Effect of Wall Shear Stress on Corrosion Inhibitor Film Performance

A dissertation presented to

the faculty of

the Russ College of Engineering and Technology of Ohio University

In partial fulfillment

of the requirements for the degree

Doctor of Philosophy

Christian M. Canto Maya

December 2015

This dissertation titled

Effect of Wall Shear Stress on Corrosion Inhibitors Film Performance

by

CHRISTIAN M. CANTO MAYA

has been approved for

the Department of Chemical and Biomolecular Engineering

and the Russ College of Engineering and Technology by

Srdjan Nešić

Russ Professor of Chemical and Biomolecular Engineering

Dennis Irwin

Dean, Russ College of Engineering and Technology

Abstract

CANTO MAYA, CHRISTIAN M., Ph.D., December 2015, Chemical Engineering

Effect of Wall Shear Stress on Corrosion Inhibitors Film Performance

Director of Dissertation: Srdjan Nešić

In oil and gas production, internal corrosion of pipelines causes the highest incidence of recurring failures. Ensuring the integrity of ageing pipeline infrastructure is an increasingly important requirement. One of the most widely applied methods to reduce internal corrosion rates is the continuous injection of chemicals in very small quantities, called corrosion inhibitors. These chemical substances form thin films at the pipeline internal surface that reduce the magnitude of the cathodic and/or anodic reactions. However, the efficacy of such corrosion inhibitor films can be reduced by different factors such as multiphase flow, due to enhanced shear stress and mass transfer effects, loss of inhibitor due to adsorption on other interfaces such as solid particles, bubbles and droplets entrained by the bulk phase, and due to chemical interaction with other incompatible substances present in the stream.

The first part of the present project investigated the electrochemical behavior of two organic corrosion inhibitors (a TOFA/DETA imidazolinium, and an alkylbenzyl dimethyl ammonium chloride), with and without an inorganic salt (sodium thiosulfate), and the resulting enhancement.

The second part of the work explored the performance of corrosion inhibitor under multiphase (gas/liquid, solid/liquid) flow. The effect of gas/liquid multiphase flow was investigated using small and large scale apparatus. The small scale tests were

conducted using a glass cell and a submersed jet impingement attachment with three different hydrodynamic patterns (water jet, CO_2 bubbles impact, and water vapor cavitation). The large scale experiments were conducted applying different flow loops (hilly terrain and standing slug systems). Measurements of weight loss, linear polarization resistance (LPR), and adsorption mass (using an electrochemical quartz crystal microbalance, EQCM) were used to quantify the effect of wall shear stress on the performance and integrity of corrosion inhibitor films. Different scenarios were evaluated in this section of the work, such as the loss of corrosion inhibitor due to the formation of foam, and the effect of different substrates on the adsorption of corrosion inhibitor.

Erosion/corrosion effects due to solids carried by a multiphase flow were investigated both on a small and large scale. Small scale experiments were performed in order to determine whether the corrosion inhibitor concentration was diminished because of adsorption onto the large surface area of entrained solid particles. The large scale experiments were done to evaluate the effect of mechanical erosion corrosion on inhibitor film performance, and *vice versa*.

The analysis of the results obtained by electrochemical characterization shows that the adsorption mechanism having a corrosion inhibitor competing with water molecules for a place on the steel surface is an accurate approach to describe this phenomenon. From the experimental results obtained in the multiphase part of this research project, it can be concluded that the performance of corrosion inhibitor films is not significantly impacted by mechanical forces alone; even under the worst case scenarios tested here (standing slug and erosion/corrosion). Reduction of inhibitor

performance was found to be primarily due to the loss of inhibitor due to consumption by adsorption particularly when a gas phase was present, leading to foam formation.

Dedication

To my wife Vanessa Fajardo Nino de Rivera who has made my life full of happiness.

To my daughter Romina Canto-Fajardo who give a new light to my heart.

I love you both.

Acknowledgments

I would like to express my sincere gratitude to my mentor, Professor Dr. Srdjan Nesic, for the guidance and support he gave me during the entire course of this work. His very presence is an example of the constant struggle to improve, that changes my life.

I would also like to thank Dr. Bruce Brown, the project leader, Dr. David Young and Dr. Brian Kinsella, for influential assistance to the work. The laboratory technicians and engineers, Al Schubert, Danny Cain, John Goettge, Cody Shafer, Phil Bullington and Steve Upton also contributed to the success of the project. The administrative staff of the Institute for Corrosion and Multiphase Technology, Edie Chalfant, Debbie Bullington and Rebecca Gill, and all my friends who worked in the Institute, everyone made the institute a nice place to work. I also want to thank my friend Yao Xiong for his collaboration to the development of the ideas in this work. I would like to thank the other members of the committee Dr. Kevin Crist, Dr. Dusan Sormaz, Dr. David Ingram, Dr. Katherine Cimatu, and Dr. David Young for their time and commitment.

To my family, Javier, Esther, Carlos and Claudia for their support during this long process.

Table of Contents

Page

List of Tables

Page

List of Figures

Page

Chapter 1. Introduction

Pipeline failures due to corrosion represent a major concern for the oil and gas industry and society. Economics is not the only aspect impacted by corrosion; environment and social safety are strongly influenced by corrosion related failures. For example, in 2006 Prudhoe Bay, Alaska witnessed the worst pipeline failure due to internal corrosion that lead to an oil spill and a shutdown of production for months. The failure resulted in enormous financial consequences (in the billions of dollars) as well as reputational damage for the companies involved. Years later, in San Bruno, California, another pipeline failure attributed to internal corrosion in a "dry" gas line killed eight people. Since the incident in San Bruno, regulations for the transportation of energy have been amended to enhance safe operation. Production loss, downtime and reduced efficiencies represent a significant problem for the oil and gas industry and thus have a direct impact on operations and production.

Many of the internal corrosion failures in pipelines are a result of the lack of understanding of the corrosion process and could potentially have been avoided if corrosion had been predicted and mitigated on time. The lack of understanding also leads to misinterpretation and use of incorrect corrosion control techniques.

Emerging problems for the oil and gas industry nowadays are the high concentrations of H_2S in gas extraction, production of sand and water in oil/gas wells, heavy oil production, oil sands production and exploration, etc. The potential impact of any occurrence, or recurrence, of the risks described above could have an adverse effect on the oil and gas industry both financially and otherwise. A detailed understanding of

corrosion control and mitigation is required for better decision making based on the complex scenarios found in the oil and gas industry around the world.

The aim of this work is to improve the understanding of corrosion control by using corrosion inhibitors when applied in pipelines under multiphase flow streams. This work will contribute to our overall ability to identify and qualify the most adequate corrosion inhibitor candidate for implementation in pipelines with high turbulence and multiphase flows. Ultimately, this work will improve our ability to understand how to:

- mitigate severe corrosivity in pipes carrying multiphase flow
- minimize safety risks
- prevent equipment failure and unplanned downtime
- reduce the cost related to corrosion
- improve education and training for corrosion control
- increase consciousness of corrosion costs and potential savings

Chapter 2. Background

2.1 Mechanisms of CO_2 Corrosion

In oil and gas production, carbon steel is the most widely used material for pipelines due to its economy and mechanical properties. However, carbon steel can rapidly corrode when exposed to CO_2 containig aqueous environments. In general, CO_2 corrosion of carbon steel is an electrochemical process. The overall reaction for steel corroding in an aqueous CO_2 environment is:

$$Fe_{(s)} + CO_{2(aq)} + H_2O_{(l)} \rightleftarrows FeCO_{3(s)} + H_{2(g)} \qquad \textit{Reaction 1}$$

This overall process is more complex than the overall reaction indicates, as described in the text below. When CO_2 is dissolved in water it reacts to form carbonic acid which then dissociates in two steps, as represented by reaction 2 through reaction 5[1,2]:

$$CO_2 \rightleftarrows CO_{2(aq)} \qquad \textit{Reaction 2}$$

$$CO_{2(aq)} + H_2O_{(l)} \rightleftarrows H_2CO_{3(aq)} \qquad \textit{Reaction 3}$$

$$H_2CO_{3(aq)} \rightleftarrows H^+_{(aq)} + HCO^-_{3(aq)} \qquad \textit{Reaction 4}$$

$$HCO^-_{3(aq)} \rightleftarrows H^+_{(aq)} + CO_3^{2-}{}_{(aq)} \qquad \textit{Reaction 5}$$

Aqueous CO_2 corrosion is a particular type of acid corrosion, due to the *in situ* formation of carbonic acid. Previously reported experimental work has shown that in a solution with a fixed pH, weak acids, such as carbonic acid, are more corrosive than strong acids, which are fully dissociated in an aqueous solution[1,2]. As carbonic acid is consumed, it is replenished according to reaction (3). Consequently, dissolved CO_2 can

act as a reservoir of additional corrosive species. This characteristic of CO_2 corrosion makes it particularly harmful for internal pipeline corrosion.

In the lower pH range (pH<7) the electrochemical reactions underlying the CO_2 corrosion process involve the cathodic reduction of hydrogen ions, and carbonic acid as shown in reaction 6 through reaction 8

Hydrogen ion reduction:

$$2H^{+}_{(aq)} + 2e^{-} \rightleftarrows H_{2(ads)} \qquad \textit{Reaction 6}$$

Carbonic acid reduction:

$$2H_2CO_{3(ads)} + 2e^{-} \rightleftarrows H_{2(ads)} + 2HCO^{-}_{3(aq)} \qquad \textit{Reaction 7}$$

Reaction 7, however, is limited by the slow hydration of CO_2 to form the carbonic acid, and in some cases by the slow diffusion of H_2CO_3 in the water phase. As pH increases above pH 7.0, bicarbonate ion, HCO_3^-, has been proposed to undergo reduction, leading to the formation of carbonate and hydrogen evolution:

$$2HCO_3^{-} + 2e^{-} \rightleftarrows H_{2(ads)} + CO_3^{2-} \qquad \textit{Reaction 8}$$

It is commonly accepted that reaction 8 is slow compared with the other cathodic reactions and can be neglected in the typical pH range seen in pipelines 3<pH<7[5].

The main anodic reaction is the dissolution of iron, given by reaction 9:

$$Fe_{(s)} \rightleftarrows Fe^{2+}_{(aq)} + 2e^{-} \qquad \textit{Reaction 9}$$

According to the Bockris[3] mechanism, this reaction is pH dependent in strong acids and this also applies to CO_2 aqueous solutions.

The formation/dissolution of a solid corrosion product layer made from iron carbonate can be described by reaction 10.

$Fe^{2+}_{(aq)} + CO_3^{2-}_{(aq)} \rightleftarrows FeCO_{3(s)}$ *Reaction 10*

According to reaction 10 if the solubility limit, K_{sp}, is exceeded, the precipitation of a $FeCO_3$ corrosion product layer will occur (reaction goes from left to right). An $FeCO_3$ corrosion product layer can be protective and reduce the corrosion rate. The precipitation rate is strongly dependent on pH and temperature[4,5]. If the corrosion product is formed on the steel surface, the overall corrosion rate can be affected by the blockage of active corrosion sites as well as the layer acting as a diffusion barrier for corrosive species. However, the $FeCO_3$ can be removed from the steel surface by mechanical forces and/or chemical interactions. The freshly exposed steel can corrode rapidly and lead to localized attack. The presence of the thick corrosion product layer can impact other forms of protection such as that provided by corrosion inhibitors due to adsorption of inhibitor on the surface of these solids (corrosion inhibitors are discussed in more detail below). The inhibition strategies should consider the possible loss of corrosion inhibitors by adsorption on the surface of corrosion product layers[6,7].

2.2 Parameters that Affect CO_2 Corrosion

The CO_2 aqueous concentration plays an important role in corrosion. An increase in the partial pressure of CO_2 leads to a higher CO_2 aqueous concentration that promotes the formation of carbonic acid which partially ionizes to form hydrogen ions; see reaction 2 through reaction 8.

Temperature can affect the corrosivity of CO_2 environments both directly and indirectly, e.g. by affecting CO_2 solubility and subsequent dissociation (direct effect) and by changing corrosion product stability (indirect effect). This latter effect can be of great

significance as increase in temperature dramatically impacts the solubility and kinetics of formation of an iron carbonate ($FeCO_3$) corrosion product, favoring its deposition at the steel surface and reducing the corrosion rate. There is experimental evidence, reported by Fajardo, *et al.*[2], (2007) showing that corrosion rate increases with temperature for up to about 80 °C. The work published by Nesic, *et al.*[8], (1996) explains that the increase in corrosion rate with temperature can occur due to increases in kinetics of the electrochemical reactions, as well as the diffusion coefficient of the corrosive species. de Waard and Lotz[9] (1993) reported that the corrosion rate reaches the maximum level when the temperature of the system is between the 70 – 80 °C after which a dense corrosion product of iron carbonate $FeCO_3$ can precipitate and thus reduce corrosion. This threshold is valid only for lower partial pressures of CO_2 and relatively high pH.

Solution pH can also significantly impact the corrosion process. In near-neutral pH systems, the corrosion product solubility decreases, facilitating formation of protective $FeCO_3$ which provides protection against corrosion[1,4,10,11]. Besides, high pH results in the reduction in concentration of corrosive species in the electrolyte (hydrogen ions) and an associated reduction in the corrosion rate. Conversely, lowering the pH increases the concentration of corrosive species in the system which increases the corrosion rate, as well as reduces the kinetics of precipitation of the protective corrosion product layer[9,12].

The pH does not only affect the availability of hydrogen ions in solution. Changes in pH may impact some of the reactions associated with aqueous CO_2 and the generation of species derived from its initial hydration. Figure 1 represents the effect of pH on the

concentration of carbonic acid (H_2CO_3), bicarbonate (HCO_3^-) and carbonate (CO_3^{2-}) species in an electrolyte, for both open and closed systems. The concentration of corrosive species was determined from dissociation constants referred to the literature[11].

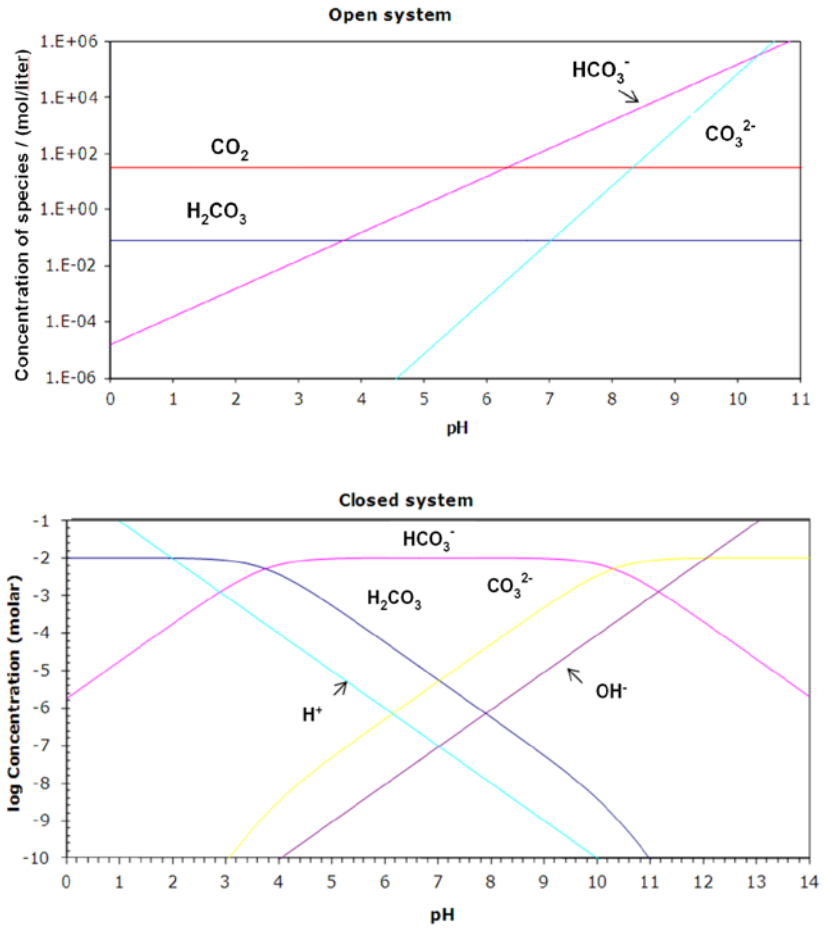

Figure 1. Concentration of corrosive species as a function of pH. Calculations were made for a concentration of 0.01 M of carbonic acid (at low pH), pCO_2 = 0.98 bars, and 25°C for a) an open system and b) a closed system.

Another important factor in CO_2 corrosion is flow. Turbulent flow introduces mixing which can help bring more corrosive species to the steel surface and enhance

corrosion – a mass transfer effect. However, there are numerous other effects of flow particularly in multiphase systems, with corrosion inhibitor present and those will be discussed below.

2.3 Mitigation of Internal Corrosion

In industrial applications, there are several ways to mitigate internal corrosion. During the design of pipeline systems, it is standard practice to select greater wall thickness (so called corrosion allowance) to help combat the adverse effects of corrosion on thinning of the wall over time. Another important way to manage internal corrosion is the utilization of corrosion resistant alloys (CRA) which are not significantly affected by internal corrosion processes, although this is a prohibitively expensive approach, applicable only for shorter pipe sections. Sometimes, and depending on the stream characteristics and flow conditions, the pipeline is internally coated in order to reduce the effect of corrosion. However, if the coating fails a rapid corrosion attack could be initiated in this small area and proceed undetected leading to localized corrosion and rapid failure.

A most economical way to mitigate internal corrosion is by the use of chemicals added into the solution that is in contact with the metal.

According to the National Association of Corrosion Engineers (NACE) any substance that when added in a small quantity reduces the oxidation rate of the metal is termed a corrosion inhibitor[13]. The most cost effective approach is to apply a corrosion inhibitor and then monitor internal pipeline corrosion over time to ensure proper mitigation[12,13–15]. The classification of these substances varies with their different forms,

such as according to their ability to reduce the magnitude of electrochemical reactions occurring at a surface. For example, a cathodic inhibitor is an inhibitor capable of reducing the rate of cathodic reactions. The substance that inhibits the anodic reaction is known as an anodic inhibitor. Chemicals that reduce both reactions are termed mixed inhibitors. Corrosion inhibitors can also be classified based upon their chemical characteristics, such as whether they are organic or inorganic. Another classification is based on the concept of principles relating to the behavior of Lewis acids and bases[15,16]. Corrosion inhibitors can also be classified according to the mechanism they mitigate corrosion, falling into one of three major categories: a) substances that adsorb on the surface and interfere with electrochemical reactions, b) substances that promote the formation of thick corrosion product layers, and c) substances that neutralize the corrosive substances in the bulk. The chemical substances capable of absorbing at the pipeline surface are often called adsorptive corrosion inhibitors, and they will be the main focus of the present work.

2.4 Corrosion Inhibitors

In the oil and gas industry, organic compounds are widely used as corrosion inhibitors. Their capacity to reduce the magnitude of electrochemical reactions is linked to their behavior as surface active compounds akin to surfactants. Those compounds are in general classified as ionic or non-ionic surfactants. Ionic surfactants are generally more active than the non-ionic surfactants; a key reason why ionic surfactants are more used as corrosion inhibitors. Ionic surfactants are also sub-divided into cationic, which are normally quaternary alkyl ammonium salts (R_4N^+), and anionic, which have the

functional groups COO^-, SO_3^-, etc. Sastri[16] has stated that non-ionic surfactants are less active because they do not have ionizable groups in their molecular structure; this is dependent on the environment to which they are exposed and the nature of their functionality. According to Xiaong-Ci *et al.*[17], (2000) when amine-type non-ionic surfactants are protonated, which could be easy for amine functionalities in acidic medium, they can be adsorbed on the metallic surface with a stronger interaction than if non-protonated.

Corrosion inhibitor molecules, as many surfactant compounds, tend to form aggregates when they reach certain concentrations in solution[18,19]. The point at which molecules begin to aggregate is called the micellar point or critical micelle concentration (CMC). Figure 2 schematically represents the formation of micellar structures in the bulk (A) and on a surface (B)[18].

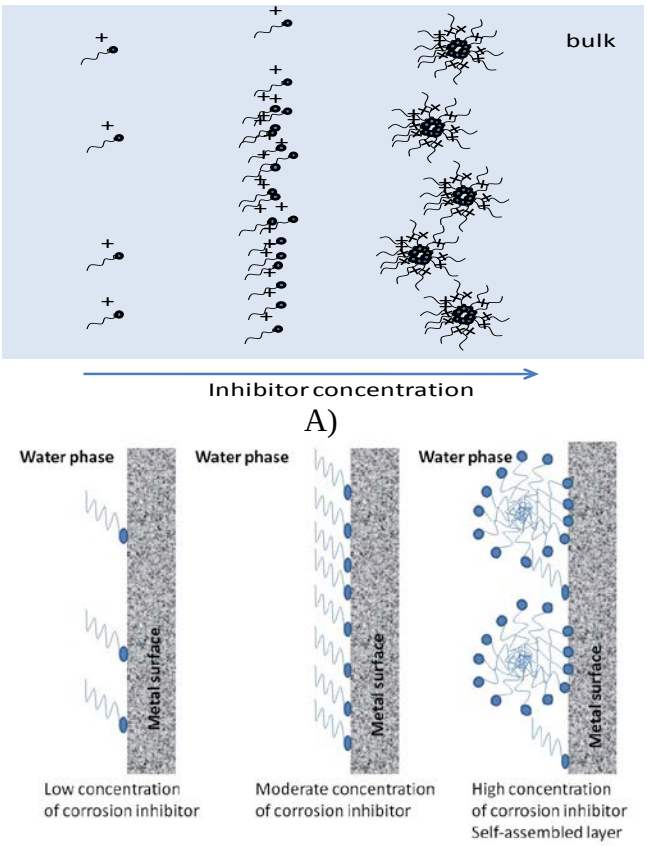

Figure 2. Schematic representation of the corrosion inhibitor adsorption and micelle formation.

Different aggregates are possible, depending on the inhibitor molecule characteristics, its amount in solution and the nature of the solution (e.g., ionic strength) as was stated by Moulik[20] (1996) and Goyal and Aswal[21] (2001). A common understanding of the adsorption of molecules onto the surface is based on the electrostatic attraction between the charged surface and the ionic surfactant. According to Knag *et al.*[22], (2004), once the first layer of corrosion inhibitor is formed on the steel surface, this affects the interaction with other inhibitor molecules coming from the bulk, dictating the

final geometry of the adsorbed inhibitor film (molecular packing). The molecular packing number (R) is calculated according to:

$$R = \frac{\upsilon}{la} \qquad \text{Equation (1)}$$

where υ is the molecular volume of the hydrocarbon chain; l is the effective length of the hydrocarbon surfactant molecule and a is the head group area. Figure 3 shows typical shapes reported in the open literature. According to Goyal and Aswall[21] (1996), at packing number $R \leq 1/3$, spherical micelles are expected. Increasing the molecular packing number to 1/2 will favor the formation of cylindrical micelles and reaching a value of 1 will lead to a lamellar geometry.

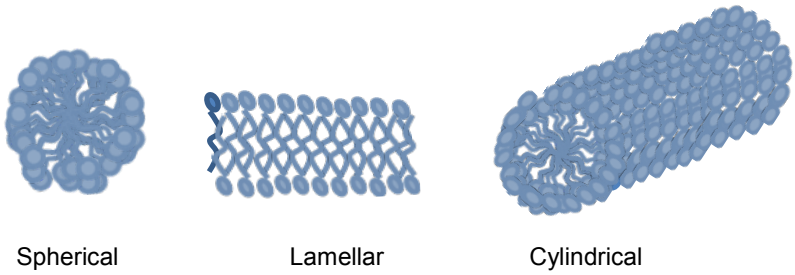

Figure 3. Schematic representation of geometrical forms of micelles.

Any reduction in the CMC by any external cause (e.g. adding salt or changing temperature) gives rise to an increase in the surfactant activity, which increases the driving force for micellization. Different parameters associated with molecular characteristics and physical and chemical parameters in the environment can influence the CMC. Description of the variables are listed below (Table 1)[18]:

Table 1. Factors that influence the critical micelle concentration

Factor	Properties	Effect on CMC
Molecular factors	Molecule architecture and head group charge	The increase in the hydrocarbon chain length favors the formation of micelles. The head group and the hydrocarbon chain, which are used to calculate the molecular packing Goyal and Aswall[21] determine the shape of the micelle.
Physical factors	Temperature	With an increase of temperature micelle interaction potential becomes more attractive favoring the micelle formation. An increase in temperature can lead to the separation of the electrolyte into two phases. One with high concentration of micelles and another with a depletion of micelles. This threshold temperature is well known for each surfactant and is called the *cloud point temperature* [21].
	Effect of salt	Salts contribute in the formation of micelles because they change the ionic repulsion between molecules, reducing in this way the micelle concentration[20].
	Effect of alcohols	It has been reported by Brown *et al.*[23], (1949) and by Benalla and Zajac[24] (2004) that the number of carbons in the alcohol are the reason for the change in the CMC. Short number of carbons will reduce the activity of the surfactants increasing the CMC. A larger amount of carbon atoms in molecules will increase the activity of the surfactant by reducing the CMC.
	Electrolyte polarity	The polarity of the media favors surfactant association. In a non-polar electrolyte the aggregation of molecules happen in a reverse orientation[18].

In the oil and gas industry there are different molecules, and mixtures thereof, that can be implemented as corrosion inhibitors. Decision relating to which inhibitor is ideal for a given situation should incorporate the analysis of the environment (water chemistry), the operating conditions (flow, velocity, temperature, pressure, etc), and the nature of the metallic surface. In general, corrosion inhibitors are complex molecules that reduce corrosion when used in small quantities (ppm range). Corrosion inhibitors are usually blended with other components to achieve enhanced performance.

Surfactant-type molecules, such as quaternary ammonium and imidazoline-type compounds, are widely used as corrosion inhibitors. These molecules have two functionalities, a polar head group which is hydrophilic and a non-polar, hydrophobic

tail[15,25–27]. According to Ramachandran *et al.*[25], (1996) the mechanism of the inhibitor attachment is through their polar head group interacting with the anodic and/or cathodic sites on the corroding steel surface; thus interfering with the electrochemical reactions. The hydrophobic tail extends away from the metal surface into the solution, where an interaction between chains should produce a protective hydrophobic film barrier that can further hinder the corrosion of steel. The polar head groups contain chemical elements such as S, N or O present in functional groups that can be chemically bound to the metal surface[17,27,30]. For a good corrosion inhibitor the molecules should easily displace adsorbed water molecules from a hydrophilic steel surface.

Attraction and interactions between corrosion inhibitor molecules and the metallic surface governs adherence strength and persistency. Molecular adsorption depends on the concentration of molecules in the bulk solution, the molecule polarity, and surface charge characteristics. The adsorption of corrosion inhibitors on a metallic surface is governed by two common types of bonding interactions.

The first is physical adsorption with relatively weak interaction between the surface and the molecules in question, such as Van der Waals bonding over a wide spectrum of dipolar interactions such as between polar species. The second type of bonding is chemical adsorption, or chemisorption, which is far stronger than physical adsorption and can happen by: ionic interaction - ions will become attracted to and interact with surfaces of opposite charge; covalent bonds - where electrons from a donor atom interact with an acceptor and become shared in a bonding interaction. A covalent

bond can only be broken by large increases in temperature or via chemical interactions, such as those occurring at a decreased pH.

The free energies associated with these two types of bonding interactions have been reported in the open literature. According to Nasser and Sathiq[28] (2010) chemisorption happens if the free energy of adsorption is lower than –40 kJ/mol. higher values, usually in the range of *ca.* –20 kJ/mol, represent a weaker interaction between the organic molecules and the surface that is characteristic of physical adsorption.

Corrosion inhibitor molecules that have nitrogen, oxygen or sulfur atoms in their structure interact with the steel surface according to one of the above bonding schemes based upon their intra-molecular dipoles and molecular charge. As a result of the adsorption process, the inhibitor molecules can then form a stable film which confers protection of the steel surface against corrosion[15,22,25]. Based on these adsorption mechanisms, it is possible to predict inhibitor efficacy according to their adsorption mechanism.

Before the implementation of corrosion inhibitors, the adsorption mechanism should be assessed based on the conditions that the corrosion inhibitor will face in operations. Factors such as temperature, pressure, flow regime, fluid composition, inhibitor concentration, etc., are usually selected carefully for testing of various inhibitors, before a final selection is made for the best performer. Different formulations have been developed by chemical companies in order to achieve the maximum performance in service. Different adsorption mechanisms have been proposed, suggesting how different surfactants, such as quaternary ammonium compounds, imidazoline

derivatives, and amines, and their combination with other compounds, such as sodium thiosulfate, act as corrosion inhibitors. These will be discussed in the following sections.

2.4.1 Imidazoline Derivatives

Imidazoline derivatives have been used as corrosion inhibitor in the oil and gas industry to minimize the corrosion induced by acid gases such as aqueous CO_2. Water soluble quarternized imidazoline compound such as, a derivatized imidazolinium ion, see Figure 4, or oleic imidazolines, act as corrosion inhibitor of steel by adsorption on its surface[29–32].

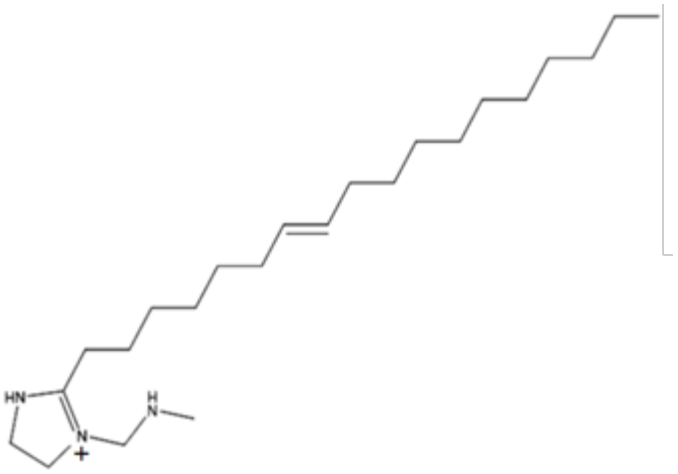

Figure 4. TOFA/DETA imidazolinium ion.

The use of this imidazolinium species as inhibitors is due to a need to have a water soluble inhibitor molecule and to have comparable results with the quaternary alkyl ammonium chloride based corrosion inhibitor, described below. In synthesis of the imidazolinium ion, a talloil diethylenetriamine imidazoline (TOFA/DETA imidazoline) is reacted with an organic acid (e.g. acetic acid) which “protonates” the imidazoline

nitrogen to form an imidazolinium cation. The synthesis studies were reported by Bajpai and Tyagi[33] (2006) ; Figure 4 represents the structure of the imidazolinium ion.

As an imidazoline derivative, this imidazolinium ion has a structure of a surfactant corrosion inhibitor. Figure 4 shows the elements that form the imidazolinium ion, which consists of a 5-membered heterocyclic head group with two nitrogen atoms, one of them with a positive charge and a pendant side chain with a long hydrocarbon tail on an adjacent carbon atom (C_{16}-C_{18} units long). As was discussed above, the head represents the hydrophilic part of the molecule and, therefore, is responsible for the molecular adsorption onto a steel surface.

Work published by Jovancicevic, *et al.*[34], (1999) summarized the effect of the imidazoline based inhibitor concentration, tail length and the head group. They reported that as the concentration increases, the inhibitor efficiency increases. There is an enhanced possibility of forming a stable film at concentrations close to or above the CMC. The importance of the head group was reported and has an effect on the solubility/stability at the interface, leading to the formation of a lamellar arrangement of molecules rather than aggregation as spherical micelles. They found that for larger hydrocarbon chain lengths more stable bilayer film could be formed, at or above the CMC.

Most organic corrosion inhibitors control corrosion by blocking of active corrosion sites. The blocking happens as a synergy between the adsorption of molecules and the steric effect of the hydrophobic chains. According to Palomar, *et al.* [31], (2011) the efficiency of imidazoline derivatives as corrosion inhibitors improves with chain length.

In their work Palomar, *et al.*[31], (2011) proposed that the adsorption of the imidazoline derivative can take place in different ways :

- Formation of an iron-nitrogen bond.
- Interaction of the *pi*-electrons between the heterocyclic part of the molecule with the steel
- Electrostatic interaction between the molecule and the steel surface

Similar adsorption mechanism using molecular modeling was published by Liu, *et al.*[32], (2009). They proposed that imidazoline derivatives inhibit corrosion by geometrical blockage of the anodic and cathodic sites. Likhanova, *et al.* [30], (2010) suggested that the geometrical blockage is influenced by the size of the corrosion inhibitor molecules allowing the formation of more stable inhibitor films. They also proposed a chemical adsorption process of imidazoline derivative due to the pi (π) electrons and a nitrogen atom with a free electron pair available to be donated at the metallic surface.

In the studies performed by Liu, *et al.* [29], (2009) the authors also evaluated the effect of 1wt.% sand entrained in water moving at high velocities and concluded that the high shear stress and erosion caused by the sand reduces the performance of the inhibitor film. However, their studies were done in a rotating cylinder electrode where the erosion effect is difficult to evaluate. Instead, the small reduction in the efficiency of inhibition for the systems with sand was probably due to the adsorption of imidazoline-type inhibitor onto sand particles. The performance of corrosion inhibitors in the presence of sand was also investigated in the present study and will be discussed later.

Zhang, *et al.*[35], (2001) studied the adsorption mechanism and the electrochemical characterization of an imidazoline derivative as a corrosion inhibitor. They calculated the thermodynamic energies of adsorption following the Langmuir isotherm, finding a $\Delta G = -30$ kJ mol^{-1}. This value of adsorption energy is in between values defined for physical adsorption and chemisorption. They found that temperature has a detrimental effect on the performance of the inhibitor.

Ramachandran and Jovancicevic [26] (1999) reported molecular modeling deployed to help understand the adsorption of imidazolines on iron oxide scale. They reported that the adsorption and the formation of a lamellar structure is primarily a function of the alkyl chain length, the same conclusion as Liu, *et al.*[32], (2010). In this work the authors calculated the binding energies for different alkyl chain lengths on the imidazoline head. They found that the bonding energy of different imidazoline molecules is strong enough to remove adsorbed water from the surface.

Zhao and Chen[36] (2012) reported that derivatized imidazolines improve the protection from CO_2 corrosion when mixed with other chemicals. In Zhao's work the adsorption energy values were reported to be in the order of -40 $kJmol^{-1}$, which is representative of a chemisorption process. In their work the authors suggested that the imidazoline ring initially adsorbs *via* electrostatic interactions with the steel surface causing an anodic shift in the zero charge potential, followed by a chemical adsorption which was represented by a negative Gibbs free energy value ($\Delta G^0 \approx$ -40kJ/mol). The mixing of imidazoline derivatives with other chemicals such as organosulfur compounds

(e.g., mercaptoethanol), aromatics, or halides strengthened the protection conferred by these molecules by building a denser and more stable inhibitor film.

2.4.2 Quaternary Ammonium Compounds as Corrosion Inhibitors

Quaternary ammonium compounds are commonly used in the oil and gas industry as corrosion inhibitors, drag reducing agents and biocides. Figure 5 shows a surfactant-type quaternary ammonium compound, “quat”, with a long alkyl group as a hydrophobic tail, a cationic nitrogen in its polar head group, and an attached aromatic ring. Thus, “quats” are cationic (R_4N^+) regardless of pH; unlike protonated amines that become deprotonated in alkaline solutions.

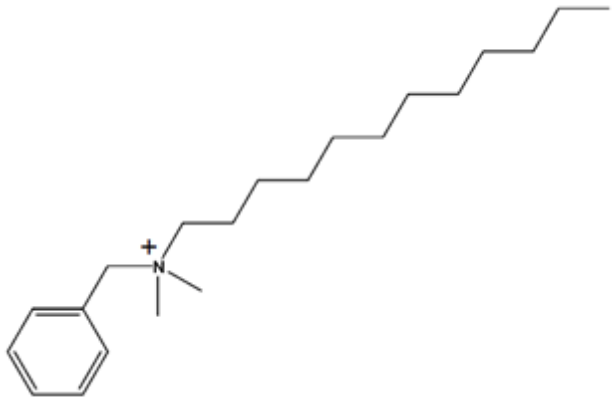

Figure 5. Schematic representation of an alkylbenzyl demethyl ammonium chloride “quat” molecule.

When quaternary ammonium salts are used as corrosion inhibitors there is a tendency of this type of surfactant to form spherical micelles as reported in the literature by Knag *et al.*[22], (2004). Electrolytes can assist the formation of micelles by lowering the repulsion between the original micelle and individual molecules resulting in ease of

incorporation into the micelle. This enlarged micelle becomes more highly charged, the electrostatic attraction with the steel surface increases with a consequent reduction of the corrosion rate by a steric blockage on the steel surface. Knag *et al.*[22], (2004) suggested that quaternary ammonium compounds adsorb rapidly at concentrations around their CMC, developing a spherical micelle structure at the steel surface.

This scenario has also been described by Bereket and Yurt[37] (2002). They stated that cationic surfactants inhibit the anodic reaction by their micellar adsorption on the surface. This micellization process follows a first stage of adsorption of individual molecules.

Fuchs-Godec[38] (2006) investigated the mechanism of corrosion in the presence of quaternary ammonium compounds, concluding that the corrosion mechanism is not altered by "quat" corrosion inhibitors. The "quats" acted by blocking the electrode reducing in this way the available open areas on the metallic surface for the corrosion process to occur. Fuchs-Godec[38] reported that concentrations above the CMC for the "quat" type inhibitors confer the best inhibition efficiency. Knag *et al.* [22], (2004) reported that quaternary ammonium chlorides are mainly adsorbed at the anodic sites leaving the cathodic areas free.

Work published by Zuauya and Dawson[39] (1993) states that "quats" inhibit the anodic reaction and also reported a shift in the potential towards the anodic direction. Zvauya and Dawson[40] (1993) and Bereket and Yurt[37] (2002) suggest that the interaction of "quats" with steel can be due to adsorption interactions with the cationic nitrogen or, given the presence of the necessary functionality, interaction of *pi* (π) electrons of a

benzene/aromatic ring with the steel surface thereby reaching adsorption energy values in the range of chemisorptions (*ca.* −40 kJ). Other studies published by Oblonsky *et al.*[41], (1995) and Dendramis *et al.*[42], (1983) that utilized Raman spectroscopy suggested that quaternary ammonium salts adsorbed *via* electrostatic adsorption on metallic surfaces. Nevertheless, they also concluded that a weak bond can be formed by aromatic ring substituents.

The work published by Knag *et al.*[22], (2004) concluded that the adsorption of quaternary ammonium compounds reached its maximum level at concentrations above the CMC in the bulk solution, and is dependent on the chain length. This is also discussed by Ramachandran, *et al.*[25], (1996) they stated that the efficiency of the inhibitor films is strongly dependent on the tail length as well as the interaction between the head groups. According to this work, in order to reach the maximum efficiency of the inhibitor film the interactions between tails and the tilt angles thereof are important to build a strong barrier to repulse water. The interaction between head groups is important to form an assembled layer in order to have efficient corrosion inhibitor surface coverage. Free[43] (2002) stated in his work that the CMC of different surfactants should be accurately calculated for each specific corrosion environment to ensure that the maximum adsorption of the surfactant is possible.

According to Malik[44–46] (1995, 2000, 2001) the corrosion efficiency of “quat” corrosion inhibitors could reach as much as 90% after 5 hours of direct contact with the steel surface. It was also reported that the inhibitor efficiency improves with concentration when the molecules are acting on clean surfaces and, again, that inhibitor

efficiency is related to the chain length. Chain lengths of C_{16} or larger reach higher efficiencies while shorter chains never reach these levels of efficiency.

The selection of a quaternary alkyl ammonium inhibitor is dependent on the corrosive environments in which they are used[39]. Malik[46] (1995) reported that the efficacy of quaternary ammonium corrosion inhibitors is strongly dependent on temperature conditions. At temperatures below 25°C the inhibitor reached efficiencies of 80% while at higher temperatures the inhibitor efficiency reached only 40%. Malik's[46] (2001) work further discussed that pH plays an important role in the adsorption of inhibitor molecules. According to Malik[45] (2000) at near neutral pH in solutions saturated with CO_2 the steel surface becomes more positively charged than in solutions with lower pH. As a result corrosion inhibitors with N^+ atoms can enhance their adsorption reducing the corrosion rate of the steel. This scenario was also suggested by Hausler[47] in 2011 in a personal communication.

2.4.3 Sodium Thiosulfate as a Corrosion Inhibitor Enhancer

The effectiveness of corrosion inhibitors has been widely reported to be strongly dependent on temperature, pH, salinity, and flow velocities (flow patterns) of the system[46,48–50]. One way to enhance inhibitor performance in a given system is by mixing different compounds that may lead to improved performance compared with the individual performance of single compounds.

One type of enhancement between chemicals can be achieved by using compounds that improves the inhibiting properties by reducing the corrosion rate. Inorganic compounds that contain sulfur are commonly used to enhance the inhibiting

properties of a corrosion inhibitor. Jovancicevic, *et al.*[51], (2000) studied the synergistic effect of sulfur compounds on corrosion inhibition in the presence of different organic inhibitors, including imidazolines and "quats". They found that the inhibitor performance improved when the concentration of the sulfur containing compounds increased.

Sodium thiosulfate, Figure 6, has been proven to have a high performance in mitigating corrosion. Phillips, *et al.*[52], (1996) studied the synergies between different corrosion inhibitor molecules applying electrochemical techniques and surface analysis. They reported that the performance of organic corrosion inhibitors was improved in mixture with thiosulfate. According to the authors, the formation of a mixed oxide and carbonate film on the surface of the metal was promoted. However, no evidence to indicate a co-adsorption of the molecules was reported.

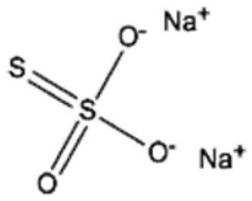

Figure 6. Diagram of sodium thiosulfate molecule.

Ezuber[40] (2009) reported the presence of sulfur in a steel corrosion product scale using EDX analysis when thiosulfate ion was present in the same solution. He concluded that this sulfur compound could be consistent with the formation of iron sulfide by the reaction of thiosulfate with the steel surface.

Kappes [53–55] has suggested that thiosulfate can disproportionate to form H_2S and SO_3^{2-} when in contact with carbon steel. With time, he observed the growth of the iron sulfide polymorph mackinawite upon exposure of steel to thiosulfate. Marcus and Protopopoff [56] (1997) also reported that dissolved thiosulfate in aqueous solution can be reduced at the steel surface to form adsorbed sulfur at specific conditions of pH and temperature. It has been extensively published that H_2S in contact with carbon steel forms iron sulfide scale with fast kinetics.

On the other hand, the risk of localized corrosion due to the oxidizing power of thiosulfate ion in systems containing high concentrations of H_2S was studied by Pou and Crolet [57] (1995) by evaluation of the effect of thiosulfate on the performance of different organic corrosion inhibitors by measuring the shift in the potential. They concluded that particular types of organic molecules, amidoamines and quaternary ammonium salts, can perform better to reduce the risk of localized attack.

2.5 Flow Enhanced Corrosion and its Effect on Corrosion Inhibitor Film Performance

Flow increases the mass transfer of corrosive species and consequently the internal corrosion of carbon steel pipelines has the potential to increase. Furthermore, if there is gas flowing concurrently with the liquid this can result in a multiphase flow (gas/liquid) in very different patterns. In horizontal pipelines, the flow patterns become more complex due to gravitational force; this causes an asymmetric distribution of phases. Depending on the flow velocity of gas and liquid, different patterns in a horizontal pipeline are shown in Figure 7. One of the most common and highly turbulent

flow pattern is slug flow [58–71]. The effect of flow on corrosion and inhibition is described in sections below.

2.5.1 Single Phase Flow

The effect of single phase flow on CO_2 corrosion and inhibition can be quantified by wall shear stress and mass transfer rate; these are parameters that describe the interaction between the steel surface and the liquid phase[48,72,73] Since higher flow rate results in higher turbulence levels and an increase in the mass transfer rates of corrosive species from bulk solution to the steel surface, therefore, the corrosion rate increases gradually when flow velocity increases[73].

The rotating cylinder electrode (RCE) has been used extensively to study corrosion as a function of the fluid flow under single phase for turbulent and laminar flow[74–76].

According to Eisenbergh, *et al*.[77], (1954) for a RCE, laminar flow is encountered at Reynolds numbers below 200. In a work published by Nesic et al.[75], (1997) using a RCE a transition between laminar to turbulent was achieved at rotating velocities above 40 rpm. The shear stress for the RCE could be calculated using equation 2 proposed by Eisenberg, *et al.*[77], (1954).

$$\tau_{RCE} = 0.0791 Re^{-0.3} \rho r_{RCE}{}^2 \omega^2 \qquad \text{Equation (2)}$$

where:

τ_{RCE} - Shear stress in the rotating cylinder electrode
Re - $\rho\omega d_{cylinder}/\mu$ → Reynolds number
ω - Peripheral velocity
$d_{cylinder}$ - Cylinder diameter
μ - Dynamic viscosity
ρ - Fluid density

r_{RCE} - Radius of the rotating cylinder electrode
ω - Angular velocity

For a single phase flow in pipelines it is expected to have laminar flow at Re<<2000 and turbulent flow at Re>>3000. An effort to correlate the shear stress found in a RCE and that seen in single phase pipe flow was reported by Silverman[74] and Nesic, *et al.*[75], (1997). The results showed that the shear stress is comparable between two geometries when the diameter is in the same order of magnitude and the flow velocity is equivalent between both geometries.

$$v_{cylinder} = 0.1066\left[\left(\frac{\mu}{\rho}\right)^{-0.229}\left(\frac{{d_{cylinder}}^{0.429}}{{d_{pipe}}^{0.2}}\right)D^{0.0371}\right]{v_{pipe}}^{1.229} \qquad \text{Equation (3)}$$

where:

$v_{cylinder}$ - rotating cylinder electrode velocity
μ - viscocity
ρ - density
$d_{cylinder}$ - cylinder diameter
d_{pipe} - pipe diameter
D - diffusion coefficient
$v_{cylinder}$ - flow pipe velocity

The shear stress encountered in a turbulent single phase pipeline could be calculated by:

$$\tau = C_f \rho u^2/2 \qquad \text{Equation (4)}$$

where:

C_f - Fanning friction factor
ρ - fluid density
u - mean flow velocity
Re - Reynolds number

The fanning friction factor, C_f, could be solved with the Patel's correlation for pipeline equation 5[78].

$C_f = 0.079Re^{-0.25}$ Equation (5)

If the wall of the internal pipe wall has formed a protective layer against corrosion (e.g. via an adsorbed organic inhibitor), the flow velocity does not play as significant a role if the system is in single phase flow. According to Gulbrandsen and Grana[60] (2007), the viscous sub-layer in a turbulent flow with a flow velocity of 20m/s is of the order of micrometers while the inhibitor film thickness is of the order of nanometers. This difference in the order of magnitude between the viscous sub layer and the inhibitor film is the reason why in single phase flow the mechanical forces do not disturb the inhibitor film[79]. However, the forces experienced in a multiphase flow could be strong enough to deteriorate a film formed for a corrosion inhibitor leading to an aggressive corrosion attack. This scenario is investigated in this work and presented in the following sections.

There are reports which state that flow velocity is responsible for corrosion inhibitor failure[48,63,80–83] while other research did not find any effect of flow on inhibitor film integrity[60,67,69,75,84]. Instead, those authors reported that loss of inhibitor protectiveness could be due to chemical contaminants, unfavorable partitioning between phases (oil and water), consumption of inhibitors by adsorption onto solids present in the brine, etc.

2.5.2 Multiphase Flow

A study of flow effects on inhibitor film performance are not performed solely in single phase systems; instead multiphase flow systems are incorporated to evaluate inhibitor performance. Transportation of oil gas is often under multiphase flow conditions when in addition to oil and/or gas the flow includes water and even solid particles such as sand, so complex multiphase flow patterns are found.

Solid/liquid multiphase flow:

The production of oil is usually accompanied by a certain amount of sand. In those fields which produce measurable quantities of sand, a fairly typical concentration is reported to be about 20-290 ppm[85]. Such a solid/liquid multiphase flow causes damage either by mechanical forces (due to erosion by sand), electrochemical mechanisms (corrosion) or by combined effects; this is termed erosion/corrosion[86,87,88]. When the flow carries solids, a synergy can accelerate the erosion-corrosion degradation process beyond being just the additive effect of erosion and corrosion, i.e. erosion-corrosion > erosion + corrosion.

Erosion-corrosion was studied by many, in oil and gas systems studies by Shadley*, et al.*[86], (1996) and McLurry*, et al.*[90], (2000), etc.; they recognized sand as a harmful component in oil and gas production, suggesting an erosion rate that is dependent on the flow velocity and angle of impact[89], even when the produced amount of solids is small.

The presence of sand results in problems that also affect corrosion inhibitor performance. Loss of inhibitor efficiency can result from adsorption of inhibitor onto the large surface area of sand particles or by mechanical erosion of the inhibitor film due to impingement of sand particles. Work published by McMahon*, et al.* [86], (2005) states that quantities of solids expected in high solid content wells are of the order of 3000 ppm, yet this does not always result in loss of inhibitor due to parallel consumption onto solid [85].

Gas/liquid multiphase flow:

Depending on the flow rate of gas and liquid flowing together, multiphase flow can develop different flow regimes[91–95]. In horizontal pipelines the flow patterns become more complex due to the force of gravity, which causes an asymmetric distribution of phases. One of the most common and most turbulent flow regime is slug flow[63,67,93,96,97]. Many efforts have been made to measure shear stress in horizontal pipe slug flow[67,97,98]. Schmitt *, et al.* [99]*,* (2000) reported that the critical wall shear stress in a horizontal pipe could reach a value of 260 Pa. Nesic*, et al.* [67]*,* (1995) reported a wall shear stress of the magnitude of 100 Pa and argued that this could be higher in the section of maximum turbulence in the slug front. It has been claimed that this high shear stress could be mitigated with the addition of inhibitors into the system due to their drag reduction properties[69].

The typical flow regimes in a horizontal line are given in Figure 7[96] . In a two-phase flow (gas/liquid) the total velocity of the multiphase flow is determined by the sum of the superficial gas velocity (v_{sg}) and the superficial liquid velocity (v_{sl}), which are obtained by dividing the volumetric flow rate of a given phase by the full cross sectional area of the pipe. When the v_{sg} and v_{sl} are low, stratified smooth and wavy flow develops in the pipe. If v_{sg} increases then a bubble flow occurs, when the gas disperses into the liquid phase as it flows along the pipeline. If the v_{sg} increases as well, slug flow is formed. Slug fronts overrun and displace the liquid layer and a highly turbulent flow is created. Annular/annular mist flow is created when the the v_{sg} highly increases entering the gas at the center of the pipeline, leaving the liquid in the pipe wall forming an annular

liquid film. A transition between slug flow and annular flow is so called wavy annular flow.

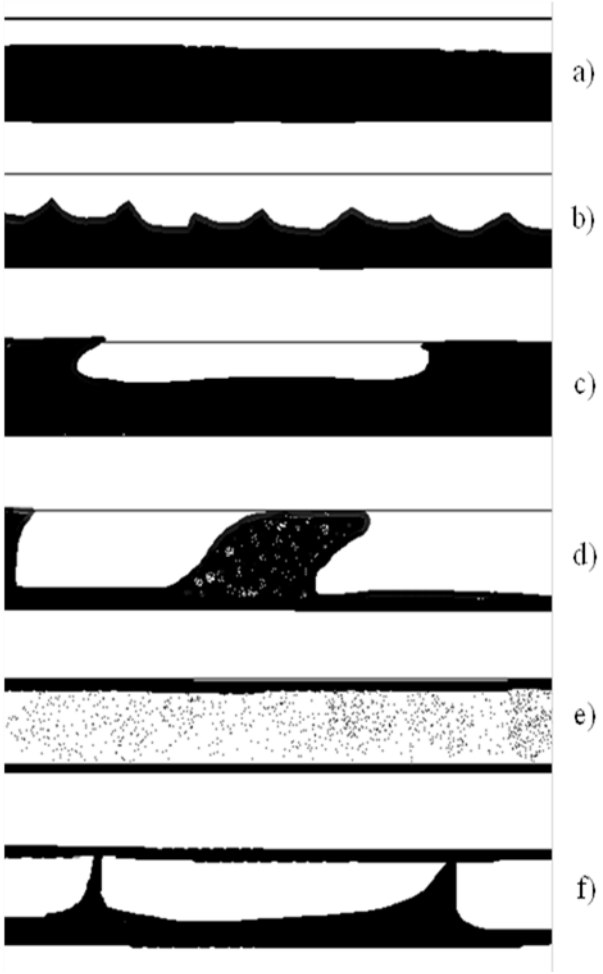

Figure 7. Flow patterns developed in a horizontal flow loop a) Stratified smooth flow. b) Stratified wavy flow. c) Elongated bubble flow. d) Slug flow. e) annular/annular mist flow. f) Wavy annular flow. [96]

2.6 Mass Transfer and Wall Shear Stress in Different Experimental Systems

It has already been argued that an increase in flow velocity increases turbulence and eventually the transport (mass transfer) of corrosive species from the bulk to the pipe wall which may result in an increase in internal corrosion rate.

Mass transfer is linked with the shear stress[73,100]. The relation between the two parameters can be explained by using the turbulent boundary layer theory. Increased turbulence and mixing in the bulk will bring the faster moving fluid closer to the wall (making the hydrodynamic boundary layer thinner), resulting in a higher velocity gradient and higher wall shear stress. Likewise, higher turbulent will bring reactive species closer to the wall where they are consumed, making the mass transfer boundary layer thinner, the concentration gradient higher and the resulting mass transfer rate also higher.[69,72,101].

Different methodologies and tests have been made in order to quantify mass transfer and wall shear in flow systems[102]. Different apparatuses, such as jet impingement, rotating cage, flow loops, and cavitation based techniques have been used to measure these hydrodynamic parameters[102].

Shear stress in jet impingement:

One of the most widespread methods to create a high wall shear stress is achieved by using the jet impingement apparatus[60,72,100,101,103,104,105]. The jet impingement flow geometry consists of a jet of liquid flowing directly and perpendicularly onto a static surface (Figure 8).

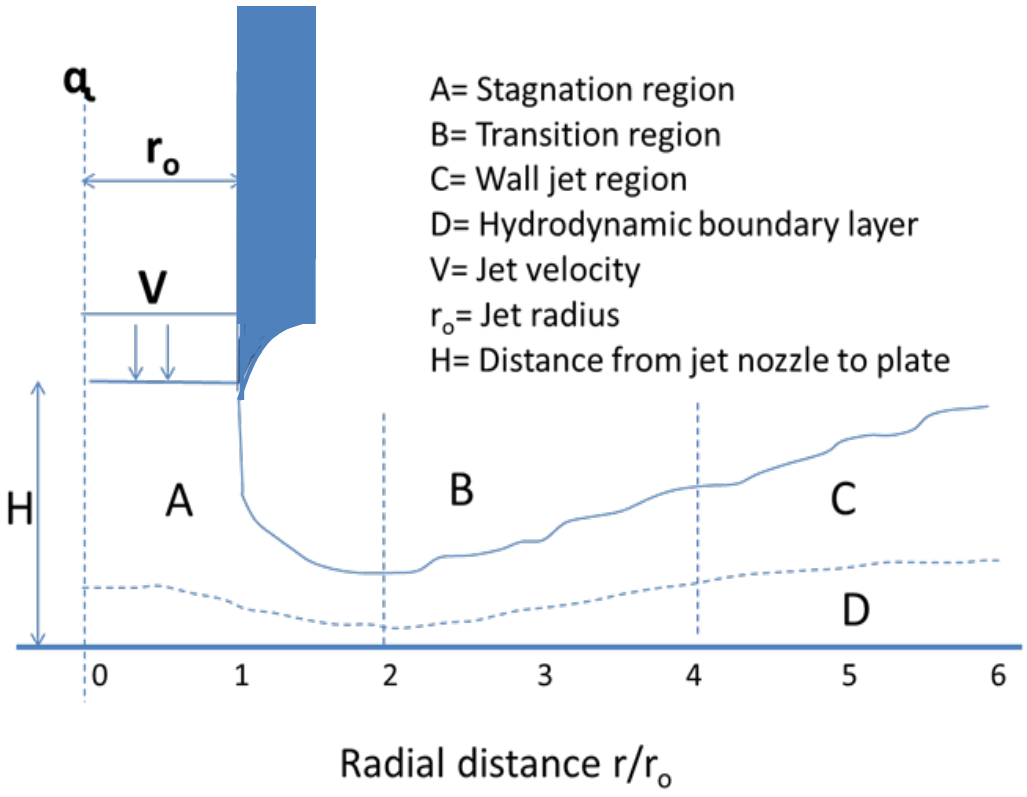

Figure 8. Jet impingement geometry[72].

The wall shear stress exerted on the surface is different in the three regions (Figure 8). The wall shear stress intensities are higher in the region ***A*** of the surface and decreases radially from the impingement point, region *B* and ***C***. For region A of the surface ($r/r_o < 2$) the flow is laminar and the wall shear stress can be calculated according to Phares, *et al.*[105], (2000):

$$\frac{\tau Re^{1/2}\left(\frac{H}{d}\right)^2}{\rho v^2} = G\left(\frac{r}{H}\right) \qquad \text{Equation (6)}$$

$$Re = \frac{2r_0 v\rho}{\mu} \qquad \text{Equation (7)}$$

$$G\left(\frac{r}{H}\right) = 0.0447Re^{0.318}\frac{r}{H}^{-2} \qquad \text{Equation (8)}$$

At the radial distance of $r/r_o \approx 2$, a transition from a laminar to turbulent flow regime occurs. A correlation to approximate the wall shear stress at the transition zone/pattern was also proposed by Phares, *et al.*[105], (2000).

$$\frac{\tau Re^{1/2}\left(\frac{H}{2r_0}\right)^2}{\rho v^2} = 0.0447 Re^{0.318}\left(\frac{r}{H}\right)^{-2} \qquad \text{Equation (9)}$$

where:

Re - Reynolds number defined for the jet
ρ - density
r - radial distance from the center of the coupon
r_o - is the ratio of the nozzle
H - distance between the nozzle and the wall specimen

Shear stress in multiphase flow loop:

Analyses of mass transfer and wall shear stress correlations have been proposed by different authors using non-dimensional numbers, in order to quantify the value of wall shear stress in a multiphase flow loop, under slug flow conditions[67,92,97]. The results of these works show a relatively close correspondence. The average reported wall shear stress for a system with a superficial liquid velocity of the order of 1m/s and superficial gas velocity of the order of 1 m/s is in the order of tens of Pascals. In a proprietary research performed by Nesic, *et al.*[67], (1995), a range of superficial velocities was studied by mass and heat transfer analysis; in each case the average wall shear stress was less than 100 Pa. Maley and Jepson[97] (2002), using a hot film probe in a stationary slug, reported an average wall shear stress of 160 Pa. In a different approach Li[98] (2012) used the floating element sensor to measure the wall shear stress in different channel configurations (pipeline and flow channel cell). The study reported wall shear stress for a

single phase pipeline in the range from 2 to 13 Pa depending of the flow rate. For gas/liquid multiphase flow the shear stress measured at the bottom of the pipe was in the ranges from 25 to 45 Pa for different superficial gas and liquid velocities.

Shears stress in a rotating cage:

The rotating cage is also used to evaluate corrosion inhibitor performance under high flow rates[93,102,106,107]. In the rotating cage configuration, the coupons are arranged vertically between two plates, called the cage, rotating at different speeds. Papavisanam, *et al.*[106], (1999) reported that the flow pattern in the rotating cage depends on the length and width of the vortex. To calculate shear stress in the rotating cage Papavisanam *et al.*[107], (2003) proposed an empirical correlation for the region where the length and width of the vortex increases as function of rotation speed:

$$\tau_{RC} = 0.0791\ Re_{RC}^{-0.3} \rho\ r_{RC}^{2} \omega^{2.3} \qquad \text{Equation (10)}$$

where:

Re_{RC} -Reynolds number defined for the rotating cage
ρ - density
r_{RC} - radius of the rotating cage
ω - rotation speed

The above correlation does not work for turbulent zone. The value shear stress in the turbulent zone might be higher than the predicted for equation 9.

Deslouis, *et al.* [108], (2004) used microelectrodes ensemble in the rotating cage to measure the wall shear stress. The shear stress reported was in the order of 100 Pa for the rotation cage.

Shear stress on a steam cavitation cell:

Other much more extreme conditions at which different authors have tested wall shear stress involve use of cavitation techniques[70,71,109–118]. Different cavitation methods have been developed such as ultrasonic cavitation, or steam cavitation. The cavitation process is characterized by the high energy delivery by the collapse of bubbles, which are generated by an abrupt change in pressure. This change of pressure and the collapse of the micro-bubbles are characterized by representative noise. The wall shear stress values measured applying cavitation reported in the open literature are in the range of Mega Pascals (MPa)[109,111,116,118], and are much higher than the wall shear stress reached in multiphase pipelines operated in the field. Besides this unrealistic value of wall shear stress, cavitation processes increase the temperature due to the excessive amount of energy produced in bubble collapse and abrupt changes in pressure.

2.7 Overall Objectives

As was discussed above, corrosion inhibitors are chemical substances which when added in small quantities (ppm range) are capable of adsorbing on the internal pipe surface and mitigating corrosion. However, there is concern that mechanical forces exerted by the flow, particularly in multiphase flow such as in slug flow conditions, might lead to disruption of the corrosion inhibitor film leading to localized attack[48,58,80,93,119,120]. Furthermore, it has been published that there is a critical wall shear stress, above which the inhibitor film could be removed from the steel surface[61,93,99]. However, there are other experimental and theoretical studies[60,75,79,121] that did not find any effect of wall shear stress on inhibitor film performance and concluded that the

failure of inhibitors to protect may be due to other reasons such as oxygen contamination or because the multiphase flow increased mass transfer of corrosive species.

An important open question remains. Can a high wall shear stress seen in multiphase flow in oil and gas pipelines affect the performance of a corrosion inhibitor film?

The aim of the present research project was to try and answer this question. Different hypothesis were tested:

- Corrosion inhibitors adsorb on the steel surface by physisorption mechanism to form a protective film, which is therefore vulnerable to damage by mechanical forces generated in multiphase flow.
- High flow rate in a multiphase flow generates high enough wall shear stress so that the corrosion inhibitor film can be disrupted.
- In multiphase flow, the corrosion inhibitor can be consumed by adsorption on solid-liquid interfaces (e.g. surface of sand particles) and/or gas-liquid interfaces (bubbles, droplets), thereby failing to protect the steel surface.

In order to test the previous hypotheses, the research work was organized in three main sections:

1. Thermodynamic and electrochemical corrosion inhibitor characterization:
    - Electrochemical behavior and enhancing between different corrosion inhibitors.
    - Characteristic adsorption isotherms and adsorption energy of the corrosion inhibitors tested.

2. Loss of inhibitor performance in gas-liquid multiphase flow:

    - Effect of high wall shear stress on the integrity of corrosion inhibitor film.

    - Role of substrates in the adsorption characteristics of the corrosion inhibitors.

    - Effect of foam formation on the availability of corrosion inhibitors.

3. Loss of inhibitor performance in solids-liquid multiphase flow.

    - Effect of inhibitor loss due to adsorption onto the sand surface.

    - Effect that the erosion-corrosion has on corrosion inhibitor removal in solid-liquid flow process, and *vice versa.*

Chapter 3. Corrosion Inhibitor Characterization

3.1 Introduction

Corrosion inhibitors are typically complex molecules that form a film at the metallic surface capable of retarding cathodic and/or anodic reactions. Organic corrosion inhibitors that contain a nitrogen atom in their structure are capable of forming a coordinated bond between the iron and the nitrogen[13,15,16]. This situation can happen when the nitrogen compound is adsorbed on the steel due to electrostatic interactions. However, corrosion inhibitors with a nitrogen atom do not impede the diffusion of oxygen towards the steel surface[50,122].

Inorganic corrosion inhibitors, such as sodium thiosulfate, Figure 9 c), have a different mechanism than the one described for organic corrosion inhibitors. The iron sulfide film is the result of reaction between the iron surface and thiosulfate ion. In the work published by Kappes *et al.*[53,54], (2011, 2012) suggested that the film could be very dense if the concentration of $S_2O_3^{2-}$ is greater than 10^{-3}M. Mixing such inorganic compounds, with organic corrosion inhibitors is a common procedure for chemical companies used to increase the efficacy of inhibitor performance in different environments.

The mixing and application of inorganic and organic compounds is underpinned by intensive research on synergistic effects between these components for specific environments. There is evidence in some publications [57,80] that antagonistic behavior can arise, depending on the conditions and the characteristic of the medium.

In this section of the present work, electrochemical analysis of organic corrosion inhibitors: imidazoline/imidazolinium (Figure 9a), and alkylbenzyl dimethyl ammonium chloride type (Figure 9 b), as well as the inorganic inhibitor: sodium thiosulfate (Figure 9 c) is investigated.

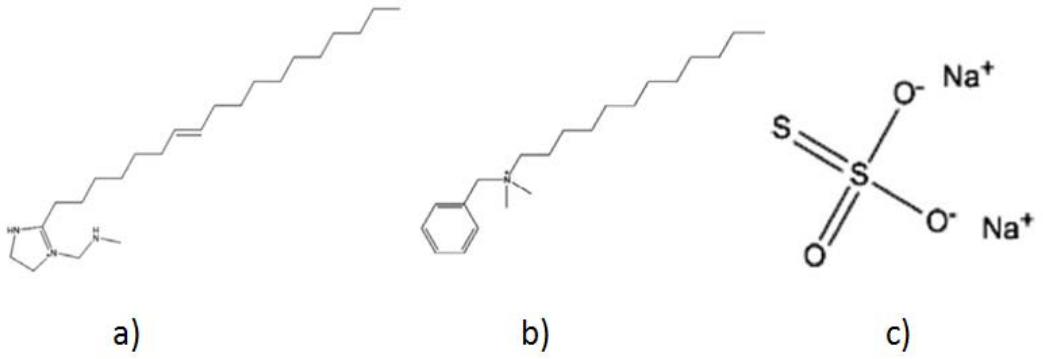

Figure 9. Corrosion inhibitors: a) TOFA/DETA imidazolinium ; b) alkylbenzyl dimethyl ammonium chloride; c) sodium thiosulfate.

3.2 Objectives

- Determine the electrochemical behavior of five different corrosion inhibitor formulations termed K1 (TOFA/DETA imidazolinium), K2 (alkylbenzyl dimethyl ammonium chloride), K3 (sodium thiosulfate), K4 (blend between K1 and K3), K5 (blend between K2 and K3).
- Determine the effect of inorganic inhibitor (sodium thiosulfate) added when blended with organic corrosion inhibitor on the corrosion inhibitor performance.
- Determine the characteristic adsorption isotherms for these corrosion inhibitors.

3.3 Equipment

Corrosion experiments were conducted in a two liter glass cell, filled with 1 wt.% NaCl solution. Beginning one hour before the experiment carbon dioxide (CO_2) was continuously bubbled into the system. The pH was adjusted with deoxygenated $NaHCO_3$ solution as needed and constantly measured. The working electrode was a 1018 carbon steel rotating cylinder (0.475" diameter, 0.5" length). The counter electrode was a concentric platinum wire and the reference electrode was a saturated Ag/AgCl electrode connected externally *via* a Luggin capillary, see Figure 10. For electrochemical characterization, corrosion inhibitors were evaluated at different concentrations, below, at and above the critical micelle concentration (0.5xCMC, 1xCMC, 2xCMC).

Corrosion inhibitor adsorption experiments were also conducted in a glass cell, using an electrochemical quartz crystal microbalance (EQCM), Figure 11. Corrosion inhibitor was added until it reached a concentration of 2xCMC.

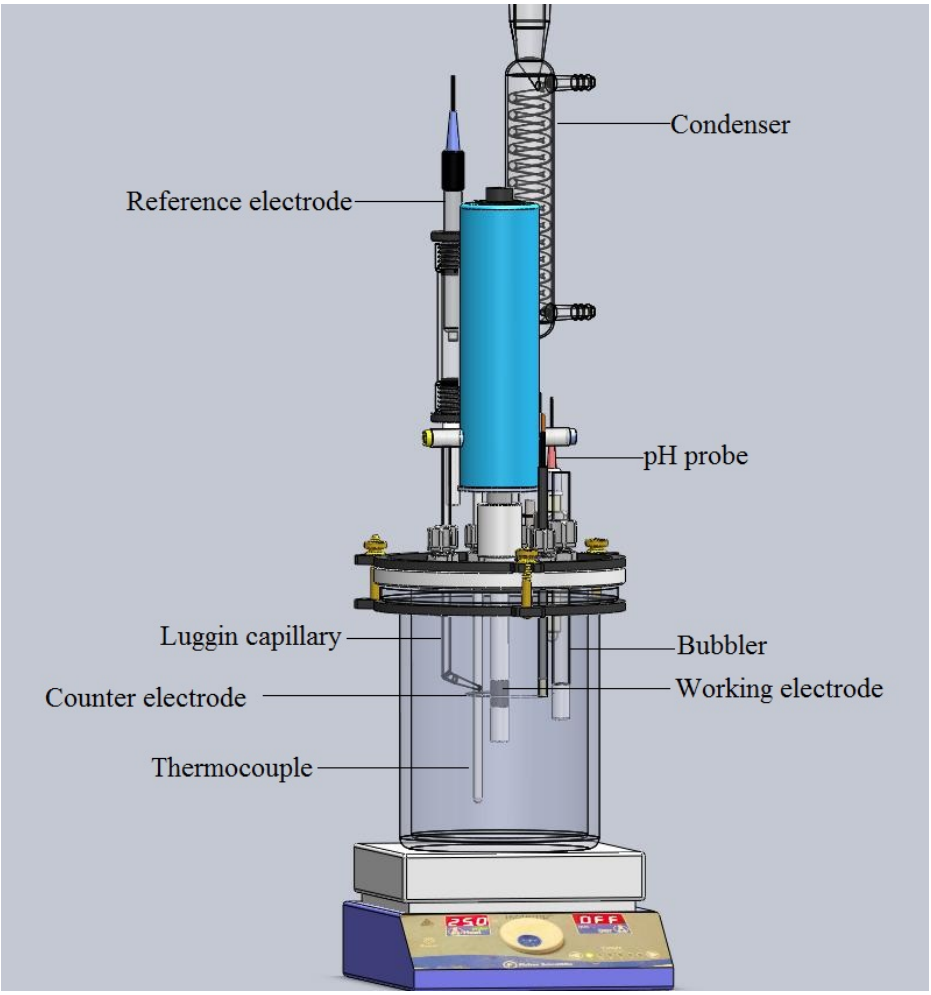

Figure 10. Electrochemical cell design.

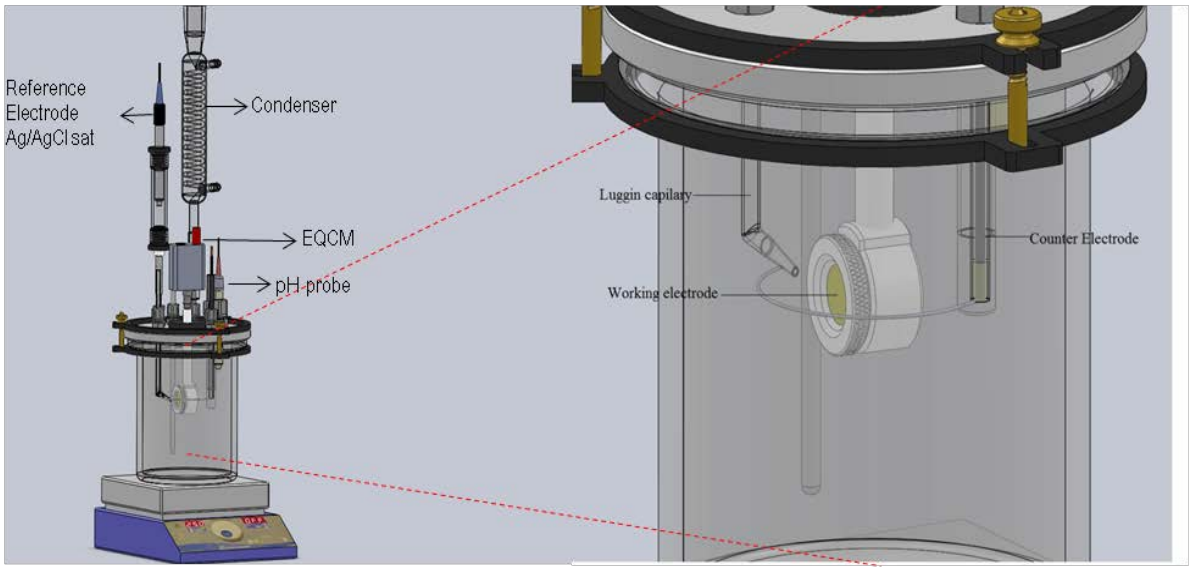

Figure 11. Electrochemical quartz crystal microbalance (EQCM) ensemble to perform electrochemical measurements in a glass cell.

3.4 Experimental Procedure

Five corrosion inhibitors labeled K1 to K5, as shown in Figure 9 and Table 2, were investigated. The present chapter is divided in two sections. The first section is related to the electrochemical characterization of these corrosion inhibitors and the second part relates to the adsorption of corrosion inhibitors on a steel surface.

3.4.1 Electrochemical Characterization

The electrochemical characterization of the five corrosion inhibitors included corrosion rate calculated from linear polarization resistance and potentiodynamic sweeps. Polarization resistance (R_p) measurements were obtained by polarizing the working electrode 10 mV from the corrosion potential (± 5 mV from the E_{oc}) at a scan rate of 0.125 mV/s. R_p values were measured during entire experiments at intervals of 30 minutes. At the end of the experiment, potentiodyamic sweeps were performed at a scan

rate of 0.250 mV/s (from -1.1 V to -.5 V vs sat Ag/AgCl electrode). At the end of the experiment the coupon was removed, rinsed with alcohol, dried and weighed.

3.4.2 Critical Micelle Concentration

Determination of corrosion inhibitor critical micelle concentrations was performed using the standard weight drop method, explained in more detail in the following section.

Table 2. Corrosion inhibitor information

Product	Description	Active Ingredient	Components
K1	Generic inhibitor	TOFA/DETA imidazolinium	10% CH_3COOH 13% $C_4H_9OCH_2CH_2OH$ 24% TOFA/DETA imidazoline Balance water
K2	Generic Inhibitor	Alkylbenzyl dimethyl ammonium chloride	24% Alkylbenzyl dimethyl ammonium chloride Balance water
K3	Generic Inhibitor	Sodium thiosulfate	36% $Na_2S_2O_3 \cdot 5H_2O$ Balance water
K4	Inhibitor blend	TOFA/DETA imidazolinium + Sodium thiosulfate	10% CH_3COOH 13% $C_4H_9OCH_2CH_2OH$ 20% TOFA/DETA imidazoline 6.28% $Na_2S_2O_3 \cdot 5H_2O$ Balance water
K5	Inhibitor blend	Alkylbenzyl dimethyl ammonium chloride + Sodium thiosulfate	20% Alkylbenzyl dimethyl ammonium chloride 6.28% $Na_2S_2O_3 \cdot 5H_2O$ Balance water

3.5 Test Matrix

Table 3 shows the experimental test matrix used to electrochemically characterize the corrosion inhibitors, and to determine the adsorption isotherm of the corrosion inhibitor at the steel surface.

Table 3. Experimental conditions - Electrochemical characterization and adsorption of corrosion inhibitor on a steel surface

Test solution	Water + 1wt% NaCl
Temperature	25 °C
Partial pressure of CO_2	0.98 bar at 25 °C
Corrosion inhibitor tested for electrochemical characterization	K1, K2, K3, K4, & K5
Corrosion inhibitor tested for adsorption isotherms	K1 and K2
Inhibitor concentration tested	For electrochemical characterization 0.5CMC, 1CMC, 2CMC
Test material (for the electrochemical characterization)	Carbon steel
Electrochemical techniques	Linear polarization resistance (polarization from -0.005V to 0.005V) Electrochemical sweeps (sweep rate 0.025mV/s) Corrosion rate was measured from linear polarization resistance

3.6 Results and Discussion

3.6.1 Critical Micelle Concentration Determination

The point at which molecules begin to aggregate is called the micellar point or critical micelle concentration (CMC). The CMC of the organic corrosion inhibitors were determined by the weight drop method[18,20,123]. The method measures the effect of the inhibitor concentration on the surface tension of water or brine. In the weight drop method, drops of DI-water or brine with corrosion inhibitors are formed by a vertical capillary of know diameter (0.156cm). Then, the drops are weight after detach from the tip of the capillary (figure 12) to calculate the surface tension of the liquid following:

$\gamma = \Phi\ mg/2\pi r$ Equation (11)

where:

γ - surface tension
Φ - correction factor
m - mass
g - gravity
r - radius of the capillary

The micellization concentration is reached at the point where the surface tension is not influenced by the inhibitor concentration. The CMC is represented graphically by the breakpoint of the curve of surface tension versus concentration[20].

Figure 12 Weight drop method for determining the surface tension.

Figure 13 and Figure 14 shows the critical micelle concentration (CMC) for inhibitor K1 (imidazolinium type) and inhibitor K2 ("quat-type") respectively. As was discussed in Chapter 1, the micellar concentration is affected by salinity of the system. The effect of the NaCl, could be seen by the reduction of the CMC for both inhibitors. For inhibitor K1 the CMC is reduced from 718 ppm to 36 ppm. For inhibitor K2 the

CMC was reduced from 470 ppm to 110 ppm. In Table 4 these values are compared with the ones reported in the literature.

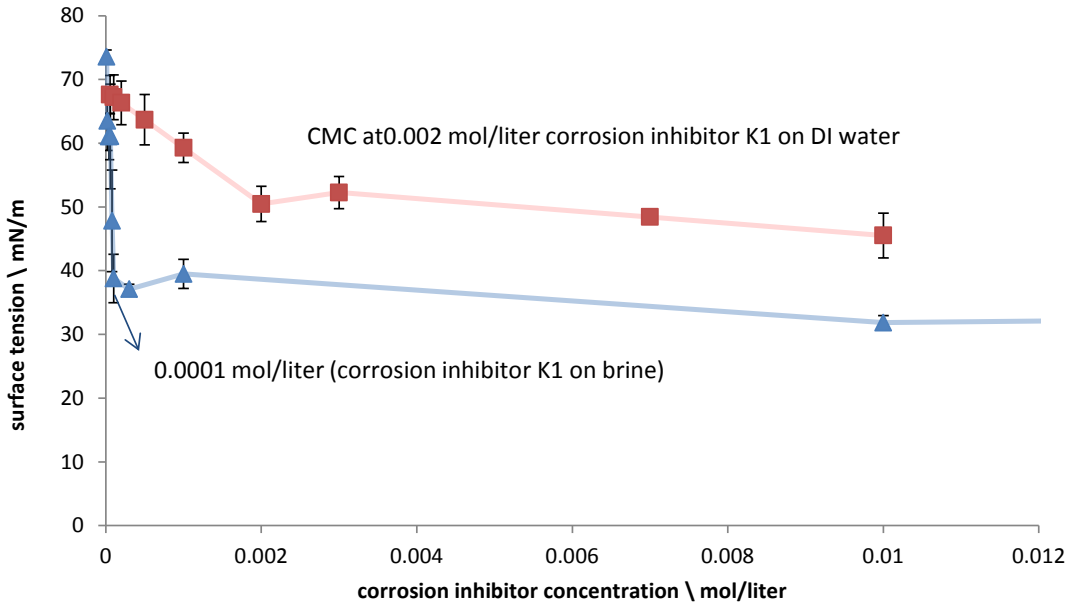

Figure 13 Determination of the critical micelle concentration (CMC) for inhibitor K1 (TOFA/DETA imidazolinium ion) with fresh DI water (square marks) and 1 wt.% NaCl (triangle mark).

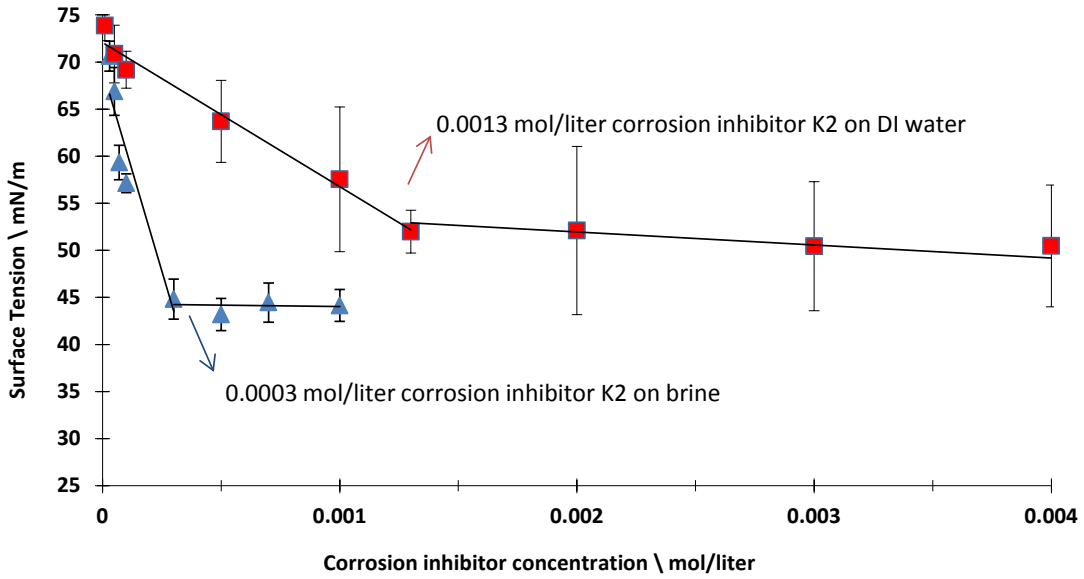

Figure 14. Determination of the critical micelle concentration (CMC) for inhibitor K2 (Alkylbenzyl dimethyl ammonium chloride) with fresh DI (square mark) water and 1 wt.% NaCl (triangle mark).

Surfactant compounds, tend to form aggregates (micells) when they reach certain concentrations in solution[18,19]. Inhibitor K3 *is not a surfactant*; therefore, it does not have a micellar concentration. Table 4 shows the effect of the salinity in the CMC for the corrosion inhibitors with organic molecules tested in this work.

Table 4. Critical micelle concentration (CMC) for five different corrosion inhibitors.

Product	**Active ingredient**	**CMC in DI-water (experimental data)**	**CMC in DI-water (reported in literature)**	**CMC 1wt% NaCl (experimental data)**	**CMC brine (reported in literature)**
K1	TOFA/DETA Imidazolinium	0.002 mol/liter (718 ppm)	-	0.0001 mol/liter (36 ppm)	Measured on CO_2 saturated water $2.57x10^{-4}$ mol/liter for chain length of C15 [124] $1.3x10^{-4}$ for chain length of C17 [124]
K2	Alkylbenzyl dimethyl ammonium chloride	0.0013mol/liter (471 ppm)	0.002 mol/liter [125] 0.0046 mol/liter [126] 0.002 mol/liter [127]	0.0003mol/liter (110 ppm)	$2.1x10^{-5}$ mol/liter in a 3 wt% NaCl solution[129] $2x10^{-5}$ mol/liter in a 4.7 wt% NaCl solution[127]
K3	Sodium thiosulfate	-	-	-	-
K4	TOFA/DETA Imidazolinium & sodium thiosulfate	753 ppm	-	215 ppm	-
K5	Alkylbenzyl dimethyl ammonium chloride & sodium thiosulfate	543 ppm	-	290 ppm	-

3.6.2 Electrochemical Characterization

Figure 15 shows the decrease in the corrosion rate due to adsorption of TOFA/DETA imidazolinium, labeled K1, on 1018 carbon steel. Subsequent additions of corrosion inhibitors were made until the CMC was reached. At this concentration, the corrosion rate of the carbon steel was reduced from 0.9 mm/year to 0.06 mm/year, representing a corrosion inhibitor efficiency of about 93%. The corrosion inhibitor efficiency was calculated using equation 12.

Inhibitor Efficiency (%) = $100 \cdot (CR_o - CR_i) / CR_0$ Equation (12)

where CR_0 is the uninhibited corrosion rate, and CR_i is the inhibited corrosion rate.

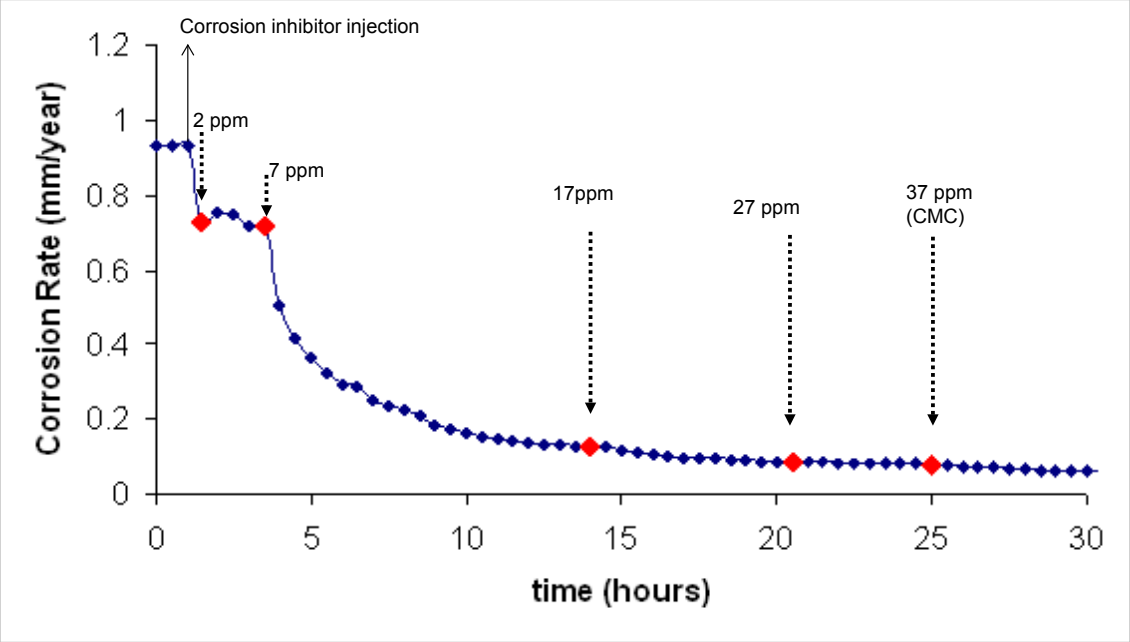

Figure 15. Corrosion rate (LPR - glass cell) of subsequent additions of inhibitor K1 (TOFA/DETA imidazolinium - CMC 36 ppm) at pH 5.0, 25°C, 1000 rpm and pCO_2=0.98 bar.

Figure 15 shows the electrochemical behavior of corrosion inhibitor K1 where potentiodynamic sweep measurements were conducted. The concentrations tested were 0.5, 1 and 2 times the CMC. Results showed the reduction of the current density each time that the inhibitor concentration increases. The anodic reaction shown in the potentiodynamic sweeps was retarded once the inhibitor was added into the system. The constant anodic slope for the system free of inhibitor is 40 mV/decade, and a negligible change in the anodic slope was detected when the corrosion inhibitor increases in concentration. This is an indication that the corrosion inhibitor adsorbs on the steel

surface providing a coverage effect without interfering in the corrosion mechanism. This confirms that the ionic imidazolinium head group works by geometrical blockage of active sites on the steel surface. No changes in the anodic slopes represent an indication of no change in the mechanism of the anodic reaction.

The cathodic reaction for an uninhibited system shows the characteristic limiting current density (i_{lim}) around 1 A/cm^2 and at very high cathodic overvoltage water reduction line is seen. When corrosion inhibitor was added to the system, even at the smaller concentration of 0.5CMC, the i_{lim} did not appear in the cathodic polarization curve. Instead, a transition toward activation control is seen for the inhibited systems. An activation control indicates that the electron transfer rate is the controlling step in the corrosion process.

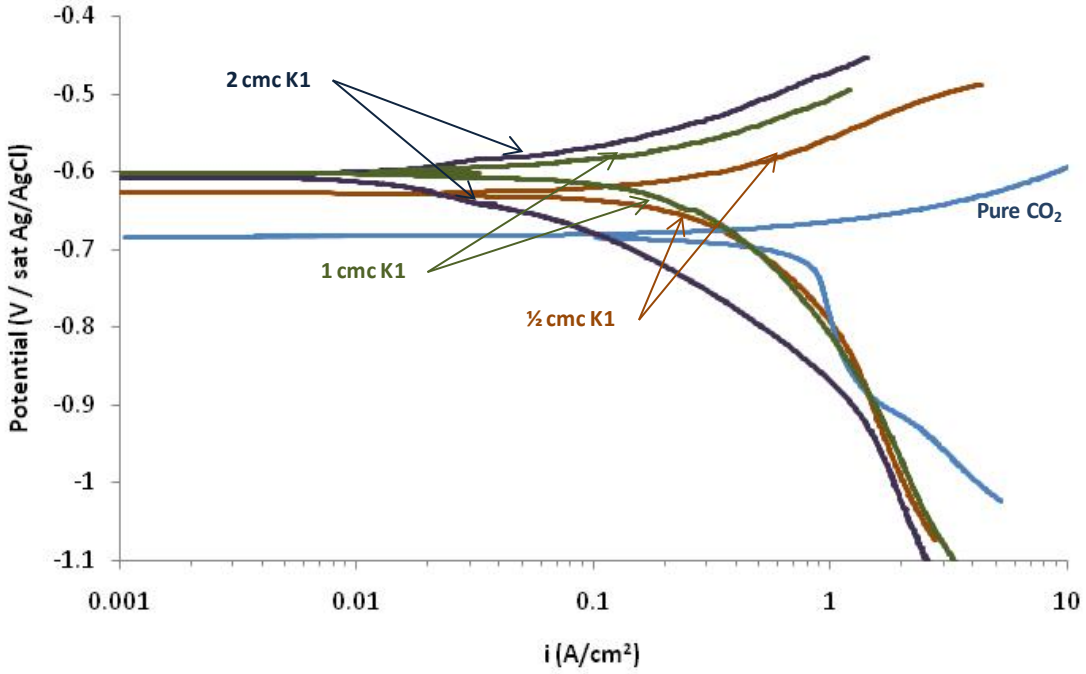

Figure 16. Electrochemical behavior of corrosion inhibitor K1 (TOFA/DETA imidazolinium) at different micelle concentrations when the concentration is 2 cmc (pH 5.0, 25°C, 1000 rpm).

Figure 17 shows the corrosion rate point trajectory for the inhibitor K1 when the concentration is 2 times the CMC. The corrosion rate obtained from LPR overlaid with the polarization curve at different test time points. From the curve it is clear that the corrosion potential is shifted to more anodic values once the inhibitor added to the solution. The change to more positive potentials happens during the first 30 minutes of the addition of the inhibitor, indicating blockage that can be detected only on anodic sites. After two hours of the exposure to the inhibited solution the potential becomes stable (at -600 mV). The stabilization in corrosion potential could be understood as more effective blockage due to possibly a superimposed assemblage of the protective inhibitor film,

forming lamellae with more hydrophobic properties, as was reported by Ramachandran and Jovancicevic (1999)[26] and Liu, *et al.* [32], (2010).

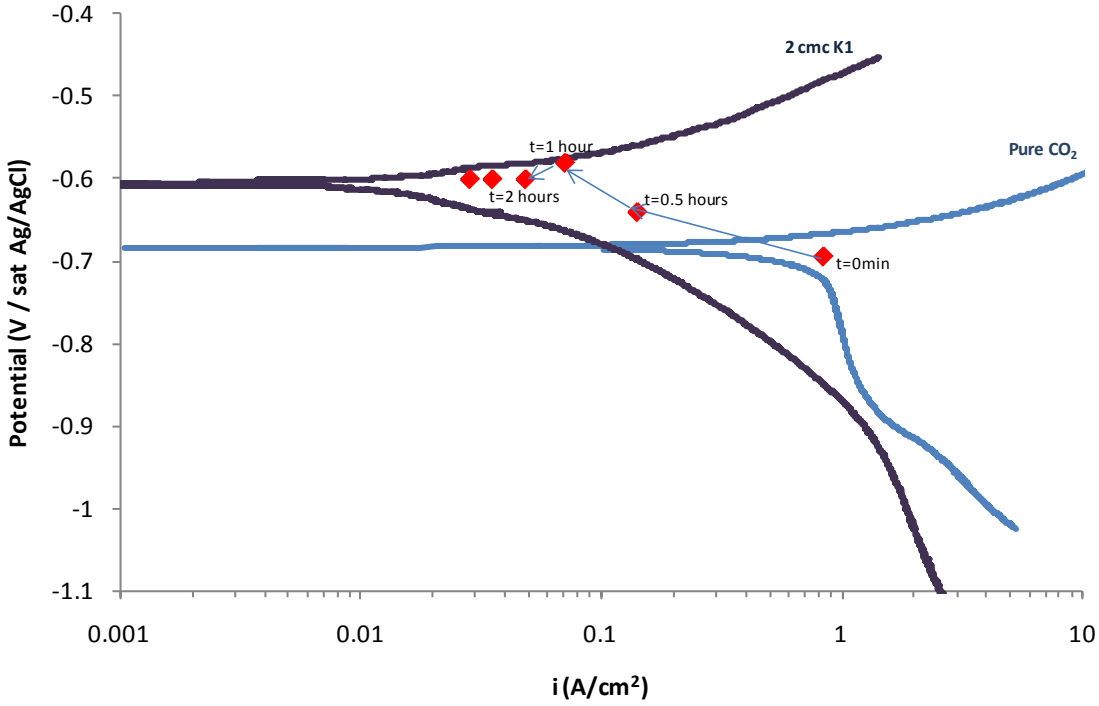

Figure 17. Pseudo polarization curve for inhibitor K1 (TOFA/DETA imidazolinium) when the concentration is 2 cmc (pH 5.0, 25°C, 1000 rpm).

Figure 18 shows the adsorption of alkylbenzyl dimethyl ammonium chloride, labeled K2, onto a 1018 carbon steel surface. The corrosion rate was reduced from 1.02 mm/year to 0.15mm/year, achieving a corrosion inhibitor efficiency of 85%. The adsorption of K2 reached the maximum protection when the corrosion inhibitor 2xCMC, what is different to the imidazolinium type (K1) corrosion inhibitor. One possible explanation could be associated with the chain length of the corrosion inhibitor K2 (C_{12}-C_{14}), which influences the CMC and the corrosion inhibition efficiency as well. Alaei, *et*

al.[127], (2013), reported that "quat" type corrosion inhibitor with 12 carbon chain is ineffective to protect against CO_2 corrosion. Another possible reason that affects the inhibition performance is the shape of the micelle formed by the "quat" type corrosion inhibitor. Bosenberg, *et al.* [125], (in 2007) reported that the adsorption of "quats" on steel at 2xCMC form a combination of cylindrical micelles and bilayers in the protective film which is less effective than a pure bilayer. Therefore, the initial adsorbed molecules of K2 (Figure 18) are not arranged in a compact bilayer on the steel surface. Therefore for "quat" type corrosion inhibitor it is needed to have 2xCMC to reach the optimal inhibition state.

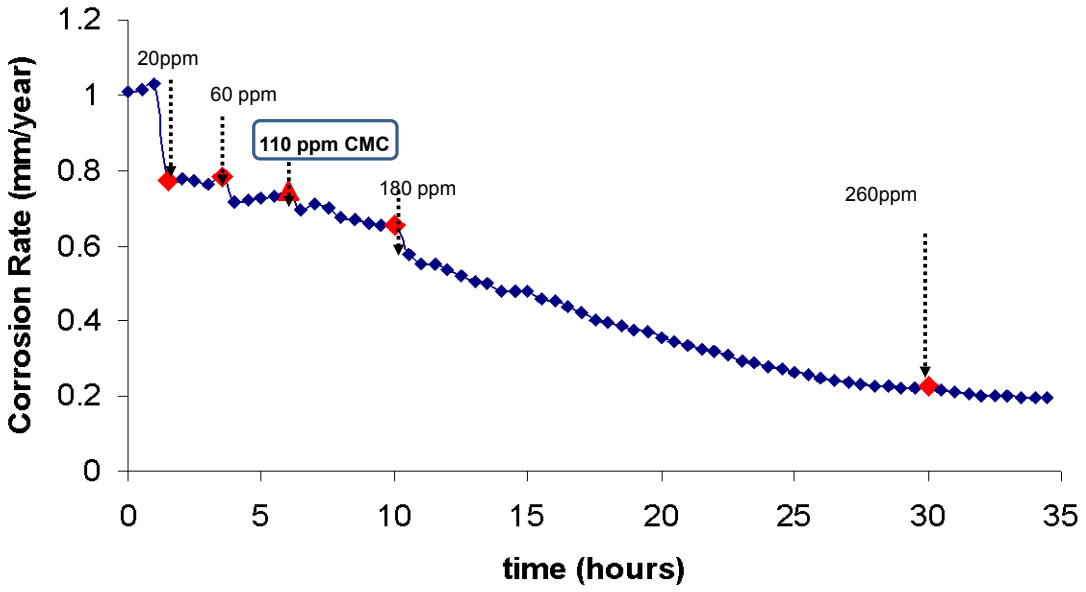

Figure 18. Corrosion rate (LPR - glass cell) with subsequent additions of inhibitor K2 (alkylbenzyl dimethyl ammonium chloride CMC- 110 ppm) (pH 5.0, 25°C, 1000rpm and pCO_2=0.98 bar).

Figure 19 shows the potentiodynamic sweeps for different concentrations of corrosion inhibitor K2 (0.5x, 1x and 2xCMC). The fact that the anodic slope does not change when the system has inhibitor in solution is because the corrosion mechanism does not change, and that the "quat" type inhibitor acts by geometric coverage of anodic active sites. When the concentration of the inhibitor in solution is 2xCMC the inhibitor film changes to form a spherical micelle, as reported by Knag, *et al.*[22], (2004) and Berek and Yurt[37] (2000).

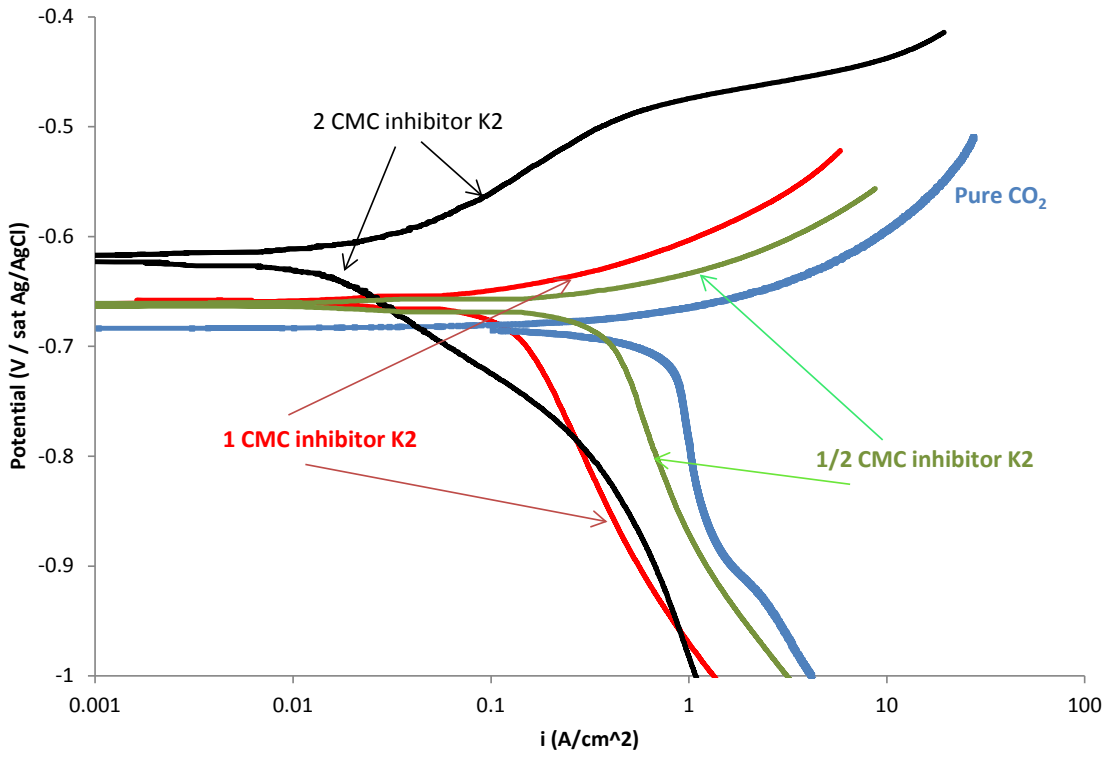

Figure 19. Electrochemical behavior of corrosion inhibitor K2 (benzylcocoalkyl dimethyl ammonium chloride) at different micelle concentrations (pH 5.0, 25°C, 1000 rpm).

Figure 20 shows the corrosion rate point trajectory plot for inhibitor K2 when twice CMC is in the system, which is in general similar to what was seen with K1. The quick change in the corrosion potential, as well as the reduction of the corrosion current, is evidence of the formation of a protective inhibitor film on the steel surface. This change of -0.06 V in the anodic direction suggests physisorption as the first stage of the adsorption process followed by a formation of micelles with a major interaction between the tails of the molecules. In the previous figure it was observed that the addition inhibitor does not reflect a change in the anodic slope, also the potential is just slightly shifted to a more anodic region. This suggests that inhibitor K2 works by geometrical blockage of anodic sites.

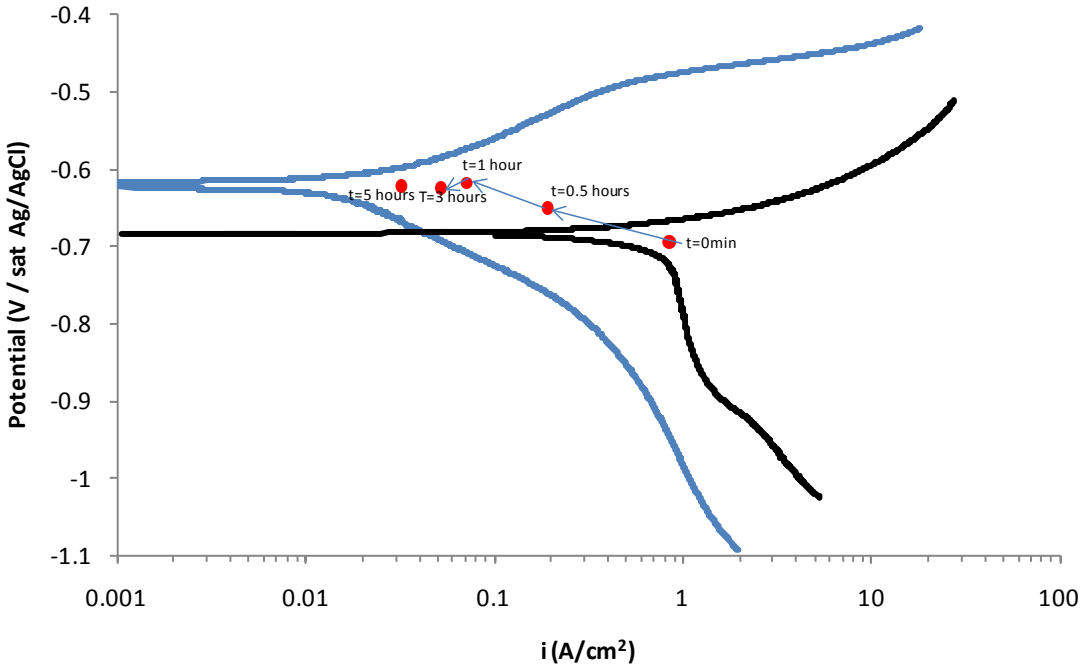

Figure 20. Corrosion rate point trajectory curve for inhibitor K2 (benzylcocoalkyl dimethyl ammonium chloride) when the concentration is 2 cmc (pH 5.0, 25°C, 1000 rpm).

It is generally accepted that immediately after the hydrophilic steel surface comes in contact with an aqueous environment the water molecules are oriented parallel to the steel surface, with their positive dipolar charge (terminal hydrogen atoms) facing the steel surface and the more negative central oxygen atom facing towards the solution. The (cationic) corrosion inhibitor added to the system then is attracted to the steel surface, and displace the water molecules from the surface to preferentially adsorb at the surface. However, at this point the efficiency of corrosion inhibition is low. As the surface coverage increases a layer is formed; the transformation of the layer to form different aggregations - micelles makes inhibitor film more protective and resistant.

Figure 21 shows the concentration (10-15 ppm) at which sodium thiosulfate, labeled K3, acquired the maximum corrosion inhibition. Subsequent additions of corrosion inhibitor K3 were made without further effect. At this concentration the corrosion rate of the carbon steel was reduced from 1.1 mm/year to 0.03 mm/year, representing a corrosion inhibitor efficiency of 97%.

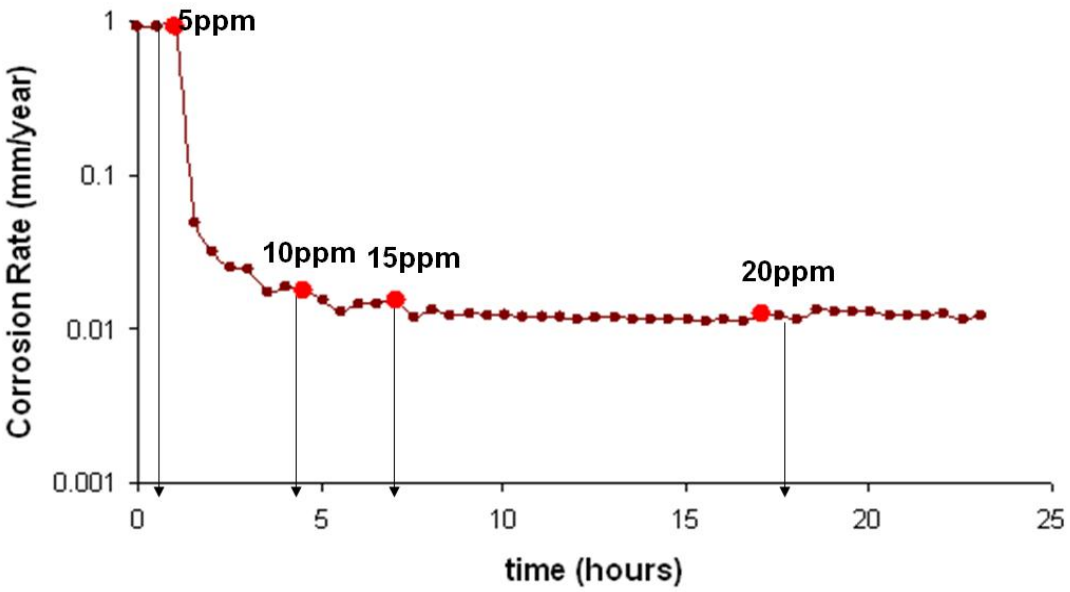

Figure 21. Corrosion rate (LPR - glass cell) with subsequent additions of inhibitor K3 (sodium thiosulfate) (pH 5.0, 25°C, 1000rpm and pCO_2=0.98 bar).

Figure 22 shows the potentiodynamical sweep for the corrosion inhibitor K3 sodium thiosulfate, showing a major reduction in corrosion rate as was reported by Kappes, *et al.* [54], (2012) and Ezuber[40] (2009) . In this particular case, according to the published work, sodium thiosulfate can be reduced at the steel surface to form H_2S which goes on to react with iron to form a thick scale of iron sulfide; this is very protective and

adherent to the metal[128]. Kappes *et al.*[54,55], (2012) conclude that the iron sulfide growths faster when the steel is immersed in acidic thiosulfate solutions than when the steel is under H_2S saturated solutions. EDS analysis, figure 23, of and iron surface exposed to the inhibitor K3 (thiosulfate ion) showed the presence of sulfur at the iron surface.

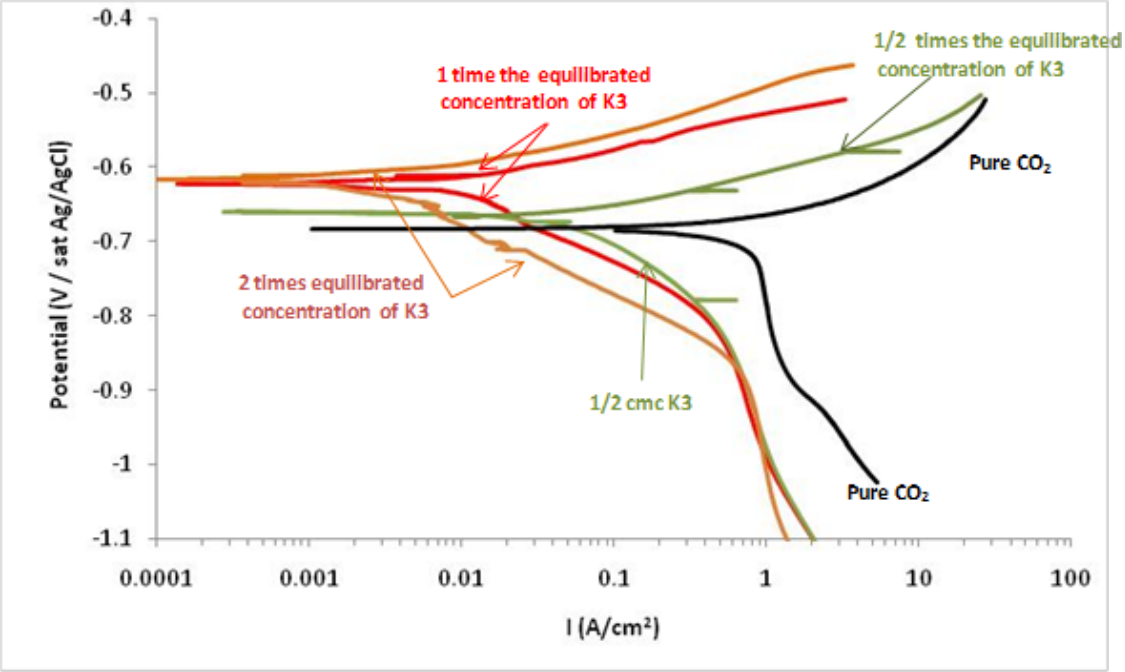

Figure 22. Electrochemical behavior of corrosion inhibitor K3 at different concentrations (equilibrated concentration =15ppm)

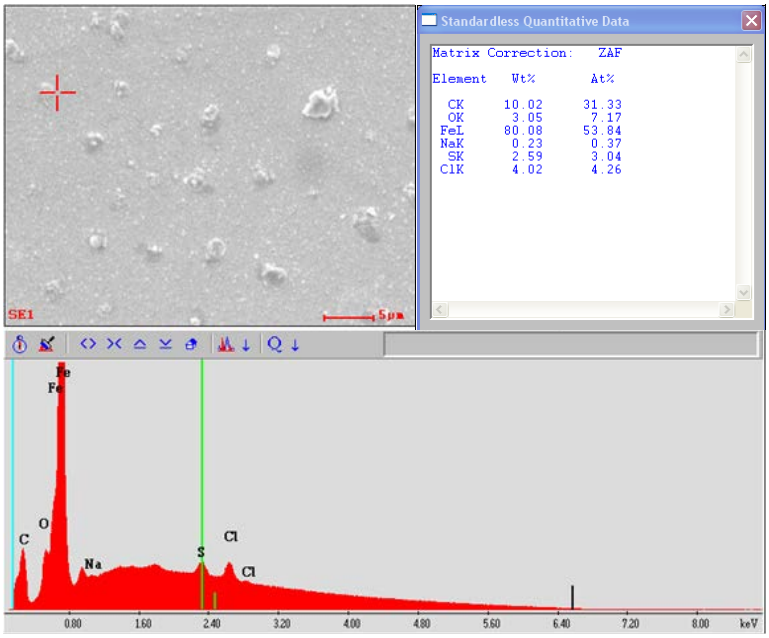

Figure 23. EDS analysis for iron surface exposed to 30ppm of inhibitor K3 (sodium thiosulfate) (pH 5.0, 25°C, and pCO2=0.98 bar).

The potentiodynamic sweeps show that the anodic reaction is strongly influenced by the addition of the inhibitor K3, reducing the corrosion reaction by three orders of magnitude. When the system has 7 ppm of inhibitor K3, which represents half the concentration at which the corrosion rate reaches the stable value (0.003 mm/year), the anodic reaction is reduced 2 or 3 times. The cathodic reaction was only slightly affected when the inhibitor K3 was in the system as it was under limiting current control.

Inhibitor labeled K4 is a mixture between inhibitor K1 and inhibitor K3 (20% TOFA/DETA imidazolinium and 4% sodium thiosulfate), with the idea to look into the combined effect in different corrosion scenarios, such as high flow velocity systems. In this combined system, the inhibitor K3 reacts and forms a layer of iron sulfide that has been hypothesized to “help” in the consecutive adsorption of the organic compound.

Figure 24 shows the EDS analysis of the comparison between inhibitor K3 (black line in the figure) and inhibitor K4 on iron surface. In the same way as inhibitor K3 inhibitor K4 showed the presence of sulfur at the iron surface.

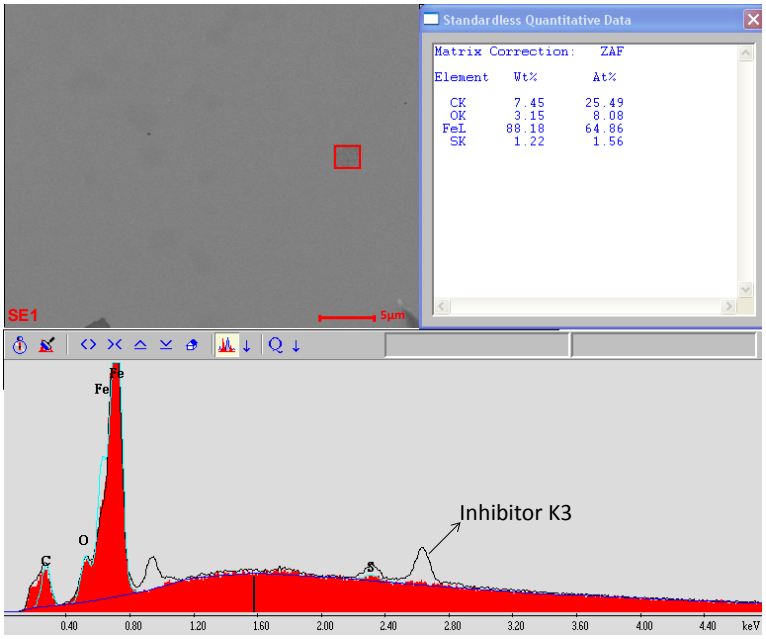

Figure 24 EDS analysis for iron surface exposed to inhibitor K4 (TOFA/DETA imidazolinium + sodium thiosulfate) (pH 5.0, 25°C, and pCO2=0.98 bar).

Figure 25 shows the potentiodynamical sweep in the presence of K4 inhibitor. The sweep shows that the addition of a small amount of inhibitor K3 to the organic compound reduces the corrosion rate by more than one order of magnitude compared to inhibitor K1. The change in current density represents an increase in the efficiency from 93% to 99%, providing evidence of an additive effect between these two compounds.

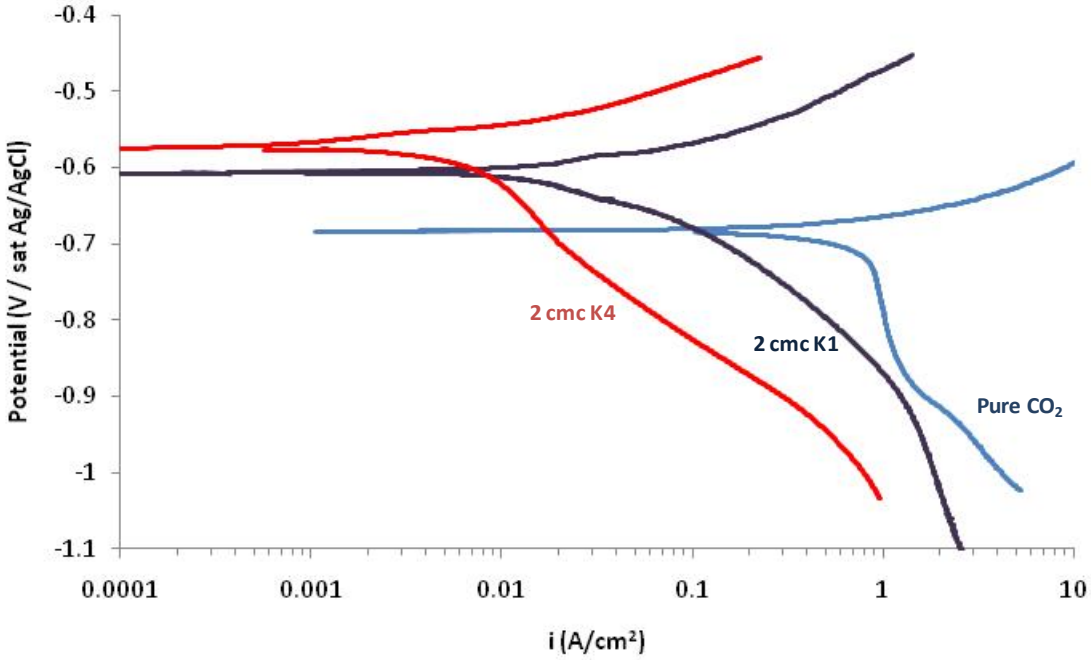

Figure 25. Effect of inhibitor K4 (which is a combination of K1 and K3) compared to inhibitor K1 alone.

Figure 26 shows the potentiodynamic polarization curve of inhibitor K5, which is a mixture between inhibitor K2 and inhibitor K3, addition of inhibitor K3 improves the performance of inhibitor K2. While for inhibitor K2 the corrosion potential shifted to positive values to an order of 60 mV, inhibitor K5 shifted the potential to more anodic sites by 170 mV. The addition of inhibitor K3 into inhibitor K2 and its effect on the formation of protective films is not clearly understood. However, studies published by Kappes[53] (2011) and research carried out in the Institute of Corrosion of Multiphase Technology[128] reveal that small amounts of sulfide can lead to a reduction of the corrosion rate by the formation of a protective iron sulfide layer. The possible formation of such a layer over areas sites that are not fully covered by the inhibitor molecules could

then improve coverage of the steel surface. The blend between inhibitor K2 and K3 improves the performance of the corrosion inhibitor package as evidenced by its reduction of the current density by two orders of magnitude.

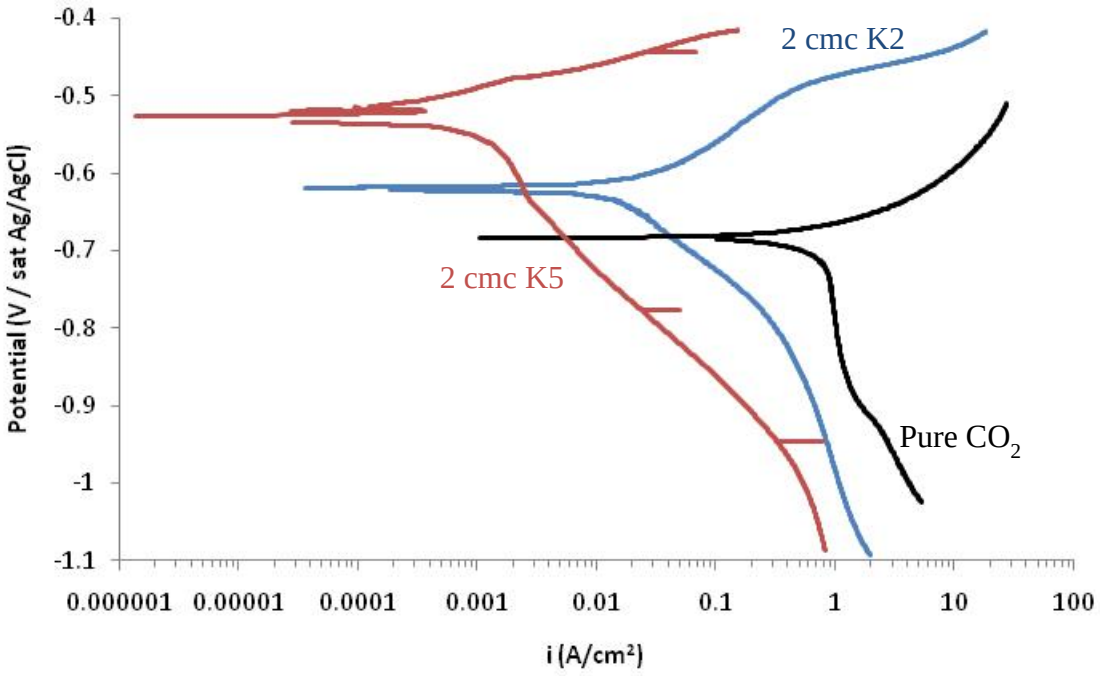

Figure 26. Effect of inhibitor K5 (which is a combination of K2 inhibitor and K3 inhibitor) compared to K2 alone.

3.7 Adsorption Isotherms

A relationship between the amount of inhibitor adsorbed on the metal surface and the concentration in the bulk solution can be determined by adsorption isotherms. The adsorption process of the corrosion inhibitor on the steel surface could be represented by a chemical reaction as:

$CI_{(sln)} + S_{surface} \rightleftarrows CI_{(ads)}S_{surface}$ *Reaction 11*

where $CI_{(sln)}$ is the corrosion inhibitor in solution, $S_{surface}$ is a free space in the steel surface and $CI_{(ads)}S_{surface}$ represents a occupied site in the steel surface. Therefore the equilibrium could be rewritten as:

$$K_{ads} = \frac{xCI_{ads}S_{surface}}{xS_{surface}[CI]} \quad \text{Equation (13)}$$

where $xCI_{ads}S_{surface}$ represents the fraction of occupied sites in the surface; $xS_{surface}$ represents the free sites on the surface; and $[CI]$ is the corrosion inhibitor concentration. It is common to use the symbol θ to refer the $xCI_{ads}S_{surface}$ therefore $xS_{surface}$ = (1-θ), the Equation 13 can be rewrite as:

$$K_{ads}CI = \frac{\theta}{(1-\theta)} \quad \text{Equation (14)}$$

equation 14 is the Langmuir isotherm.

Measurements of the uniform corrosion rate were used to determine the inhibitor efficiency, as described above, and the degree of surface coverage (θ) by:

$$\theta = 1 - \frac{CR}{CR_0} \quad \text{Equation (15)}$$

where CR_o is the corrosion rate in the absence of corrosion inhibitor and CR is the corrosion rate calculated in the presence of corrosion inhibitors.

The adsorption constant (K_{ads}) can be determined as the slope of the linear relationship between the ratio of $\frac{\theta}{(1-\theta)}$ and the corrosion inhibitor concentration, based on the Langmuir isotherm. The Gibbs energy (ΔG_{ads}) can then be calculated as follows:

$$\Delta G^{\circ}_{ads} = -RT \cdot ln(K_{ads}) \quad \text{Equation (16)}$$

where R is the ideal gas constant and T is the absolute temperature.

Figure 27 shows the characteristic adsorption isotherm and the linear regression line for corrosion inhibitor K1. The simple Langmuir adsorption model fits this experimental data very well, obtaining a correlation coefficient of R^2=0.989. Figure 27 also shows the value of the adsorption constant ($1.93x10^{-5}$ mol/l). The Gibbs free energy value is also calculated, ΔG = -30.15 kJ/mol implying a spontaneous adsorption due to the large negative value, and also suggesting that the adsorption of the imidazolinium ion at the steel surface is somewhere in between electrostatic interaction between charged molecules, and chemisorption.

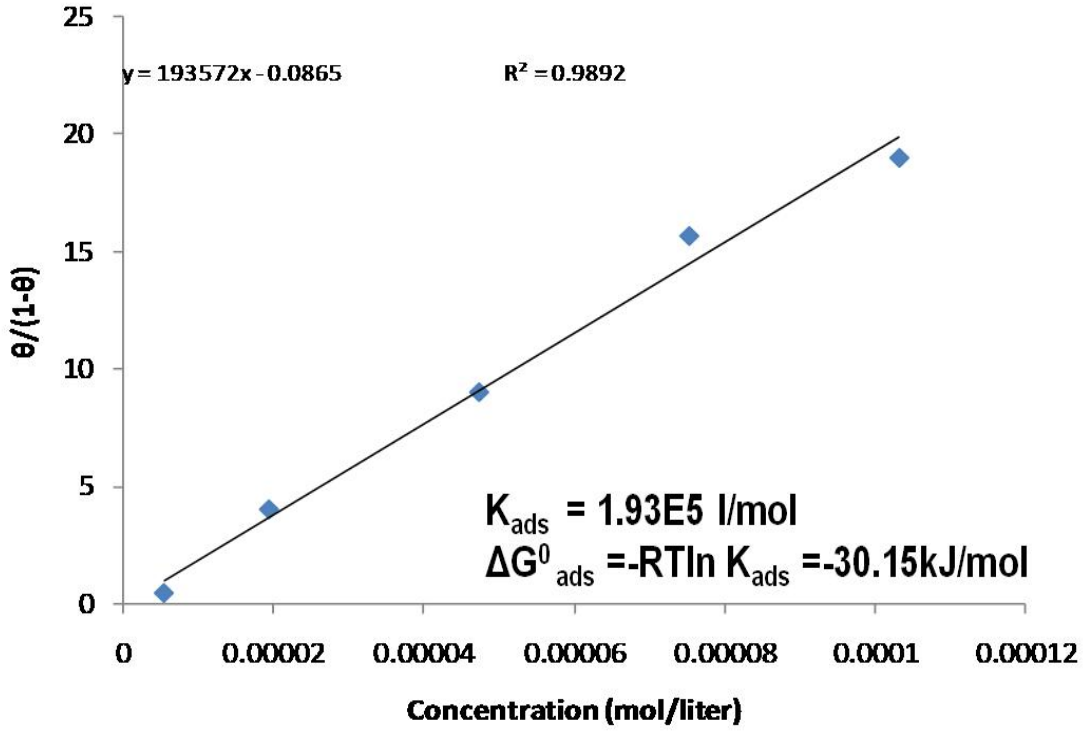

Figure 27. Adsorption isotherm for inhibitor K1 (pH 5.0, 25°C, 1000 rpm and pCO_2=0.98 bar).

The Gibbs energy can be compared with the force needed to remove a corrosion inhibitor molecule calculated with the atomic force microscope (AFM)[129]. The adsorption energy per molecule for K1 is:

$$\Delta G^{\circ}_{ads} = \frac{-30.15\frac{kJ}{mol}}{6.02\times10^{23}\frac{molecule}{mol}} = -5\times10^{-20}\ \frac{J}{molecule} \qquad \text{Equation (17)}$$

The AFM is a powerful instrument to measure topography in the nanometer order of magnitude. The AFM generates the image by contacting the surface with a very small tip located on a sensitive cantilever. Bouncing from the back of the cantilever a laser beam is directed towards a photodetector which converts the physical deflection into a electrical signal. With the use of the AFM it is also possible measure the forces needed to remove the molecules from a surface. Adsorption force of organic corrosion inhibitors has been measured and the micellar structure identified by the use of the AFM as reported in the open literature [125,130]. Xiong, *et al.* [130],(2014) quantified the force required to penetrate a corrosion inhibitor film using the AFM. They reported a force in the range of 10^{-9} N equivalent to a shear stress of 10^{6} Pa.

The force required to remove a corrosion inhibitor could here be approximated by combining the Gibbs energy definition:

$$-\Delta G = W_{a,rev} \qquad \text{Equation (18)}$$

where $W_{a,rev}$ is the maximum work. The work is defined as the force that is applied for the AFM in the inhibitor film times the length of the corrosion inhibitor, which is the distance that the AFM tip travels to touch the steel surface:

$$-\Delta G = W_{a,rev} = F^{*}l_{(hydrocarbon)} \qquad \text{Equation (19)}$$

Therefore the force required to remove the corrosion inhibitor could be estimated as

$$\boldsymbol{F} = \frac{-\Delta G}{l_{hydrocarbon}} = \frac{5\times10^{-20}\ J}{2\times10^{-9}\ m} = .025\ nN \qquad \text{Equation (20)}$$

An hydrocarbon chains in solution form a zig-zag arrangement when are in their most stable state [131]. According to Small[131], (1984) the distance between carbon atoms in a zig-zag arrangement is around 0.1533 nm with an angle between them of 109 ° - 112 °. The distance between every second carbon is 0.255 nm. Based on this assumption the approximate length of corrosion inhibitor, with a chain length of 18C, is $2x10^{-9}$ m. This length represents the distance that the AFM tip needs to travel through the corrosion inhibitor film to the substrate.

Mcmahon[132] (1991) reported that imidazoline molecule covers an iron surface area of 0.65 nm^2. If the area of the AFM tip[129] is approximately hundreds of nm^2 the approximate number of molecules in contact with the AFM tip should be in the range of thousand of molecules. For example, if the tip is in contact with approximately 1000 molecules then the penetration force is in the ***nN* scale**, which is in the range of the penetration force calculated from AFM as shown in Figure 28.

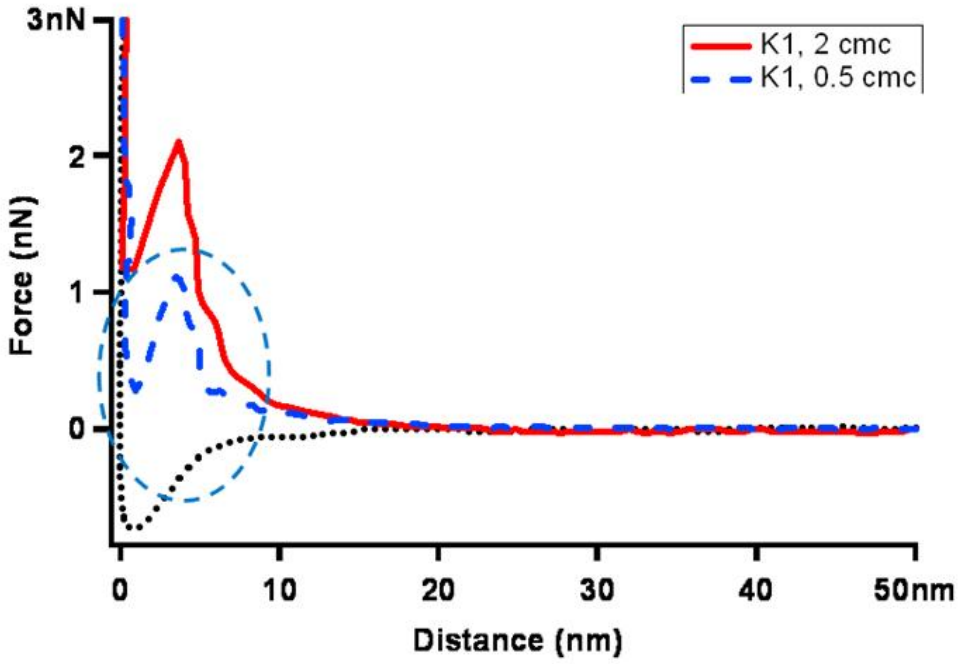

Figure 28. Penetration force for inhibitor K1 [129].

For corrosion inhibitor K1 a monolayer was observed with the AFM when the concentration was half the CMC and a bilayer when reaches the CMC as shown in Figure 29 (a) and (b).

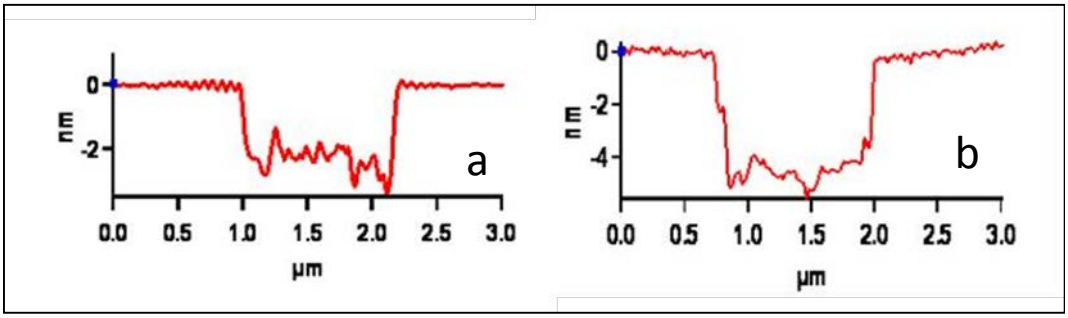

Figure 29 Thickness of corrosion inhibitor film K1 at concentrations equal to (a) ½ CMC and (b) 2 CMC (pH 5.0, 25°C and pCO_2=0.98 bar) [129].

In order to have a monolayer (as reported by Xiong[129] (2001) at 0.5CMC) of corrosion inhibitor K1 (adsorbing diameter in the order 10^{-9} nm^2) on the quartz crystal (Area = 4 x 10^{-4} m^2) it is necessary to have approximately 10^{14} molecules, this represents an approximated gain mass of one order of magnitude of $\mu g/cm^2$. Figure 30 shows that the measured mass gain for 0.5CMC (18 ppm) is 1.57 $\mu g/cm^2$, which is in acceptable agreement with the approximated value calculated for mass per unit area. It is likely that when the corrosion inhibitor K1 reached the maximum adsorption mass of 3$\mu g/cm^2$, this indicates formation of a bilayer on the steel surface.

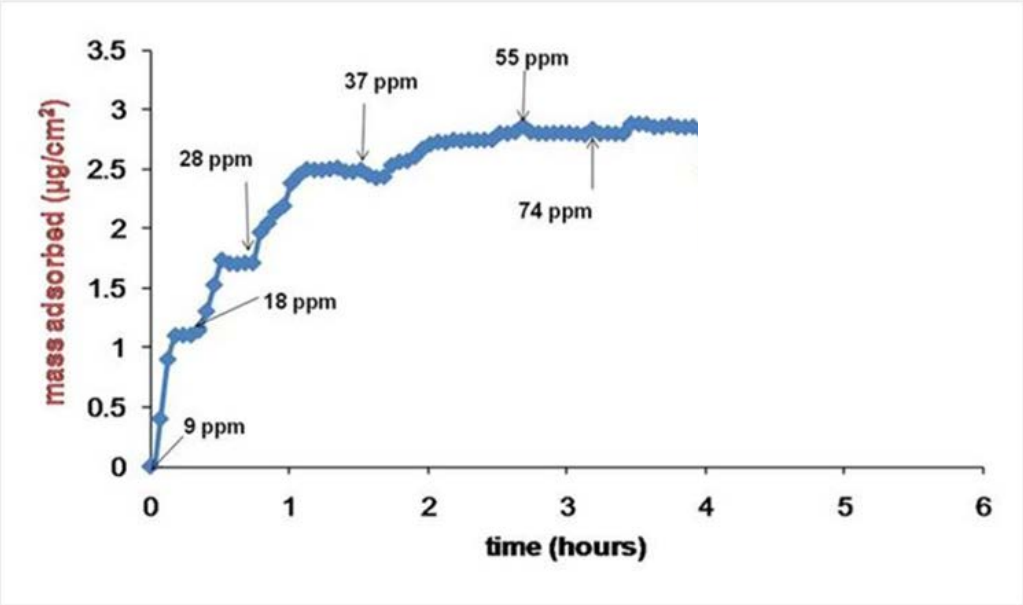

Figure 30. Adsorption of corrosion inhibitor K1 on iron coated quartz crystal substrate (pH 5.0, 25°C and pCO_2=0.98 bar CMC 36ppm).

Figure 31 shows the K_{ads} and the Gibbs energy of adsorption (ΔG_{ads}) for inhibitor K2. The negative value in the calculated ΔG represents a spontaneous adsorption with an

electrostatic bonding between steel surface and charged alkylbenzyldymethylammonium chloride surfactant.

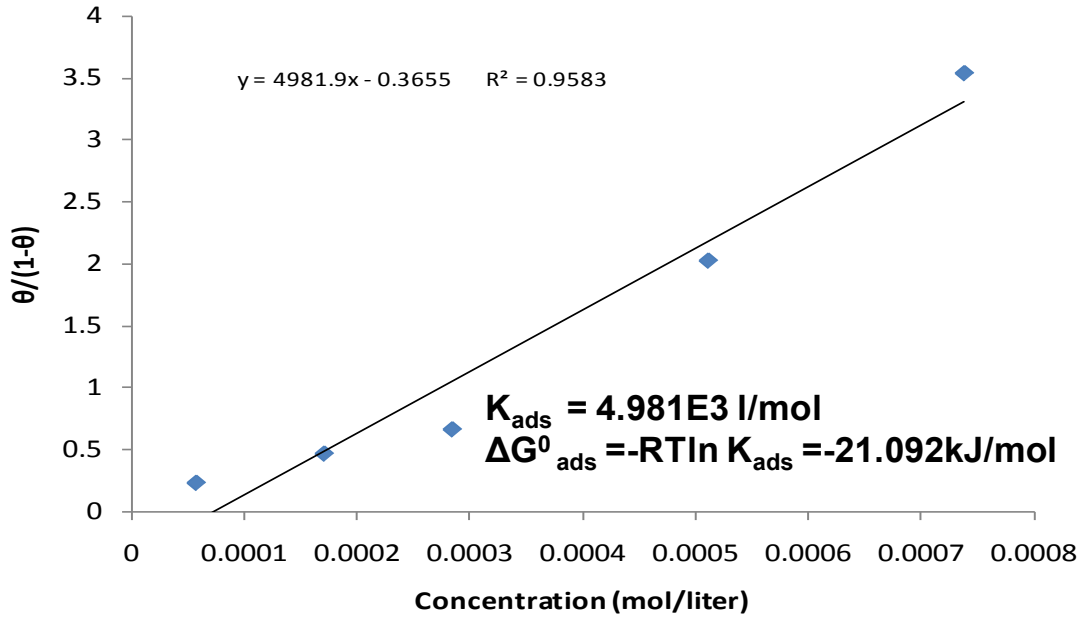

Figure 31. Adsorption isotherm for inhibitor K2 (pH 5.0, 25°C, 1000rpm and pCO_2=0.98 bar).

The adsorption energy for a single corrosion inhibitor molecule is

$$\Delta G^{\circ}_{ads} = \frac{-21.092 \frac{kJ}{mol}}{6.02 \times 10^{23} \frac{molecule}{mol}} = -3.5 \times 10^{-20} \frac{J}{molecule} \qquad \text{Equation (21)}$$

As was reported by Small[131] (1984) the change in the angles and distances between different hydrocarbon chains does not vary significantly, therefore, we could follow the same approach used for inhibitor K1 to calculate inhibitor K2, which has only

16 carbons in its chain. The length of corrosion inhibitor K2 is 1.7 nm, which also is the distance that the AFM tip needs to travel in order to reach the steel surface.

If this free energy of adsorption is converted into a force, following the same approximation than with inhibitor K1, then the force necessary to remove one corrosion inhibitor molecule is:

$$F = \frac{3.5x10^{-20}\ \frac{J}{molecule}}{1.7x10^{-9}\ m} = 0.02\ \frac{nN}{molecule}$$ Equation 22

According to Knag, *et al.*[22],(2004) "quat" type corrosion inhibitors adsorb as micelles in the surfaces with a typical area of 0.6nm^2. Therefore, the AFM tip is in contact with a thousand of inhibitor molecules, then penetration force is in the order of magnitude of ***nN*** which remains in the range determined for corrosion inhibitor K1 (27 nN).

Figure 32 shows the corrosion inhibitor adsorption on an EQCM iron coated quartz crystal. The results show that for 0.5CMC (55 ppm) the mass adsorbed onto the crystal is 2 μg/cm^2. Therefore, the monolayer should be expected when the system is around order of magnitude in μg/cm^2 for inhibitor K2.

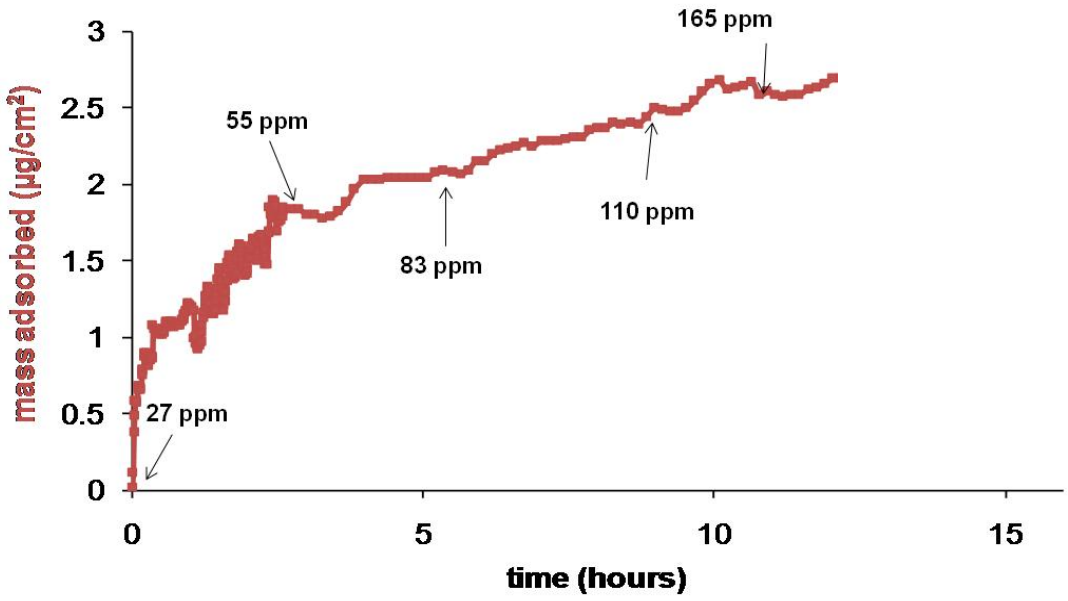

Figure 32. Adsorption of corrosion inhibitor K2 on iron coated quartz crystal substrate (pH 5.0, 25°C and pCO_2=0.98 bar, CMC 110 ppm).

Measurements performed on an AFM[129] for the corrosion inhibitor K2 showed that at half CMC a monolayer film is seen, Figure 32(a). When the inhibitor concentration is twice the CMC the film detected was of semi-micelle type, Figure 32(b). When the system had a corrosion inhibitor concentration above the CMC, the mass recorded was 2.7 µg/cm^2. It is then valid to assume that the film of inhibitor K2 adsorbed onto the iron coated quartz crystal is not a full double layer film; instead the film corresponds to a spherical micelle film as represented in Figure 3, as was reported by Xiong (2011) with the AFM[129].

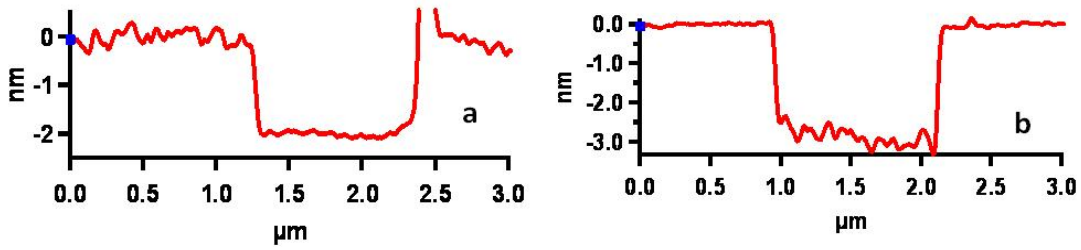

Figure 33. Thickness of corrosion inhibitor film K2 (a) ½ CMC (b) 2 CMC (pH 5.0, 25°C and pCO_2=0.98 bar) [129].

Figure 34 shows the relationship between coverage and inhibitor concentration for corrosion inhibitor K3. The relationship follows the Langmuir adsorption model (a correlation coefficient of R^2= 0.969) even if the mechanism of attachment of K3 to the steel surface is different. In this case, the decomposition of the thiosulfate which is in K3 ion in the steel surface to produce H_2S and further form a FeS film is the main reason of the corrosion protection. The thiosulfate results in formation of a passive layer that reduces the corrosion as was reported by Kappes *et al.* [54], (2012). High concentration of thiosulfate can represent a very thick iron sulfide layer which is detectable as a clear mass gain in Figure 35.

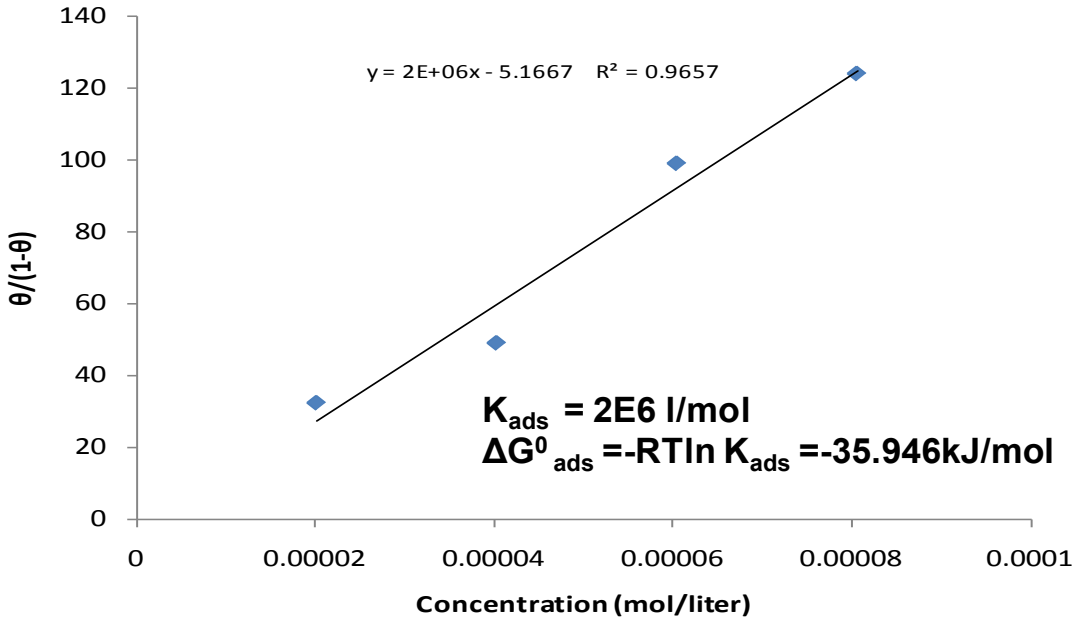

Figure 34. Binding energy for inhibitor K3 (pH 5.0, 25°C, 1000rpm and pCO_2=0.98 bar).

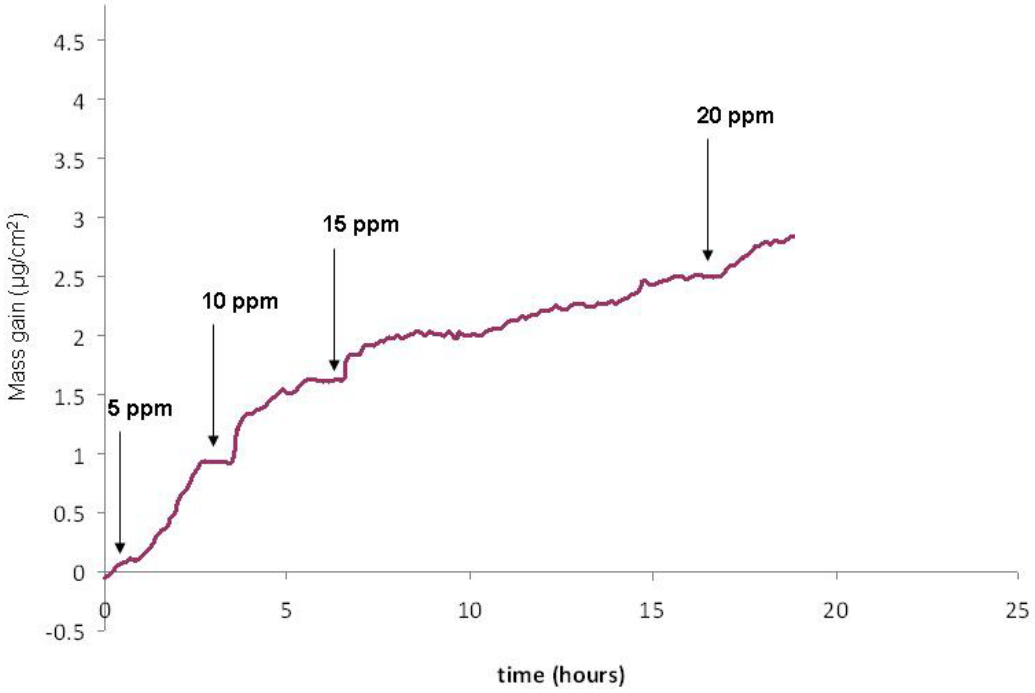

Figure 35. Adsorption of corrosion inhibitor K3 on iron coated quartz crystal substrate (pH 5.0, 25°C and pCO_2=0.98 bar).

Figure 36 show the adsorption of corrosion inhibitor K4 (which is a combination of K1+K3) on an iron coated quartz crystal. The results reveal that when the system reaches the cmc (210 ppm) the mass adsorbed was 4.0 µg/cm^2. When the system has a concentration above 1xCMC the adsorbed mass does not increase significantly. This means that the surface coverage is not improved by an increase in the concentration of inhibitor K4 once the system had reached the critical micelle concentration, similar to what was seen with K1.

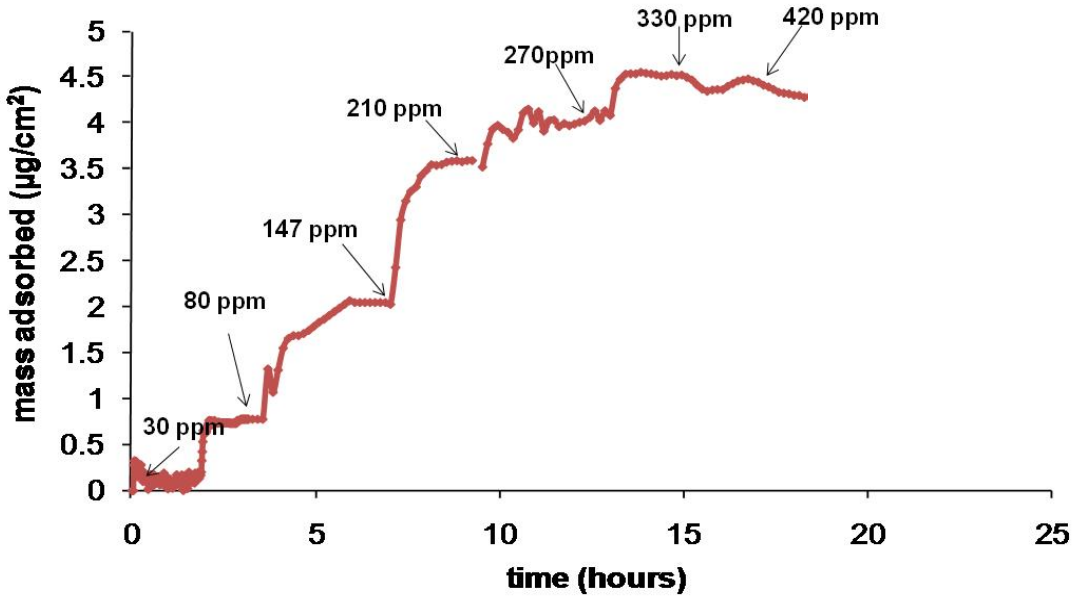

Figure 36. Adsorption of corrosion inhibitor K4 on an iron coated quartz crystal substrate (pH 5.0, 25°C and pCO_2=0.98 bar).

Results reported by Xiong[129], (2011) with the AFM showed that corrosion inhibitor film developed with inhibitor K4 has a similar characteristic to that developed with inhibitor K1. Figure 37 shows the thickness of inhibitor K4 using an AFM. The thickness of the corrosion inhibitor film corresponds to a bi-layer film, in a similar way as for inhibitor K1.

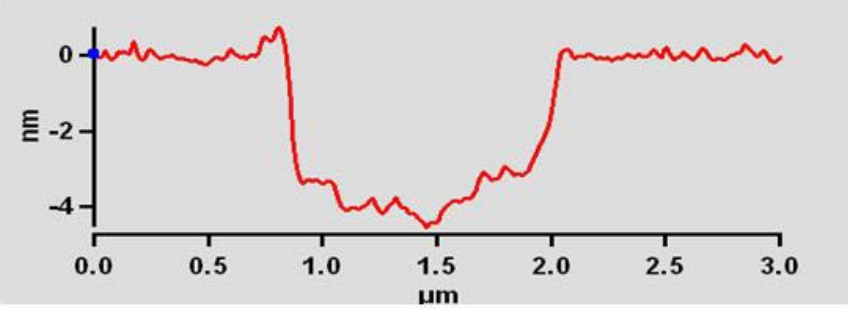

Figure 37. Thickness of corrosion inhibitor film K4 at 2 cmc on mica (pH 5.0, 25°C and pCO_2=0.98 bar) [129].

Figure 38 shows the corrosion inhibitor adsorption of corrosion inhibitor K5 (which is a combination of K2+K3) on a quartz crystal microbalance with an iron coated quartz crystal. The results showed that at cmc (290 ppm) the mass adsorbed on the crystal is 5.0 µg/cm^2, and that after this point the increase in concentration of inhibitor K5 does not change the mass adsorbed on the iron coated quartz crystal, similar to what was seen with K2. AFM measurements performed by Xiong[129], (2011) for the corrosion inhibitor K5 showed that the results are similar to those for inhibitor K2, see Figure 39.

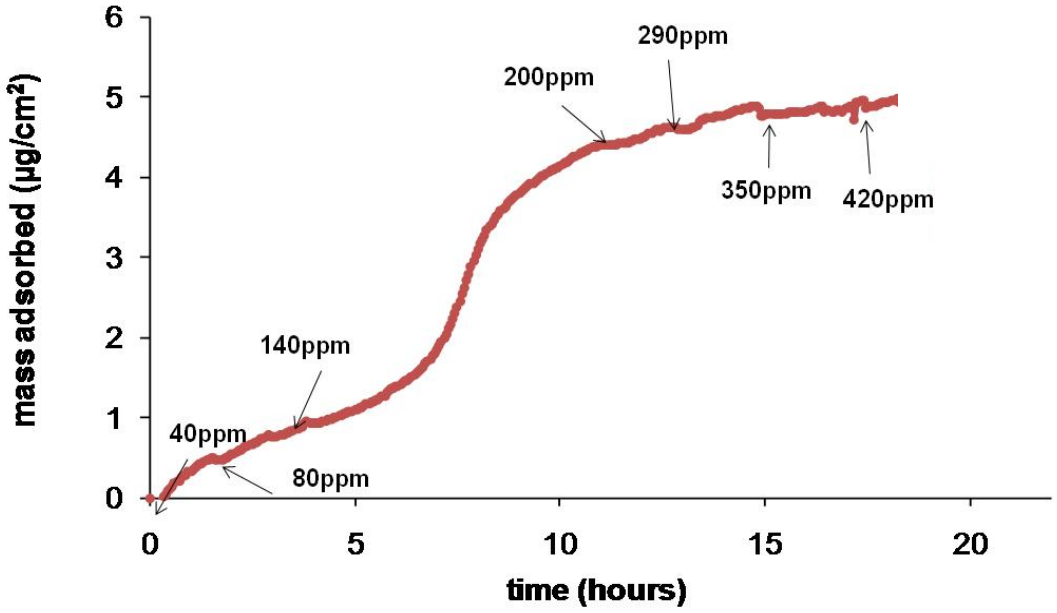

Figure 38. Adsorption of corrosion inhibitor K5 on iron coated quartz crystal substrate (pH 5.0, 25°C and pCO_2=0.98 bar).

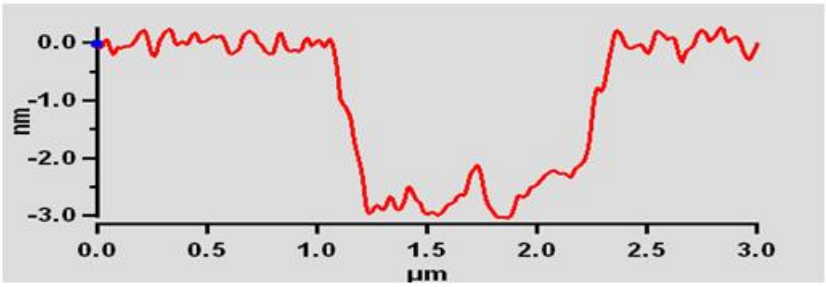

Figure 39. Thickness of corrosion inhibitor film K5 at 2 cmc on mica (pH 5.0, 25°C and pCO_2=0.98 bar) [129]

3.8 Summary

The formation of micelles on the surface close or above the CMC, improves the coverage of active corrosion sites. According to linear polarization measurements the

addition of twice the CMC of inhibitor K1 and K2 promoted the protection against corrosion.

The electrochemical sweeps did not indicate a change in the corrosion mechanism due to inhibitor presence. Rather the results suggest that the corrosion inhibitors act by superficially blocking of active sites on the steel surface.

The changes in the inhibition performance when the organic surfactants (K1 and K2) are blended with thiosulfate ion (K3) suggest an additive effect (Figure 23 and Figure 24). Sodium thiosulfate probably acts by forming a thin film of iron sulfide at the sites that are not covered by inhibitor molecules.

Adsorption of inhibitors K1 and K2 can be described by Langmuir adsorption isotherms. Even the coverage by inhibitor K3 which is not a surfactant appears to follow the same trend.

Binding energies showed distinguishable levels of interaction between the steel surface and the corresponding inhibitor. Thus quaternary alkyl ammonium compounds (K2) have the weakest interaction, with ΔG of physical adsorption around -21 kJ/mol. The imidazolinium ion showed a stronger interaction based on ΔG, somewhere in between physisorption and chemisorption at approximately -30 kJ/mol. Sodium thiosulfate showed the highest binding energy, closest to chemical adsorption, approximately -36 kJ/mol.

Chapter 4. Effect of Gas/Liquid Multiphase Flow on Corrosion Inhibitor Film Performance

4.1 Introduction

From the open literature review, two opposing conclusions can be made extracted the effect of flow on performance of thin protective inhibitor films. While many conclude that the flow directly affects inhibitor performance, others conclude that the actual change in performance is primarily related to factors other than flow. The most common hypothesis is that the intensity of a particularly violent type of gas/liquid flow – so called slug flow, can mechanically damage and even completely remove the corrosion product layer[48,93]. These reports have also suggested that, under a slug flow regime, the inhibitor is unable to become attached to the steel surface. It has also been reported that there is a critical wall shear stress above which the inhibitor film could be removed from the steel surface. In contrast, other authors did not find any effect of wall shear stress on the performance of thin protective inhibitor films[60,69,76]. These works reported that the inhibitor film failure was due other issues, e.g. ingress of contaminant species such as oxygen, loss of inhibitor availability, or as a result of higher corrosivity of the environment.

In order to quantify the effect of flow on inhibitor adoption and removal, one has to consider the effect of substrate used in the study. This can be best described by considering the charge of the metallic surface, which can be expressed using values for the *zero charge potential* vs. the corrosion potential. It has been reported[133–135] that when the difference between the corrosion potential and the zero charge potential is negative,

the metal becomes negatively charged and adsorption of cations is expected to happen, as shown in Figure 40. Table 5 tabulates the calculations of the difference between the corrosion potential and the zero charge potential for iron, gold and platinum. For iron the adsorption of cations at the surface is expected to be strongly favored. The consequences of this will be discussed in the text below.

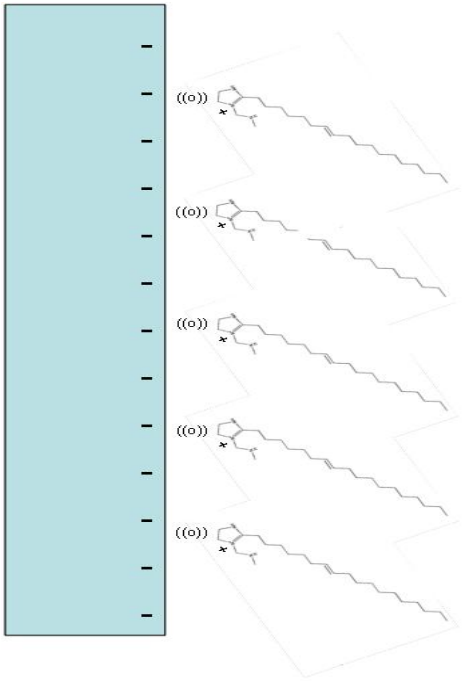

Figure 40. Adsorption of cationic inhibitors on negatively charged metallic surface.

Table 5. Difference between corrosion potential and zero charge potential for three different substrates.

Substrate	Corrosion potential vs. sat Ag/AgCl (pH 5.0, 25°C & pCO_2=0.98 bar) (experimental data)	Zero charge potential vs Hydrogen electrode (SHE) [136]	E_{corr}-E_{zero}
Iron	-720 mV	-350 mV (-620 mV vs sat Ag/AgCl)	-100 mV Negatively charged metal
Gold	-87 mV	+180 mV (-40 mV vs sat Ag/AgCl)	-47 mV Negatively charged metal
Platinum	-142 mV	+20 mV (-200 mV vs sat Ag/AgCl)	58 mV Positively charged metal

4.2 Objectives

The research objectives for the work described in this chapter were to:

- Determine the effect of high shear stress on the integrity of corrosion inhibitor films using an electrochemical quartz crystal microbalance (EQCM)
- Since it is common to do the EQCM measurements on platinum, establish if the substrate plays an important role in the adsorption/desorption process under flowing conditions.

4.3 Small Scale Experiments

4.3.1 Equipment

In order to measure the effect of hydrodynamic surface forces on inhibitor film performance, two sets of experiments were performed in a glass cell using a submerged jet impingement configuration.

In one set of experiments, the adsorption process of inhibitors was tested using an electrochemical quartz crystal microbalance (EQCM) with three different substrates -

metals coating the quartz crystal (gold, iron and platinum). Polarizations of metal surface to -900 mV *vs.* a saturated Ag/AgCl electrode were performed to: a) avoid corrosion of the iron coated crystal and to evaluate all three metal substrate electrodes at the same potential[137]. In the second set of experiments, electrochemical techniques were deployed using a rotating cylinder electrode.

In both tests, an impinging jet flow was applied directly to the electrode surface in order investigate the effect of wall shear stress on inhibitor film integrity. The jet was applied using three different methods: as submerged water jet, as a two-phase gas/liquid submerged jet containing CO_2 bubbles, and as a two-phase gas/liquid submerged jet carrying water vapor bubbles causing cavitation; for details see Table 6. The nozzle creating the jet was made from a glass tube ending in a 1 mm opening; it was oriented perpendicular to the test specimen surface. The 1 mm opening of the glass tube was set at a distance of 3 mm from the specimen surface. After 10 hours of inhibitor adsorption in quiescent conditions, the jet flow was applied for another 10 hours.

4.3.1.1 Mass Change Measurements Obtained Using EQCM

The mass gain due to inhibitor adsorption was measured using an electrochemical quartz crystal microbalance (EQCM), Figure 41. With the use of the EQCM it is possible to quantify any inhibitor loss due to flow by measuring the mass change of the inhibitor adsorbed on the substrate[138–140].The EQCM experimental cell design is shown in Figure 42.

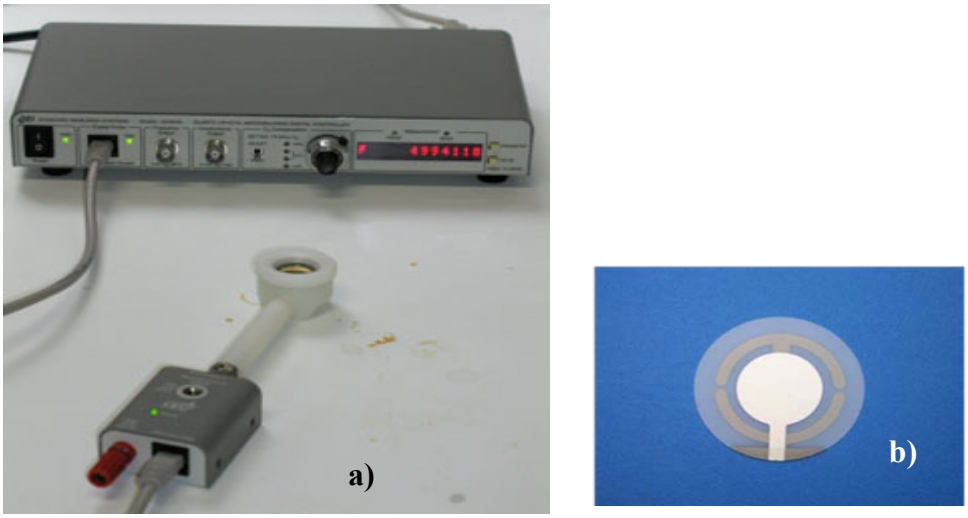

Figure 41. a) Electrochemical Quartz Crystal Microbalance (EQCM200 from Stanford Research System) b) Quartz crystal with unpolished platinum coated quartz crystal surface

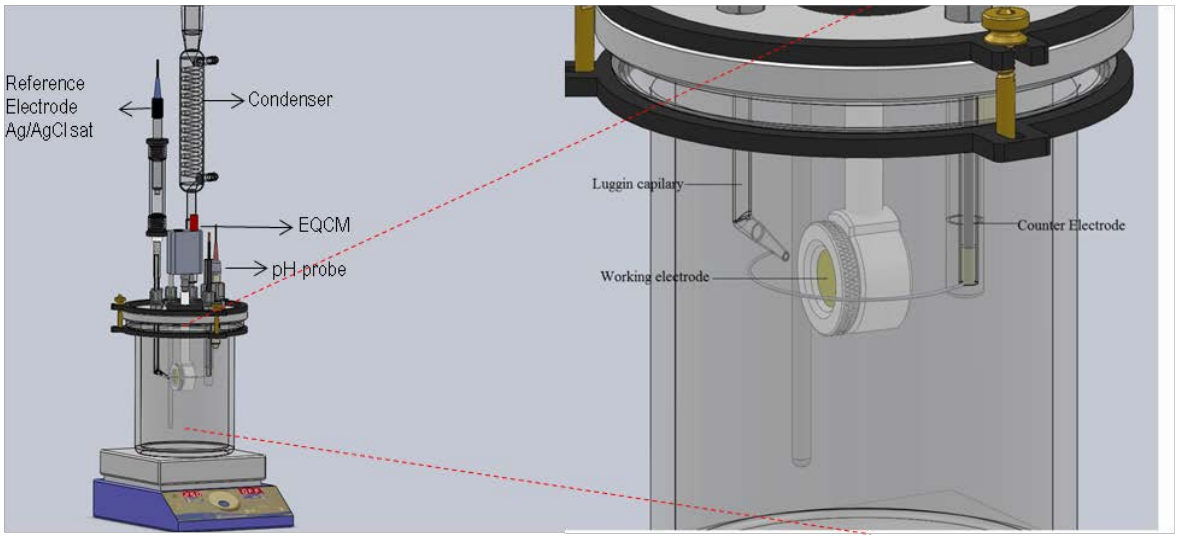

Figure 42. Electrochemical quartz cell microbalance immersed in solution. a three electrode set up to polarized the working electrode to -900 mv vs reference electrode (sat Ag/AgCl)

4.3.1.2 Electrochemical Measurements of Inhibitor Performance Using a Rotating Cylinder Electrode

In a corresponding series of experiments, inhibitor performance was evaluated using a similar setup with a submerged jet and a RCE as a target. Electrochemical measurements were done using a three electrode system. A cylindrical rotating specimen made from 1018 carbon steel was used as the working electrode, a concentric platinum wire was used as the counter electrode, and the silver-silver chloride reference electrode was connected externally *via* a Luggin capillary tube, see Figure 43.

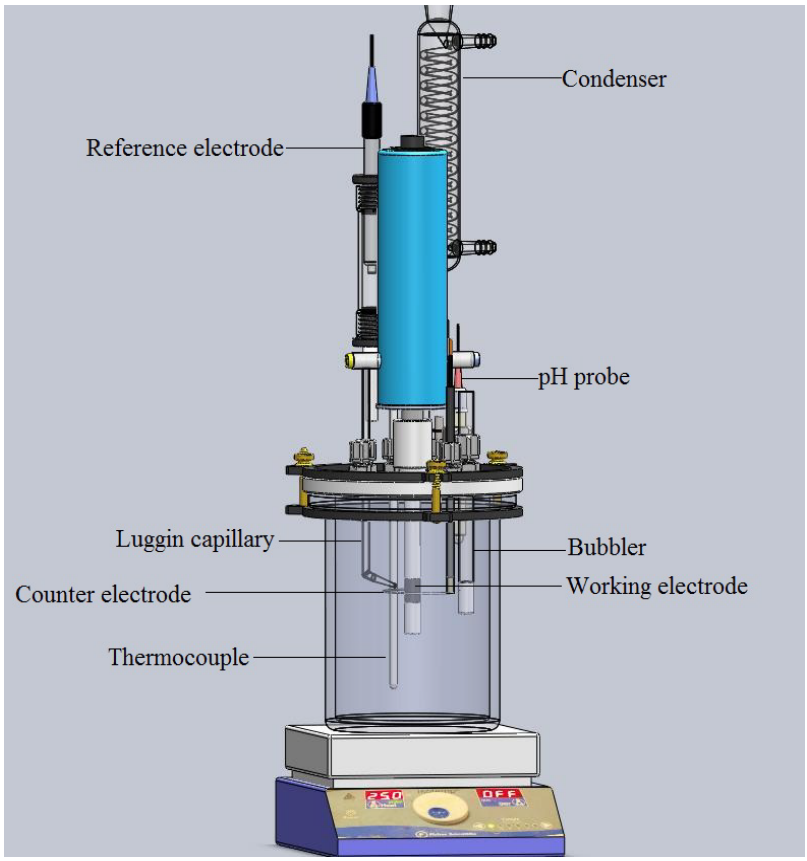

Figure 43. Electrochemical cell design – Rotating cylinder electrode (RCE)

4.3.2 Experimental Procedure

In both sets of experiments described above (EQCM and RCE), the glass cell was filled with de-ionized water and 1 wt.% NaCl. Carbon dioxide (CO_2) was bubbled into the system one hour before the beginning of the experiment with continuous bubbling during the entire experiment. At the beginning of the experiment, the pH was adjusted with deoxygenated $NaHCO_3$ solution and continuously measured. The corrosion inhibitor was added one hour after the working electrode was submerged into the system. The five different corrosion inhibitors K1, K2, K3, K4 and K5 (see Table 2) were tested in EQCM experiments with three different metal substrates (iron, gold and platinum). In RCE electrodes, the five different corrosion inhibitor formulations were tested for inhibition performance on mild steel. The corrosion inhibitors concentration was selected to be 2xCMC, as shown in Table 4. All the experiments were repeated twice, the most representative data are the ones reported on the figures presented below.

The submerged jet cavitation flow design was made by using an auxiliary glass cell containing boiling water, Figure 44. The water was boiled for around 2 hours in order to de-gas it. The cell with boiling water generated water vapor which was passed to the test cell through the tubing and eventually emerging as bubbles carried by the submerged jet. The vapor entering the lower temperature working solution in the main cell condensed, with the vapor bubbles collapsing, causing cavitation. It was expected that this cavitation near the surface of the RCE or EQCM led to fairly large mechanical forces being exerted on the surface of metal.

In the RCE setup, linear polarization resistance measurements were made in order to determine the corrosion rate. The scan rate was 0.125mV/s from -5mV to 5mV *vs.* the open circuit potential. The estimation of the current density was used with the Stern-Geary constant B value of 20.7 mV/dec. The solution resistance was measured using electrical impedance spectroscopy (EIS), and the LPR values were corrected manually thereafter.

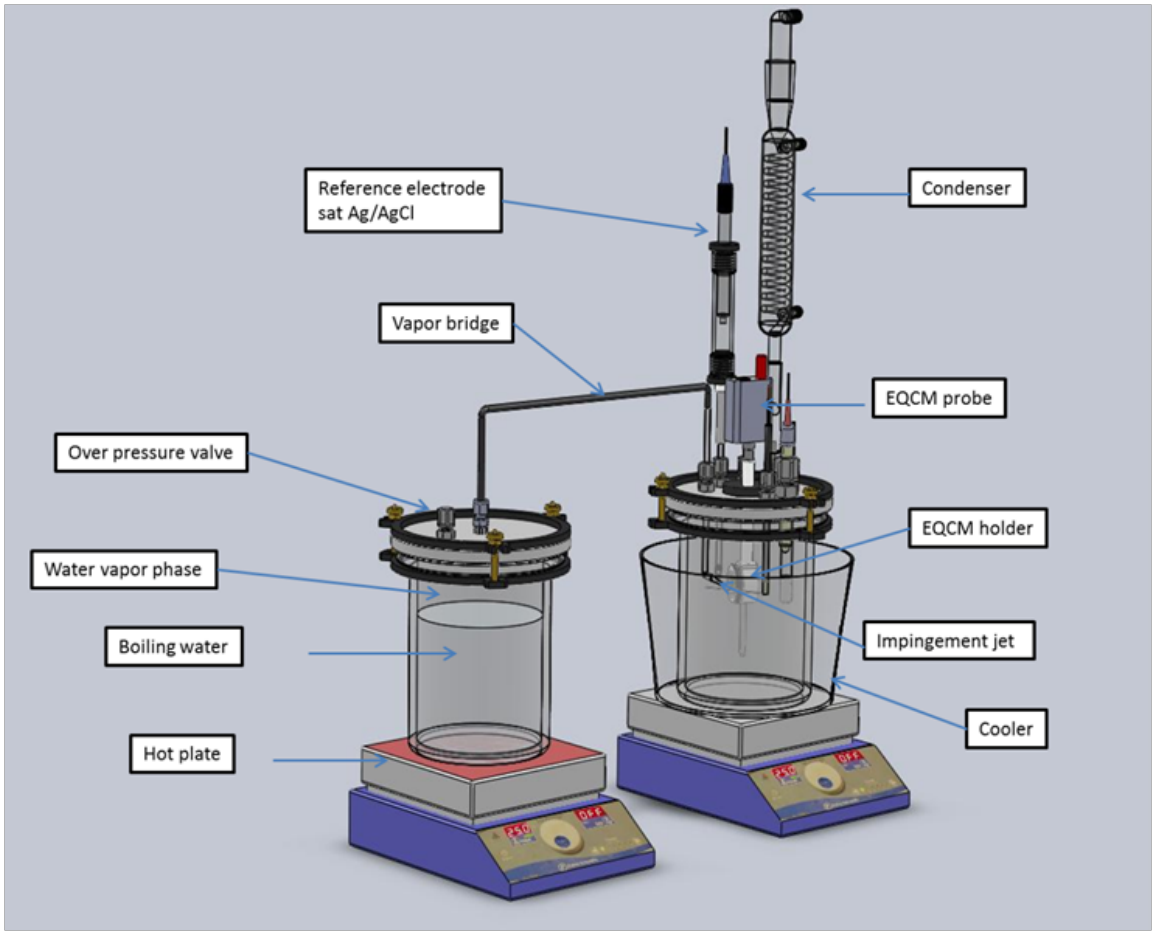

Figure 44. Water vapor cavitation setup.

4.3.3 Test Matrix

Table 6. Experimental conditions – Small scale experiments for gas/liquid multiphase flow

Test solution	1 wt. % NaCl
Temperature	25°C
Partial Pressure of CO_2	0.98 bar at 25°C
pH	5.0
Inhibitor Systems	K1, K2, K3, K4 and K5 (see Table 1 in Chapter 3)
Inhibitor concentration tested	2 CMC
Test material	Au, Fe and Pt coated quartz crystals (Polarized to -0.9 V vs. sat Ag/AgCl)
High shear stress on a EQCM	CO_2 bubble impact water jet vapor cavitation
Corrosion Rate Measurement	Linear Polarization Resistance (LPR)

4.3.4 Results and Discussion

The use of EQCM to measure the effect of high wall shear stress on inhibitor film performance was evaluated as follows. Figure 45 shows the baseline test checking for any effect of wall shear stress on the platinum coated quartz crystal in a system free of inhibitor. When CO_2 bubbles impacted the Pt coated crystal it seems that the perturbation was very small compared to the magnitude of mass change that was to be measured using this system. A submerged jet carrying CO_2 bubbles was applied for 2 hours. Subsequently, the system was allowed to recover for 2 hours; thereafter a submerged

water jet was applied at a velocity of 20 m/s, this corresponds to a calculated pressure of 1400 Pa at the center of the jet impact. It seems that even though there was some more perturbation of the measured signal, it remained small and the average value remained the value. When water vapor bubble cavitation was applied, a more significant change of in the EQCM response was registered. This change was most likely associated with the changes in temperature close to the metal surface due to impact of the hotter vapor bubbles and the water dragged by them.

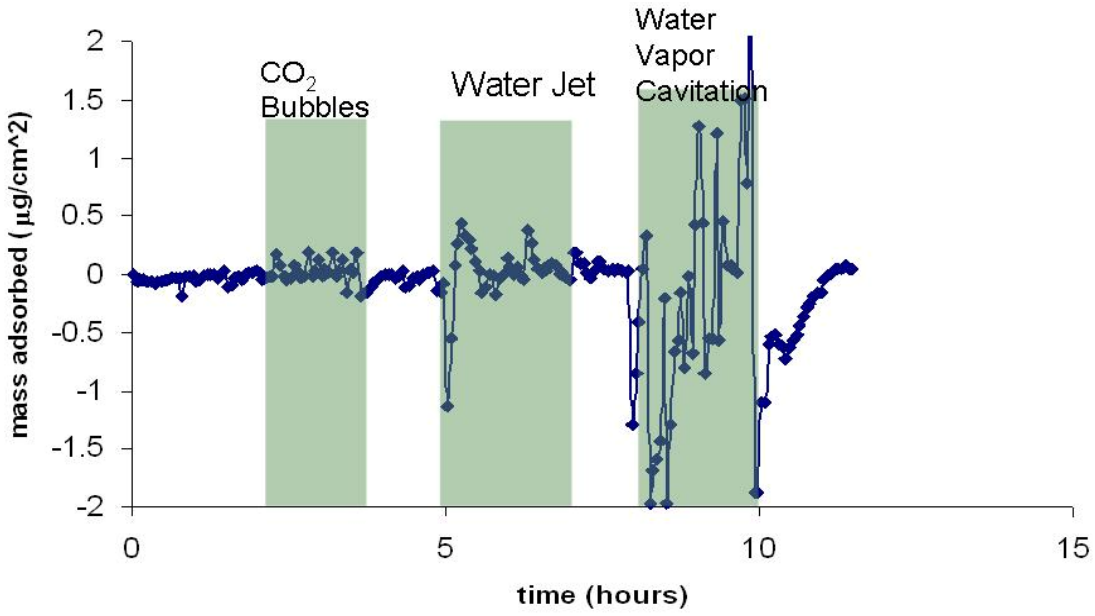

Figure 45. Use of EQCM for high wall shear stress on an unpolished platinum coated quartz crystal (pH 5.0, 25°C and pCO_2=0.98 bar).

The effect of different metal substrates on the adsorption of corrosion inhibitors is shown in Figure 46 for the adsorption of inhibitor K2 on an unpolarized Pt quartz crystal, as well as for three different polarized quartz crystals, coated with Fe, Au and Pt.

The inhibitor (2xCMC) was added 1 hour after the stabilization of the corresponding crystal in the uninhibited electrolyte. The adsorption process of the inhibitor was allowed to occur over the next 10 hours. The weakest adsorption of inhibitor K2 was at the unpolarized Pt surface, reaching an adsorbed mass of 0.5 $\mu g/cm^2$.

The polarized iron, platinum and gold crystals adsorbed more of inhibitor, 2-3 $\mu g/cm^2$. The adsorbed inhibitor films were then exposed to the high wall shear stress by applying a submerged jet carrying CO_2 gas bubbles. The mass adsorbed on all the three surfaces increased.

Inhibitor adsorption theory and zero charge potential data can be used to interpret some of the experimental observations. The least favorable material for adsorption of inhibitor molecules was the unpolarized platinum surface due to its high potential (see Table 4) which did not favor adsorption of a cationic inhibitor. Reducing the potential of platinum resulted in better adsorption of inhibitor. On the other hand, it is not clear why the adsorption of inhibitor increased with application of the impinging jet flow, when according to many previous studies, the decrease was to be expected.

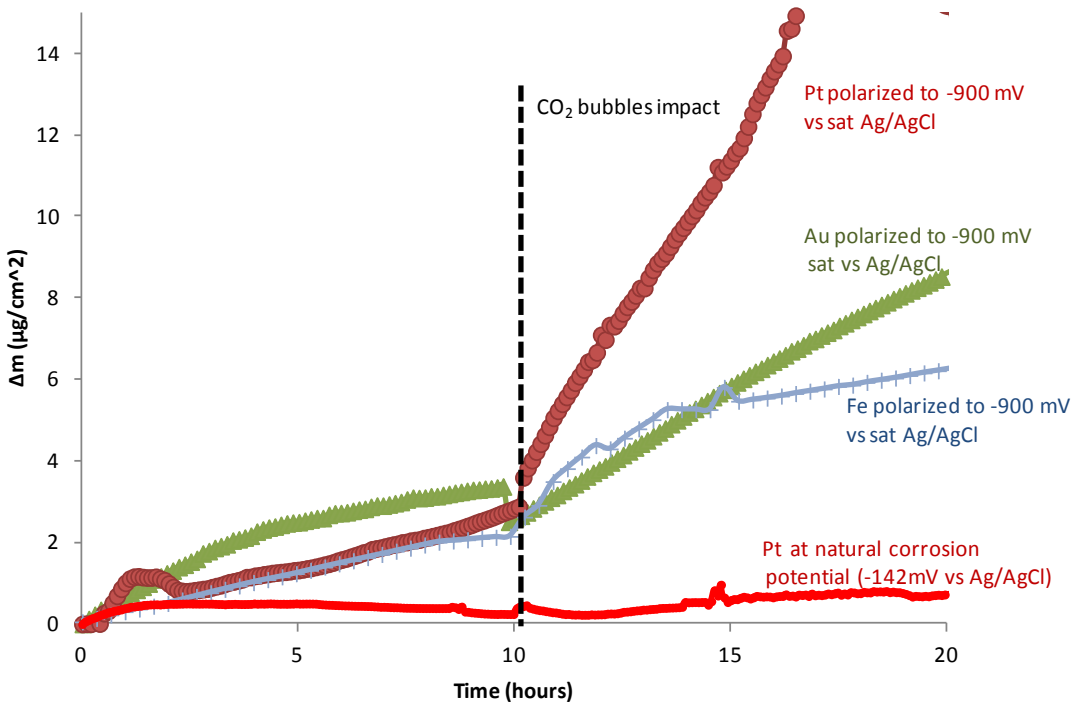

Figure 46. Effect of different substrate on K2 corrosion inhibitor film performance when it is tested against a multiphase flow carrying CO_2 bubbles.

Inhibitor K1 (TOFA/DETA Imidazolinium):

Figure 47 shows the adsorption of inhibitor K1, on three different metal substrates at fixed potential of -900 mV vs Ag/AgCl reference electrode (gold, platinum and iron). Corrosion inhibitor film was exposed to a submerged high velocity water jet containing the inhibitor, following ten hours of adsorption in quiescent conditions. The water jet did not seem to have any adverse effect on the inhibitor film adsorbed on any of the three metal surfaces, and quite the contrary – a significant increase of the adsorbed inhibitor mass was seen.

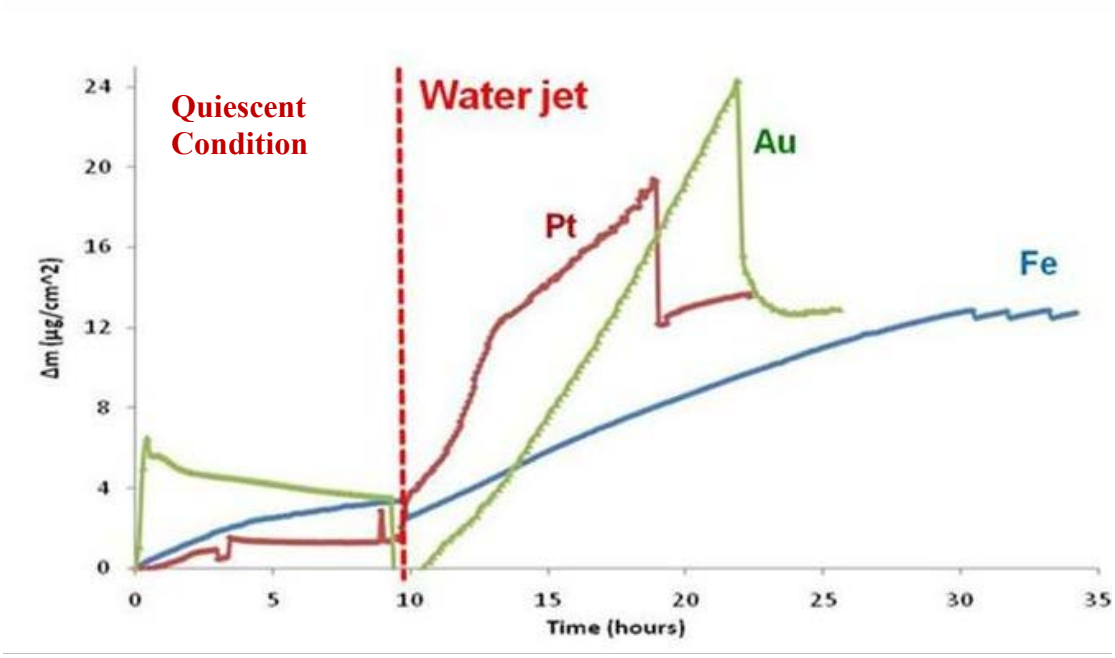

Figure 47. Adsorption and expose to single phase flow (water jet) of inhibitor K1 (TOFA/DETA Imidazolinium) on three different metal substrates (pH 5.0, 25°C, pCO_2=0.98 bar and polarized to -900 mv vs sat Ag/AgCl electrode).

Figure 48 and Figure 49 show the performance of the same inhibitor when exposed to a multiphase flow jet containing CO_2 bubbles and water vapor bubbles, respectively. In neither of these two situations was the inhibitor film disrupted by the multiphase jet on any of the different substrates. Again, the adsorption of corrosion inhibitor on the substrate appeared to increase when jet flow was applied.

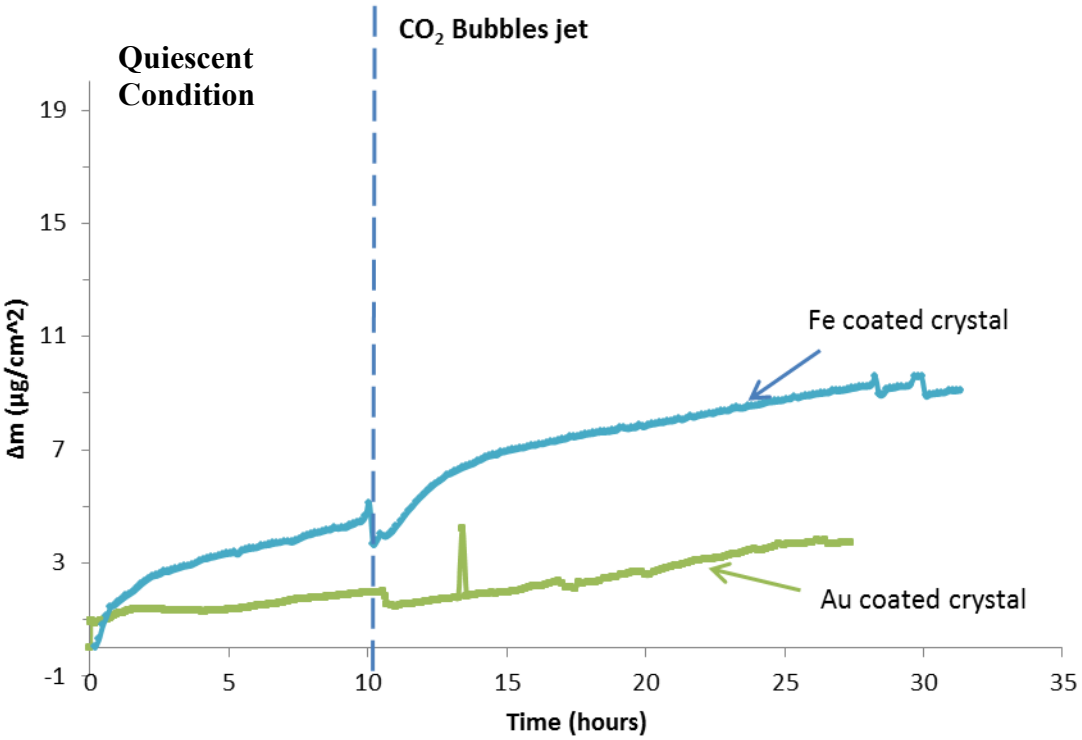

Figure 48. Adsorption and expose to multiphase flow (CO2 bubbles jet) of inhibitor K1 (TOFA/DETA Imidazolinium) on different metal substrates (pH 5.0, 25°C, pCO_2=0.98 bar and polarized to -900 mv vs sat Ag/AgCl electrode).

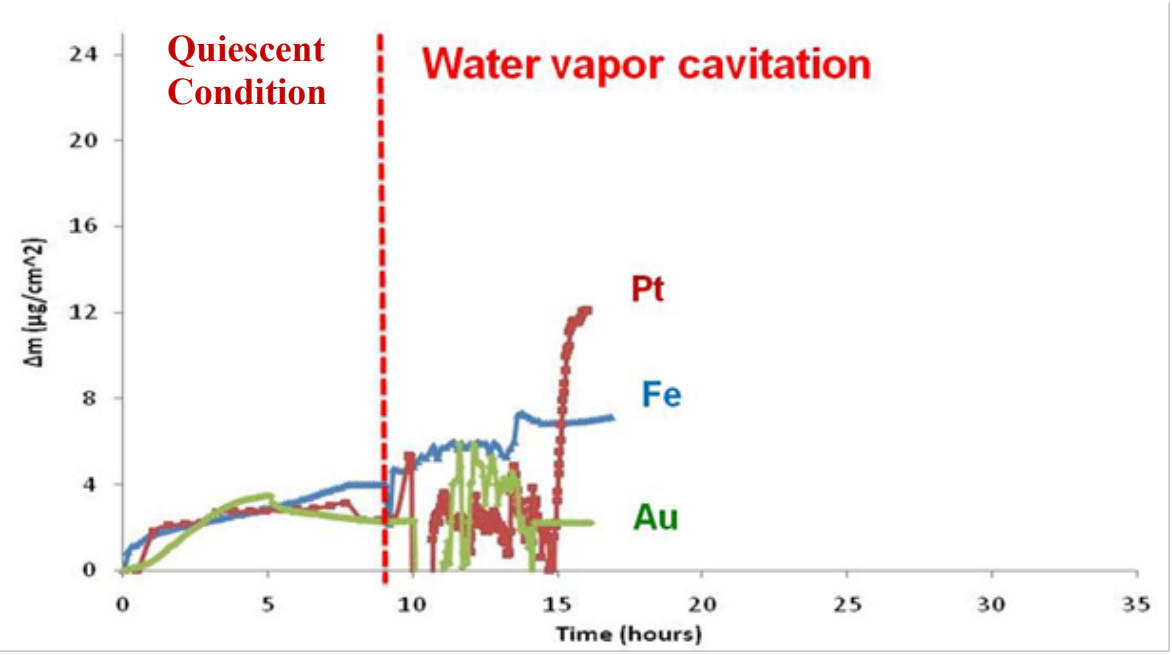

Figure 49. Adsorption and expose to multiphase flow (vapor bubble cavitation) of inhibitor K1 (TOFA/DETA Imidazolinium) on three different metal substrates (pH 5.0, 25°C, pCO_2=0.98 bar and polarized to -900 mv vs sat Ag/AgCl electrode).

Inhibitor K2 (Alkyl benzyl dimethyl ammonium chloride):

Figure 50 shows an inhibitor film developed with an alkyl benzyl dimethyl ammonium chloride, labeled K2, after ten hours of adsorption. When adsorption of corrosion inhibitor reached a quasi-stable value (~3.5 µg/cm^2 for all three metallic surfaces) the film was exposed to a water jet. The result shows that inhibitor film K2 was not affected adversely by the submerged water jet.

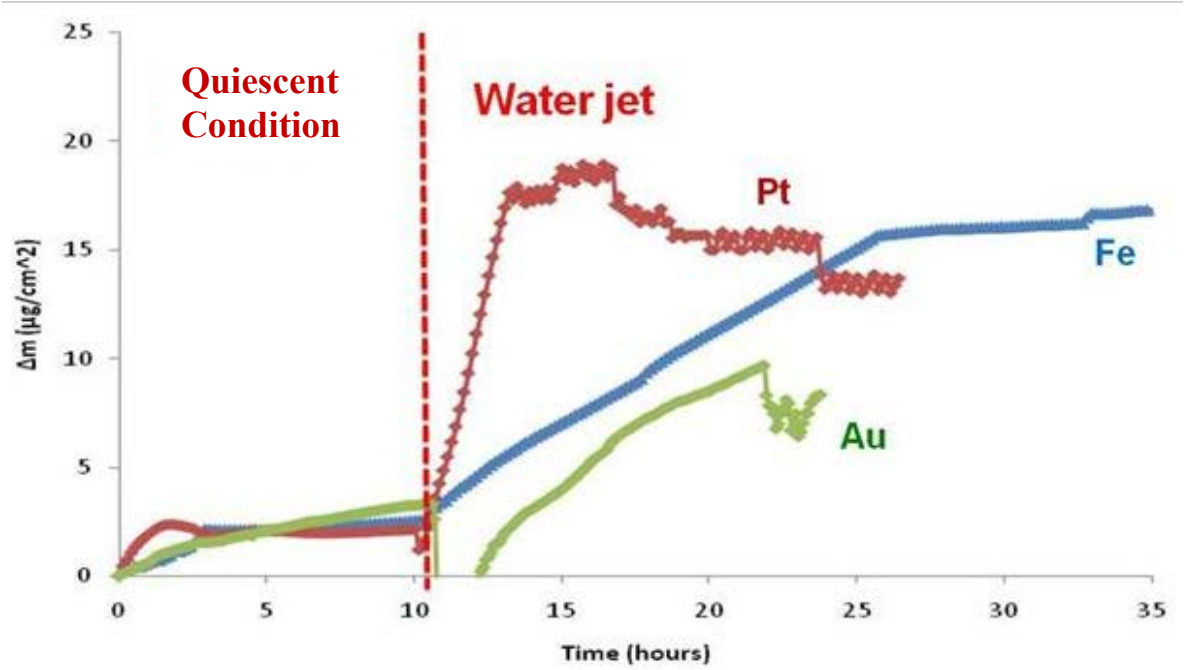

Figure 50. Adsorption and expose to single phase flow (water jet) of inhibitor K2 (alkylbenzyl dimethyl ammonium chloride "quat") on three different metal substrates (pH 5.0, 25°C, pCO_2=0.98 bar and polarized to -900 mv vs sat Ag/AgCl electrode).

The effects of multiphase flow on the performance of inhibitor film K2 are shown in Figure 51 and Figure 52, corresponding to CO_2 bubbles and water vapor bubbles jet impingement. The results showed the same effect as for the single phase water jet. No negative effect of wall shear stress on inhibitor film K2 performance was observed. The opposite happened – the amount of adsorbed inhibitor adsorbed increased.

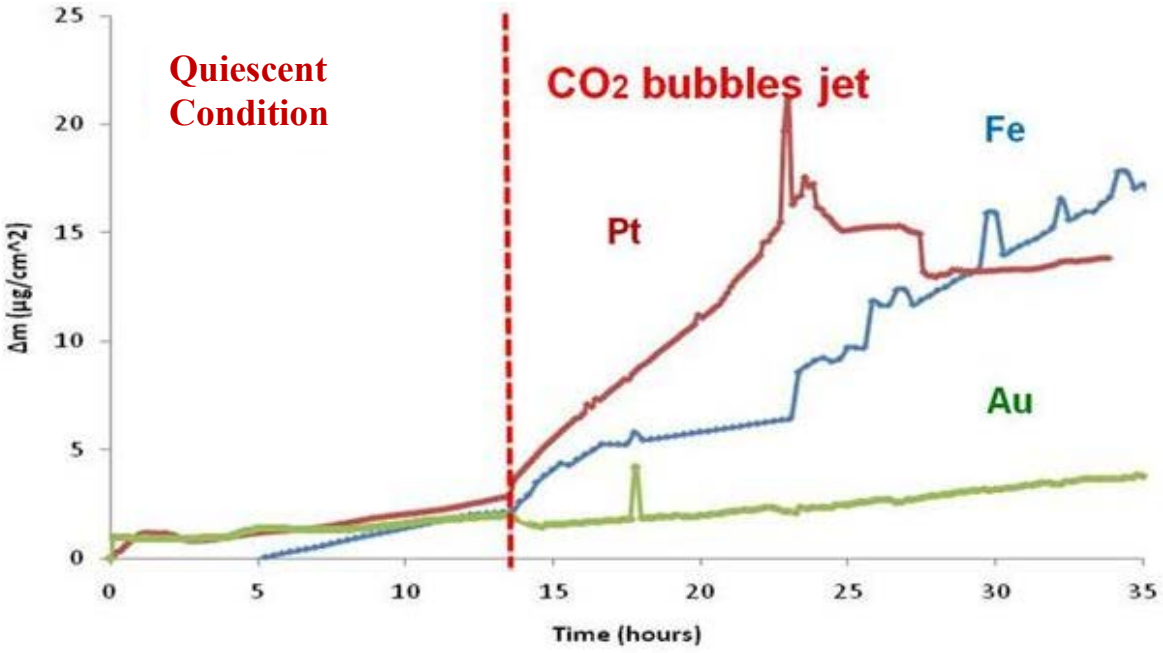

Figure 51. Adsorption and expose to single multiphase flow (CO_2 bubbles jet) of inhibitor K2 (alkylbenzyldimethylammonium chloride "quat") on three different metal substrates (pH 5.0, 25°C, pCO_2=0.98 bar and polarized to -900 mv vs sat Ag/AgCl electrode).

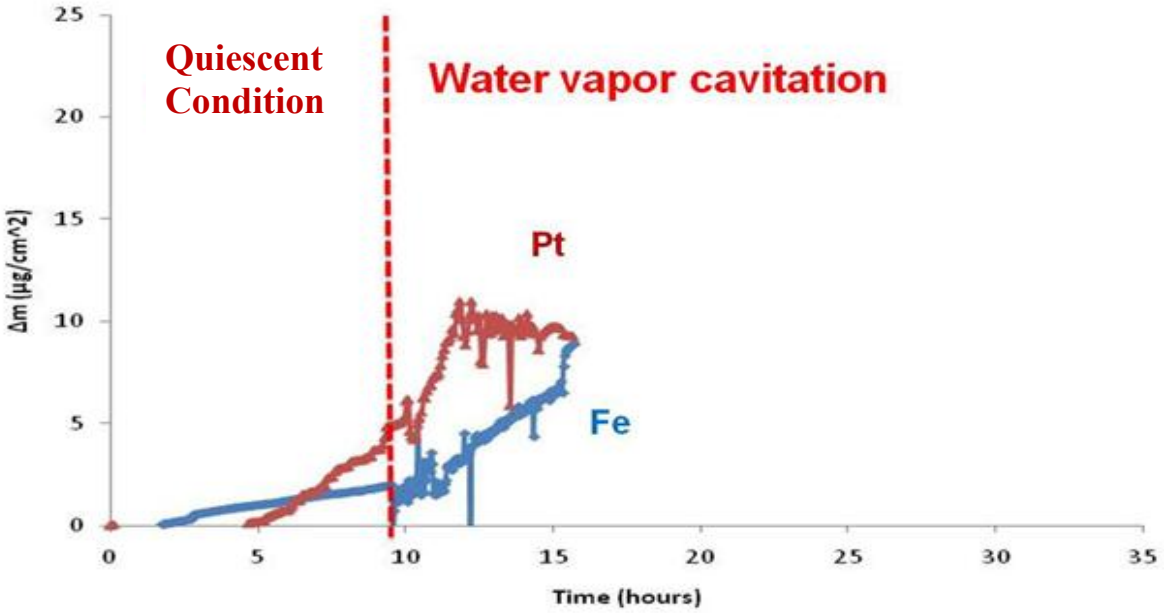

Figure 52. Adsorption of inhibitor K2 (alkylbenzyldimethylammonium chloride "quat") before and after exposure to a multiphase flow (water vapor cavitation) on three different metal substrates (pH 5.0, 25°C, pCO_2=0.98 bar and polarized to -900 mv vs sat Ag/AgCl electrode).

Inhibitor K3 (sodium thiosulfate):

Inhibitor K3, sodium thiosulfate, was allowed to adsorb onto the iron substrate for ten hours. Inhibitor K3 was then exposed to a single-phase and a multiphase submerged jet flow, just like in the cases described above. The results are in Figure 53 for a submerged single-phase water jet, Figure 54 for a jet carrying CO_2 bubbles, and Figure 55 for a jet carrying water vapor bubbles. In all cases the inhibitor film was not disrupted; instead, adsorption of corrosion inhibitor onto iron substrate improved each time the jet flow was applied.

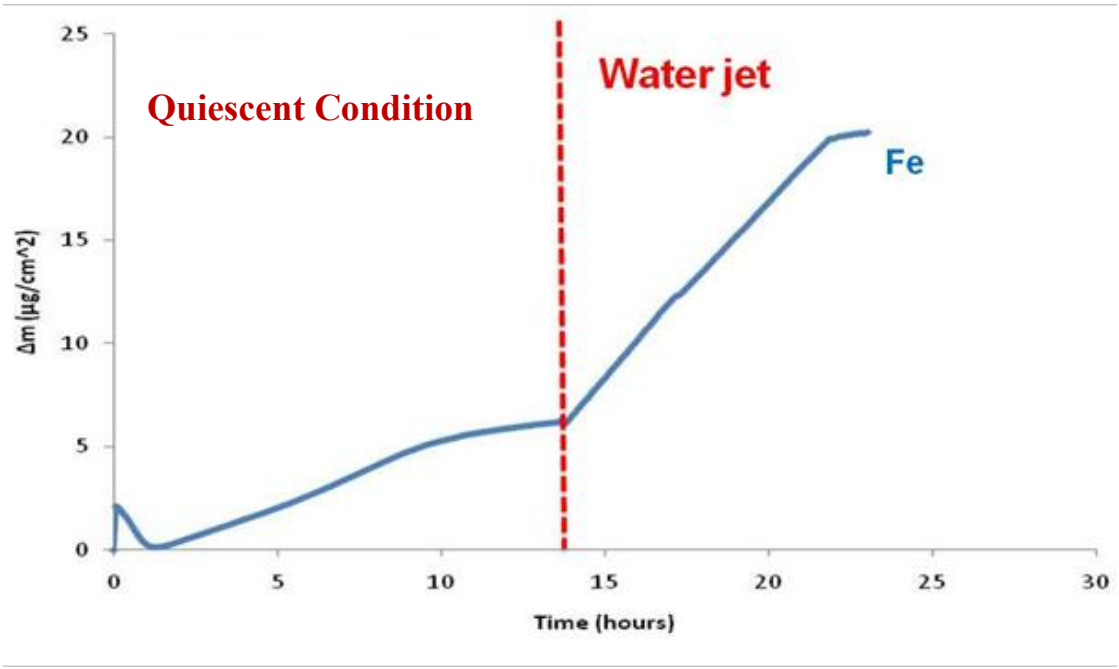

Figure 53. Mass gain and expose to single phase flow (water jet) of inhibitor K3 (sodium thiosulfate) on iron coated quartz crystal substrate (pH 5.0, 25°C, pCO_2=0.98 bar and polarized to -900 mv vs sat Ag/AgCl electrode).

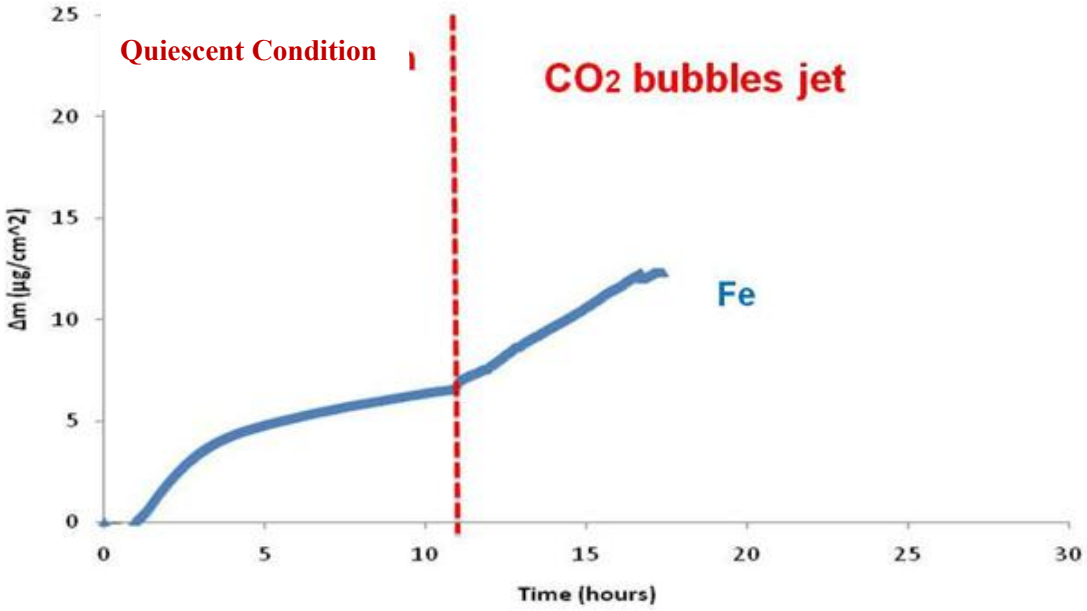

Figure 54. Mass gain and expose to multiphase flow (CO_2 bubbles jet) of inhibitor K3 (sodium thiosulfate) on iron coated crystal substrate (pH 5.0, 25°C, pCO_2=0.98 bar and polarized to -900 mv vs sat Ag/AgCl electrode).

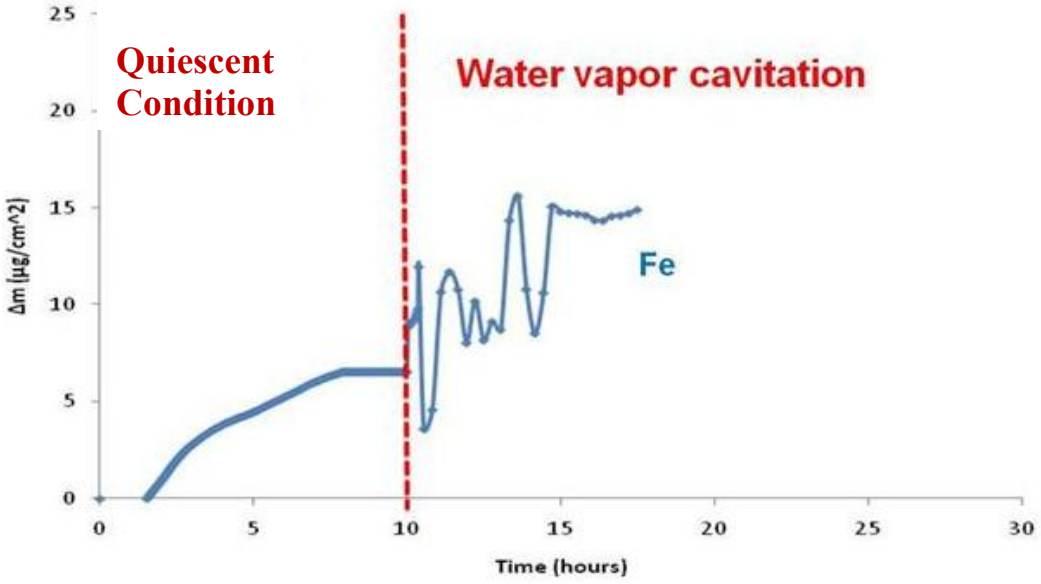

Figure 55. Mass gain and expose to multiphase flow (water vapor cavitation) of inhibitor K3 (sodium thiosulfate) on iron coated quartz crystal substrate (pH 5.0, 25°C, pCO_2=0.98 bar and polarized to -900 mv vs sat Ag/AgCl electrode).

Inhibitor K3 did not adsorb on gold and platinum substrates as far as EQCM measurements could indicate.

Inhibitor K4 (TOFA/DETA Imidazolinium + sodium thiosulfate):

Inhibitor K4, which is a mixture of the surface active components in inhibitor K1 and K3, was impinged by water jet after ten hours of adsorption onto an iron crystal, see Figure 56. When the K4 inhibitor film was exposed by the single phase flow no negative effect was recorded. The adsorbed mass increases during the entire application of the jet. The same result was observed when the system was under multiphase flow with CO_2 bubbles and water vapor bubbles, see Figure 57 and Figure 58 respectively. The behavior

of K1 inhibitor was overall very similar to that of K4 inhibitor reinforcing the conclusion that there was no negative effect of submerged jet flow.

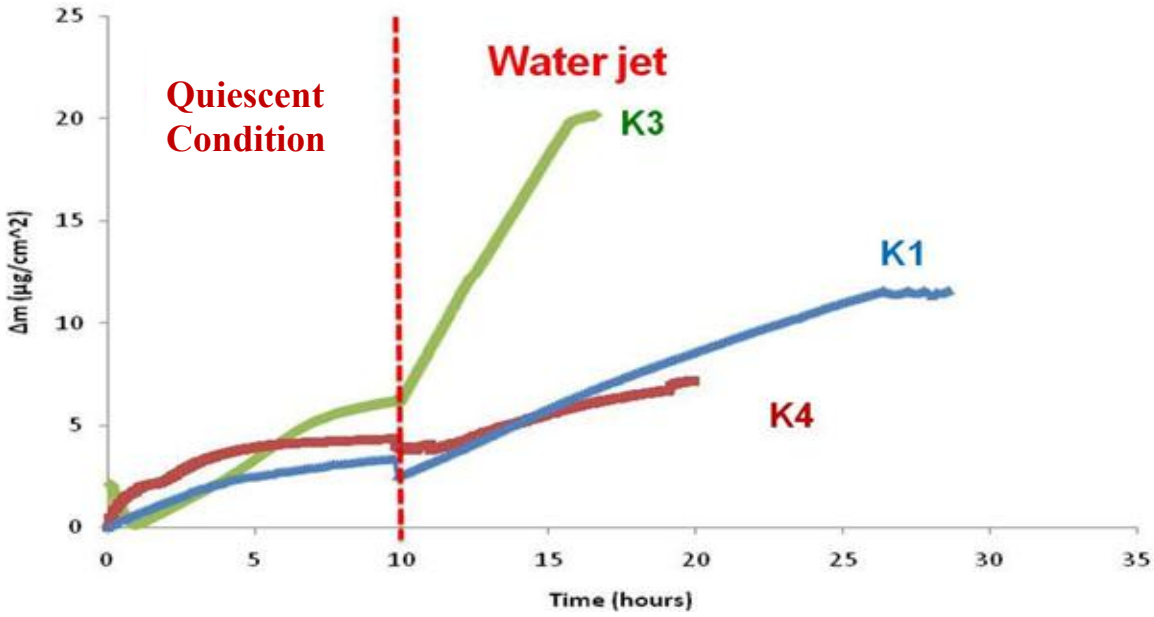

Figure 56. Adsorption and expose single phase flow (water jet) of inhibitor K4 (blend of TOFA/DETA Imidazolinium + sodium thiosulfate) on iron coated quartz crystal substrate (pH 5.0, 25°C, pCO_2=0.98 bar and polarized to -900 mv vs sat Ag/AgCl electrode).

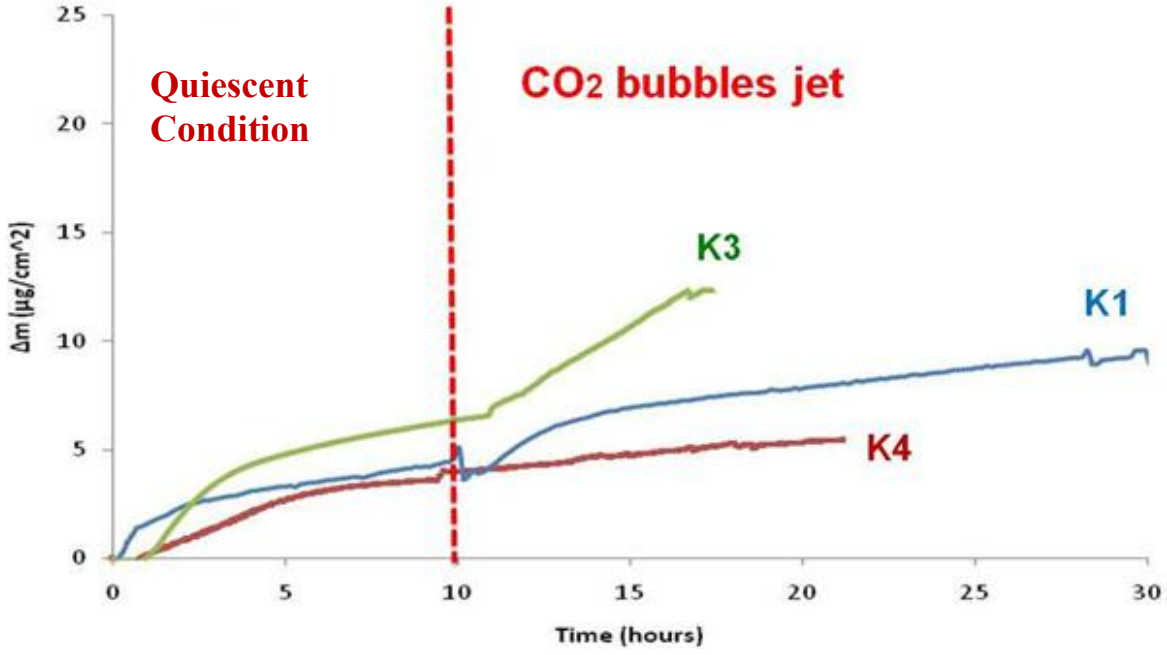

Figure 57. Adsorption and expose to multiphase flow (CO_2 bubbles jet) of inhibitor K4 (blend of TOFA/DETA Imidazolinium + sodium thiosulfate) on iron coated quartz crystal substrate (pH 5.0, 25°C, pCO_2=0.98 bar and polarized to -900 mv vs sat Ag/AgCl electrode).

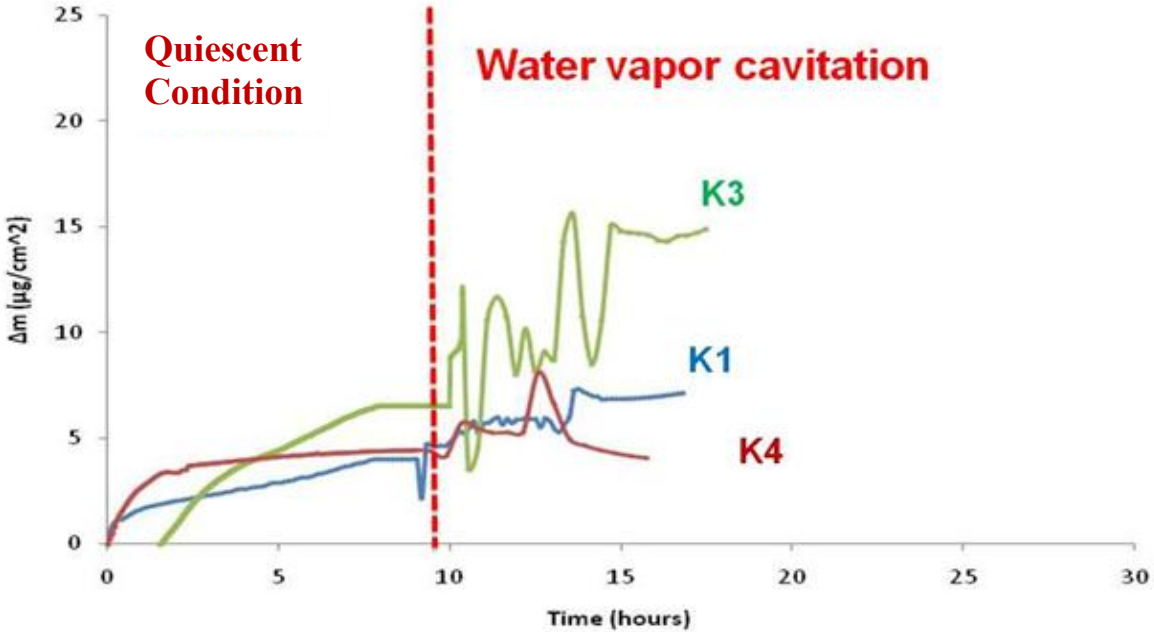

Figure 58. Adsorption and expose to single phase flow (water vapor cavitation) of inhibitor K4 (blend of TOFA/DETA Imidazolinium + sodium thiosulfate) on iron coated quartz crystal substrate (pH 5.0, 25°C, pCO_2=0.98 bar and polarized to -900 mv vs sat Ag/AgCl electrode).

Inhibitor K5 (alkylbenzyl dimethyl ammonium chloride + sodium thiosulfate):

The jet impingement effects on corrosion inhibitor film using K5 are shown in Figure 59, Figure 60 and Figure 61 for the three different conditions evaluated. After 10 hours of inhibitor adsorption, a jet was applied on the inhibitor film. Figure 59 shows the effect of the submerged water jet on the inhibitor film. No negative effect on the film was registered. Again, an increase in mass adsorbed was observed at the time of jet impingement. Multiphase flow effects made with CO_2 bubbles, Figure 60, and water vapor bubbles, Figure 61, show similar results as for single phase flow. Inhibitor K5 behaved overall very similar to inhibitor K2.

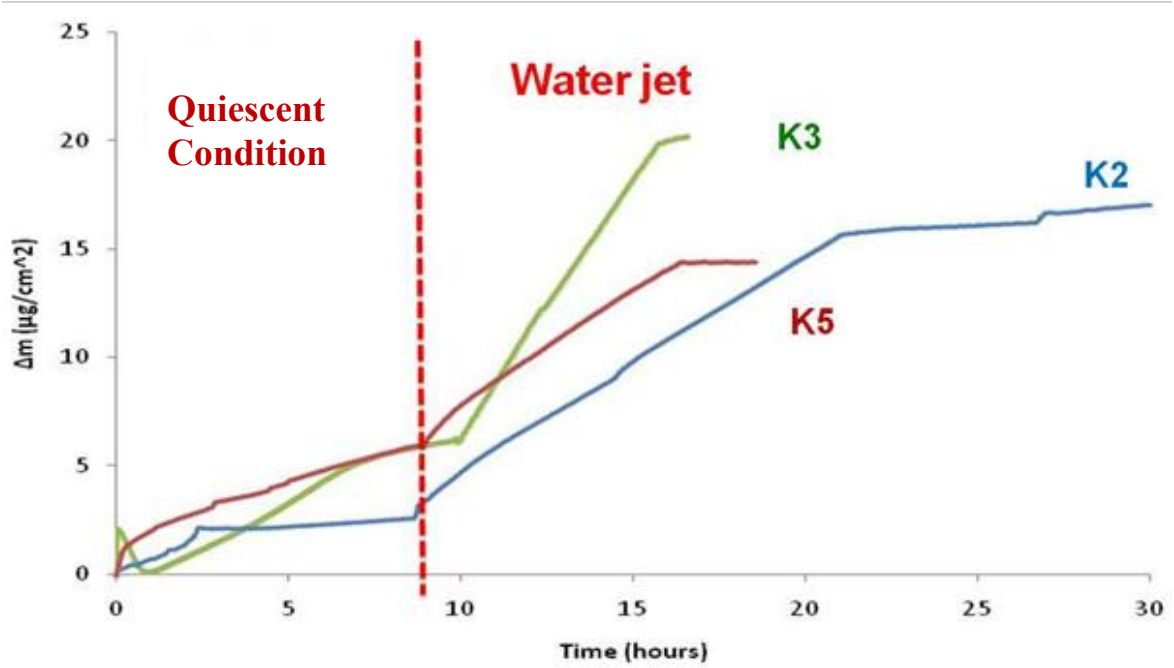

Figure 59. Adsorption and expose to single phase flow (water jet) of inhibitor K5 (blend of alkylbenzyl dimethyl ammonium chloride “quat” + sodium thiosulfate) on iron coated quartz crystal substrate (pH 5.0, 25°C, pCO_2=0.98 bar and polarized to -900 mv vs sat Ag/AgCl electrode).

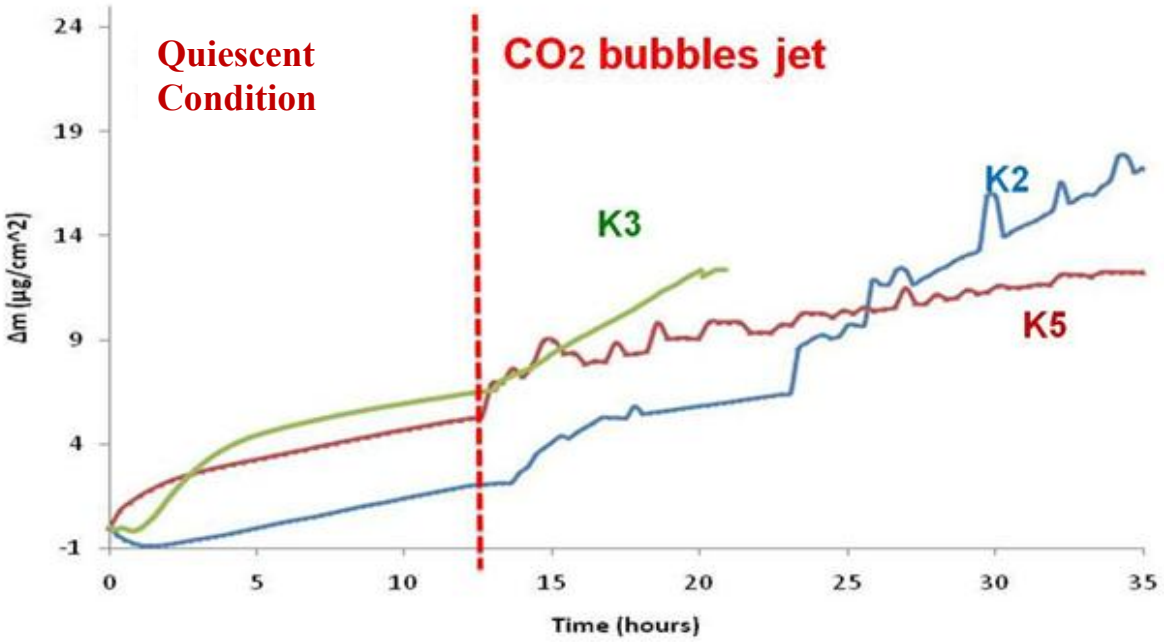

Figure 60. Adsorption and expose to multiphase flow (CO_2 bubbles jet) of inhibitor K5 (blend of alkylbenzyl dimethyl ammonium chloride “quat” + sodium thiosulfate) on iron coated quartz crystal substrate (pH 5.0, 25°C, pCO_2=0.98 bar and polarized to -900 mv vs sat Ag/AgCl electrode).

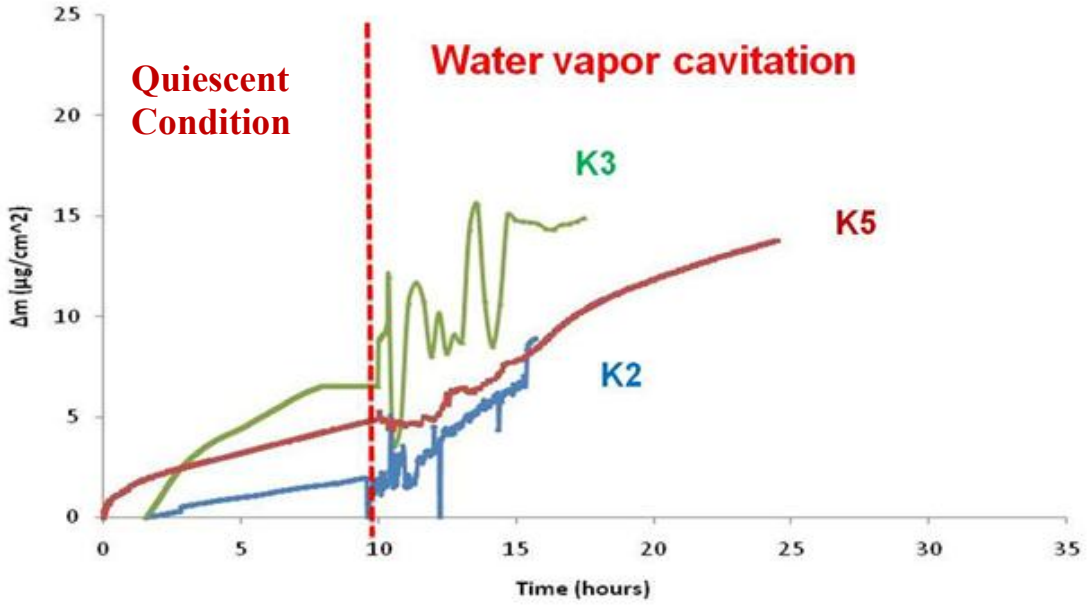

Figure 61. Adsorption and expose to multiphase flow (water vapor cavitation) of inhibitor K5 (blend of alkylbenzyl dimethyl ammonium chloride "quat" + sodium thiosulfate) on iron coated quartz crystal substrate (pH 5.0, 25°C, pCO_2=0.98 bar and polarized to -900 mv vs sat Ag/AgCl electrode).

4.4 Discussion

The effect of wall shear stress on corrosion inhibitor film integrity was evaluated using five corrosion inhibitor formulations, three different hydrodynamic setups with a submerged water jet under single phase flow, a multiphase flow carrying CO_2 bubbles and multiphase flow carrying water vapor bubbles, on three different substrates (iron, gold and platinum). The results show that there was uniformly no negative effect of wall shear stress, even for the most aggressive case of cavitating vapor bubbles.[1] Instead of

[1] In recent research results using extreme cavitation caused by sudden pressure drop following an obstacle in flat channel flow, performed by Li [100] (2014), it was demonstrated that corrosion inhibitor film

causing inhibitor film removal, the jet flow seemed to increase inhibitor film adsorption, irrespective of the inhibitor type or the substrate.

Some of the prior research has indicated that wall shear stress should not play any role on corrosion inhibitor film removal, due to a wide disparity in length scales[60,79]. While wall shear stress length scale can be estimated using the viscous sub-layer thickness, which is of the order of micrometers, corrosion inhibitor films measure in nanometers [79,125,130]. Consequently, the author claims that it is difficult to envision an effective mechanical interaction between the single-phase flow structures and the adsorbed inhibitor film.

Experiments performed in this work show that corrosion inhibitor adsorption actually increases due to the application of the single phase water jet. Two arguments could be hypothesized for this scenario:

1.- It has been previously argued that the increased turbulence due to water jet flow provides better inhibitor transport to the surface [141,142] although it is not clear that this is the right argument for the present case.

2. – Alternatively it can be argued that higher shear and increased turbulence leads to the disruption of micelles, leading to a higher free inhibitor concentration close

---

failure could be achieved in these conditions. However, in the same study, this cavitation damage was overpowered when the corrosion inhibitor concentration was significantly increased. Either way, this study confirmed that extremely high surface forces are required to cause inhibitor failure at the steel surface.

to the steel surface. Thus results in a higher coverage of the steel surface with the inhibitor molecules, improving the inhibitor performance.

Mass gain of the inhibitor was also observed when the system was impinged by a jet carrying CO_2 bubbles regardless the nature of the corrosion inhibitor or the substrate. A possible explanation for this increase in mass is due to the surfactant nature of the molecules. The tendency of the surfactant is to partition the molecule locating the hydrophilic head in the water phase and the tail into the gas phase. This tendency has been reported to be energetically stable [18] and means that CO_2 bubbles could carry additional corrosion inhibitor molecules to the surface. However, further investigation is needed to clarify the investigation. Inhibitor K3 is not a surfactant, and therefore the explanation provided above does not hold.

4.5 Electrochemical Corrosion Measurements

These experiments performed using the EQCM, do not tell us whether the incremental changes in adsorbed mass translate into improvement in corrosion inhibitor efficiency. For this reason, a parallel set of experiments with evaluation of inhibited corrosion rates were done and are compared with those where mass adsorbed was measured in an EQCM. Comparison was made using a CO_2 bubble jet which bears the closest similarities with slug flow.

Figure 62 compares corrosion rate and mass gain of corrosion inhibitor K1 after ten hours of adsorption on an iron coated crystal. The corrosion rate reaches a value of 0.4 mm/year, giving an efficiency of 66%. An increase in mass of inhibitor adsorbed clearly coincides with an improvement in inhibitor protectiveness against corrosion. After

the CO_2 bubble jet was applied, the corrosion rate diminishes to a low value of 0.03 mm/year, and this is matched by the increase of adsorbed mass of the inhibitor. Clearly, the improvement of corrosion inhibitor efficiency corresponds to the increase of corrosion inhibitor adsorption measured by the EQCM. This further reinforces the finding that change in hydrodynamic conditions introduced by the impinging jet is not a factor in corrosion inhibitor film removal.

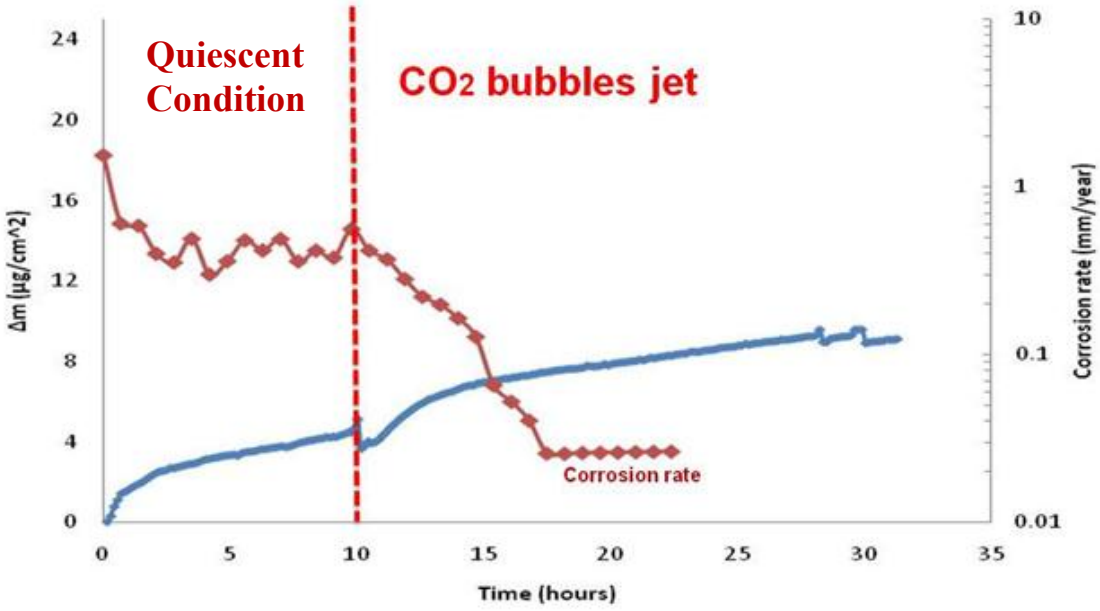

Figure 62. Comparison between corrosion rate and mass gain of corrosion inhibitor K1 when impinged by multiphase flow of CO_2 bubbles (pH 5.0, 25°C and pCO_2=0.98 bar).

Figure 63 shows the effect of wall shear stress on corrosion rate measurements using corrosion inhibitor K2. Corrosion inhibitor efficiency reaches a value of 75% in quiescent conditions. Once the CO_2 bubble jet impinges the corrosion inhibitor film the corrosion rate is reduced to a value of ~0.09 mm/year. The corresponding situation is

observed in EQCM experiments. After application of the CO_2 bubbles jet, corrosion inhibitor adsorption onto the metallic surface is enhanced. The two results obtained with different techniques give coherent results. No negative effect of increased wall shear stress due to jet flow on corrosion inhibitor film removal was found.

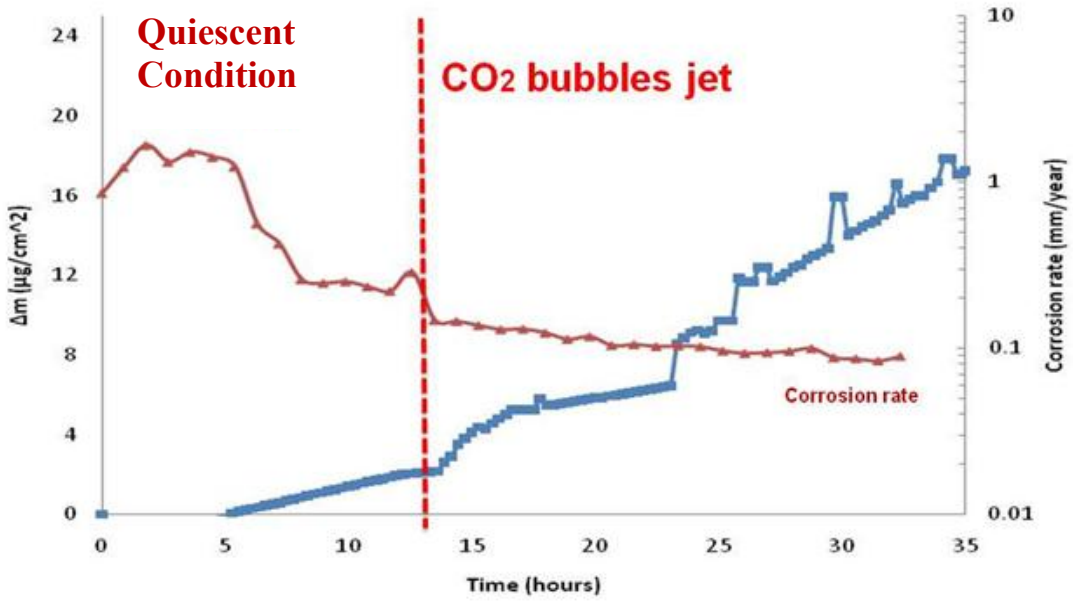

Figure 63. Comparison between corrosion rate and mass gain of corrosion inhibitor K2 when impinged by multiphase flow of CO_2 bubbles (pH 5.0, 25°C and pCO_2=0.98 bar).

Figure 64 shows the corrosion rate for corrosion inhibitor K3. The corrosion inhibitor K3 reached an efficiency of 97% when the system was is in quiescent conditions. After the application of the jet with CO_2 bubbles the corrosion rate is reduced to a value of ~0.007mm/year, conferring an efficiency of 99%. The increase in corrosion inhibitor efficiency due to jet impingement is in accordance with the EQCM results. In both experiments the inhibition by corrosion inhibitor K3 was improved by flow.

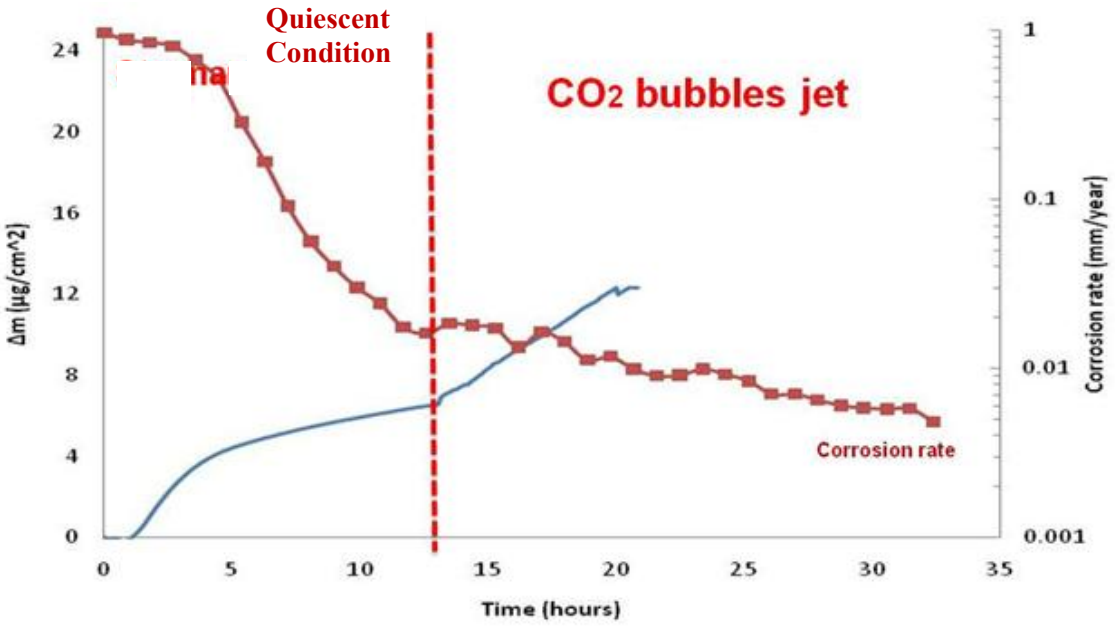

Figure 64. Comparison between corrosion rate and mass gain of corrosion inhibitor K3 when impinged by multiphase flow of CO_2 bubbles (pH 5.0, 25°C and pCO_2=0.98 bar).

Corrosion rate of corrosion inhibitor K4 is shown in Figure 65. Before the application of the CO_2 bubble jet, the corrosion rate reaches a value of ~0.07 mm/year giving an efficiency of 95%. After ten hours of inhibitor adsorption the CO_2 bubble jet impinges the inhibitor film. The results show that changes in hydrodynamic conditions do not have any effect on corrosion inhibitor film performance.

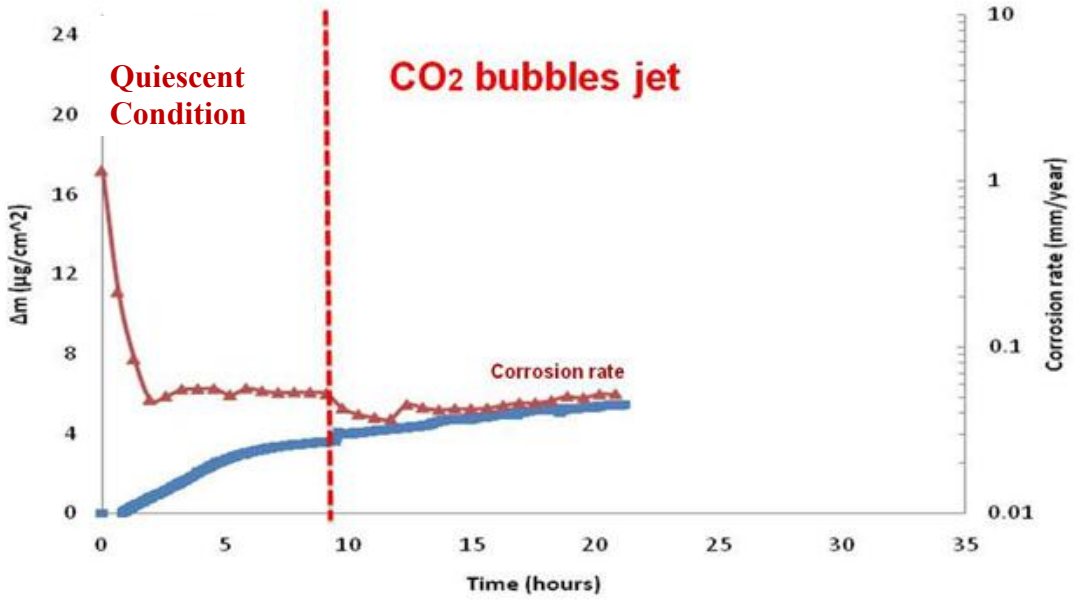

Figure 65. Comparison between corrosion rate and mass gain of corrosion inhibitor K4 when impinged by multiphase flow of CO_2 bubbles (pH 5.0, 25°C and pCO_2=0.98 bar).

Wall shear stress effects on corrosion inhibitor K5 defined by measuring the corrosion rate is shown in Figure 66. The results prove that wall shear stress does not have any negative effect on corrosion inhibitor film performance. Again, the jet improves the protection conferred by corrosion inhibitor K5 against corrosion.

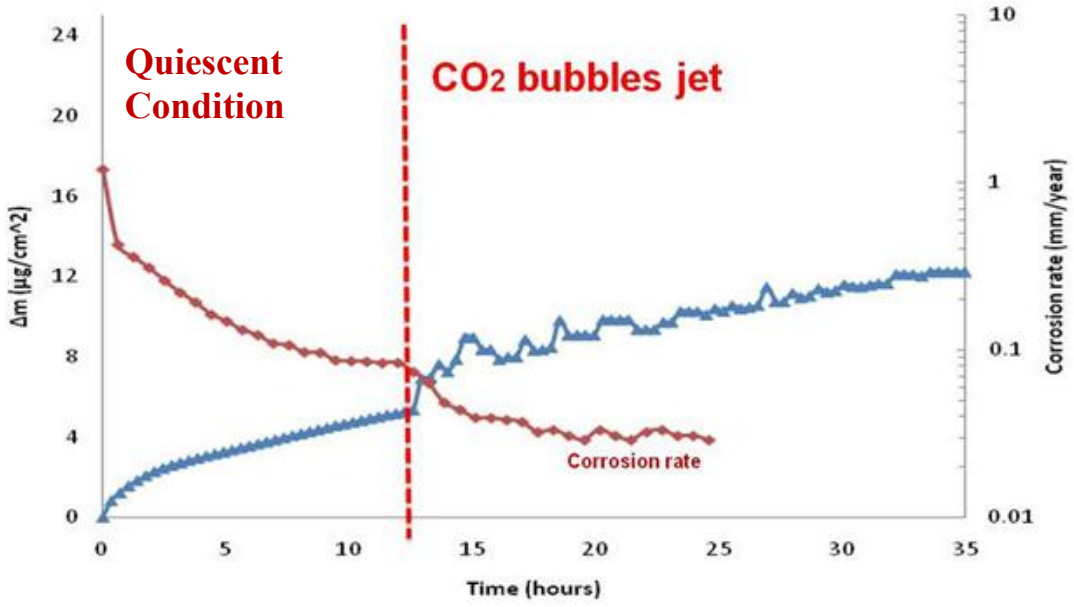

Figure 66. Comparison between corrosion rate and mass gain of corrosion inhibitor K5 when impinged by multiphase flow of CO_2 bubbles (pH 5.0, 25°C and pCO_2=0.98 bar).

4.6 Summary

The multitude of experimental results shown in this section of the work, obtained with the two different techniques: corrosion rate and mass adsorption, lead to the same conclusions. Increasing wall shear stress does not have a detrimental effect on corrosion inhibitor performance. The effect of more intense turbulent flow, according to the current results, can even be beneficial for corrosion inhibitor film performance. As previously explained this can be due to higher shear and increased turbulence leading to the disruption of micelles, leading to a higher free inhibitor concentration close to the steel surface. Resulting in a higher coverage of the steel surface with the inhibitor molecules, improving the inhibitor performance.

4.7 Large Scale Experiments

Using two different large scale multiphase flow systems provided an opportunity to test the effect of more realistic turbulent multiphase flow on inhibitor film performance. Slug flow was used as one of the more severe multiphase flow regime due to the high shear stress that is developed at the front of the slug. The two multiphase flow systems could generate either a “moving” slug or a “standing” slug.

4.7.1 Standing Slug

A slug flow is a multiphase flow pattern encountered in oil and wet gas pipelines generated by the accumulation of liquid in the cross-section of the line. When the liquid bridges the entire cross section of the pipe, a slug of liquid is formed and pushed forward by the buildup of gas behind it. The liquid slug moves at the gas velocity on top of a thin liquid film at the bottom, moving much slower. Bonizzi and Issa[95] (2003) reported that there is a homogeneous distribution of dispersed gas bubbles in the horizontal slug flow. For high flow rates the gas bubbles entering the slug are uniformly distributed. For low flow rates the entrainment of gas bubbles in the slug is not as pronounced.

When the slug is formed the slow liquid film below it is accelerated up to the slug velocity creating an intense shear mixing zone. In this region considerable amount of gas entrains into the slug body, which is released as pulses of bubbles in a similar way as it happens in a so called hydraulic jump[95] (schematic shown in Figure 67). These small and dispersed bubbles in the mixing zone travel with high intensity to the bottom of the pipe where they are dispersed.

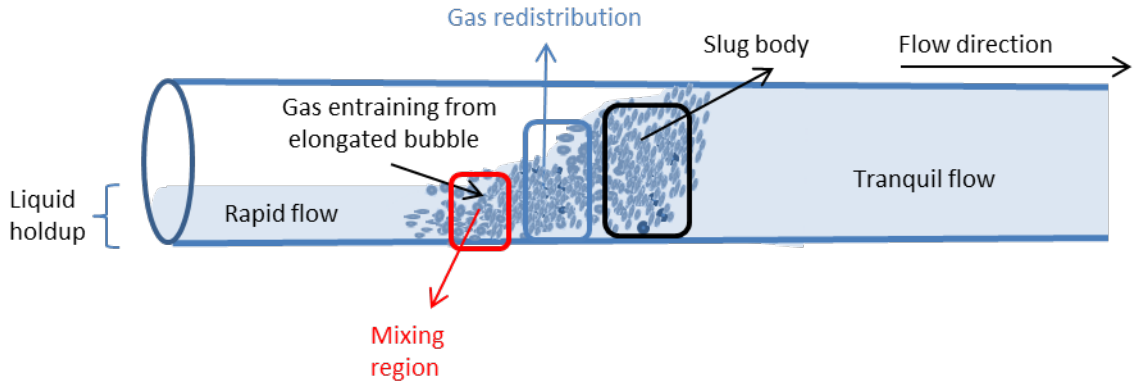

Figure 67 Hydraulic jump schematic[95]

The slug flow characteristics were studied from Fagundes, *et al*. [143], (1999) and by Maley and Jepson[97] (1998) using a hydraulic jump. According to Fagundes, *et al*. [143], (1999) the hydraulic jump occurs along a finite length where wall shear stress is much higher than the shear stress experienced in the fully developed flow. This seems to suggest that the wall shear stress experienced in the hydraulic jump is of the same magnitude to the wall shear stress seen in the moving slug flow. Therefore, a hydraulic jump (also referred to as "standing slug") provides an interesting (worst case) scenario where a high wall shear stress seen at the slug front, can be held in one location for prolonged periods of time.

Different authors have investigated the characteristics of a standing slug. According to Fan. *et al.* [144], the hydraulic jump has three characteristic regions Figure 68.

- The mixing region, which is the zone of high turbulence where small bubbles are formed due to entrance of gas into the liquid film.

- The gas recirculating region, at this region some of the bubbles are transported to the body of the slug, the remaining bubbles are recycled into the gas mass. At this region most of the bubbles are homogeneously distributed through the cross section of the pipe including those impacting the bottom of the pipe wall.
- The slug buddy is the region where the redistribution of gas was completed and remains unaltered trough the slug body.

Wang, *et al.* [145], (2012) reported four different regions for the standing slug: the same three regions described above by Fan plus a fourth region at the end of the slug where the flow becomes stratified.

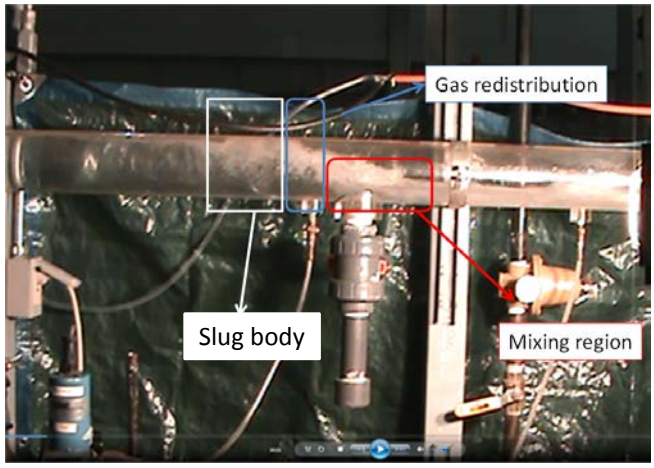

Figure 68 Standing slug visualization.

4.7.1.1 Experimental Procedure

A standing slug setup was used as a severe slug condition to evaluate the effect of wall shear stress on thin protective inhibitor films, as the slug “hovers” at approximately the same location for an extending period of time. In order to measure the effect of

surface forces on inhibitor films, a set of experiments (Table 7) was performed by placing an EQCM to measure the mass of adsorbed inhibitor, at the location on the wall just below the standing slug. With the exception of inhibitor K3, the concentration used was twice the critical micelle concentration (CMC); the exact values are shown in Table 4.

The standing slug flow loop was deoxygenated by the continuous injection of CO_2 in the liquid stream. The pH was adjusted accordingly with the additions of Na_2CO_3. Once the pH was adjusted the liquid flow rate was set to 1 m/s. The loop was operating at atmospheric pressure and 25 °C. Once the operating conditions were set in the flow loop the probe, either EQCM or LPR, was inserted. For the EQCM mass gain measurements, the crystal was polarized to –0.9V (*vs.* saturated Ag/AgCl) in order to minimize corrosion of the thin iron layer. The flow pattern used in the first part of the experiment was single phase liquid flow. In this first time period the corrosion inhibitor was added in the flow loop, to simulate the continuous injection, common practice in the oil and gas industry. After an initial adsorption on the probe surface time of approximately 6 hours, it was deemed that the corrosion inhibitor had achieved its maximum coverage as observed by the small change of mass, using the EQCM. The resulting inhibitor film was then exposed to the standing slug, which was developed by injecting the CO_2 gas right after the flow loop gate as was described above. The standing slug was positioned over the iron coated EQCM surface covered by the corrosion inhibitor for as long as 6 hours. In the second series of similar experiments, electrochemical measurements of the corrosion rate (LPR) were performed using a flush mounted, concentric ring LPR probe following the same procedure, but without polarizing to -0.9 V vs. sat Ag/AgCl electrode.

4.7.1.2 Test Matrix

Table 7. Experimental conditions – using standing slug to evaluate the high wall shear stress effect on corrosion inhibitor film

Test Solution	Water + 1 wt.% NaCl
Temperature	25 °C
Partial pressure	0.98 bar at 25 °C
pH	5.0
Inhibitor type (from table 1 in chapter 3) Inhibitor concentration	2 CMC
Test material	Iron quartz coated crystal Polarized to -0.9V vs sat Ag/AgCl
High stress shear on the EQCM	Standing slug

4.7.1.3 Results and Discussion

Effects of wall shear stress on corrosion inhibitor film performance using an electrochemical quartz crystal microbalance are reported in this section. Figure 69 shows the effect of adsorption of TOFA/DETA imidazolinium, K1, on an iron coated quartz crystal. Corrosion inhibitor film was exposed to the standing slug following six hours of adsorption in single phase liquid flow. The wall shear stresses developed by the standing slug did not seem to have a negative effect on the inhibitor film developed on the iron coated quartz crystal, judging by the mass of inhibitor adsorbed. The graph also shown the corrosion rate measured by LPR in parallel experiments as well as the corrosion rate when the system has no inhibitor (to be used as a baseline). When the standing slug was introduced, the corrosion rate did not seem to be adversely affected remaining steady around 0.5 mm/year. This LPR measurement were consistent with the increase of

inhibitor mass adsorbed recorded by the EQCM. This supports the notion that changes in hydrodynamic conditions (increasing mechanical forces introduced by the standing slug) were not a factor leading to corrosion inhibitor film removal.

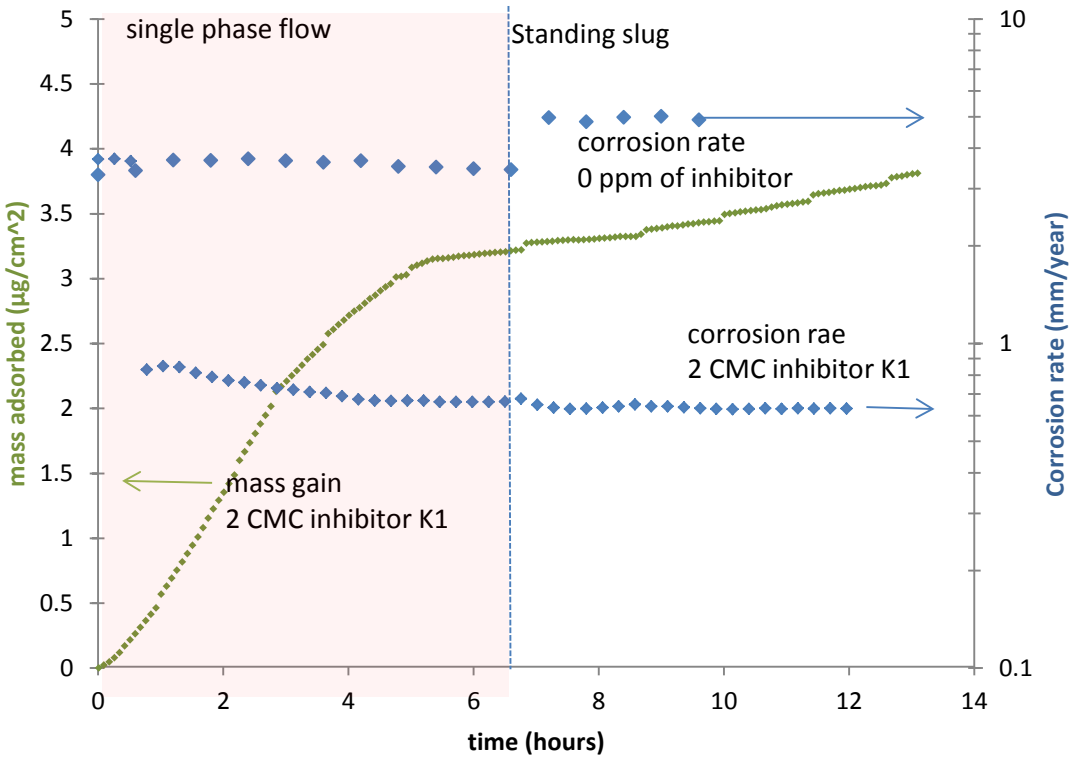

Figure 69. Effect of wall shear stress developed with a standing slug on mass adsorbed and corrosion rate using K1 - TOFA/DETA imidazolinium corrosion inhibitor (pH 5.0, 25°C, liquid velocity 1 m/s and pCO_2=0.98 bar).

Figure 70 shows the effect of wall shear stress developed in a standing slug system on a corrosion inhibitor film developed with inhibitor K2 (alkylbenzyl dimethyl ammonium chloride) after nine hours of adsorption in single phase flow. The result shows no adverse effect of wall shear stress on K2 inhibitor film. Figure 70 also shows

the effect of wall shear stress on LPR corrosion rate for corrosion inhibitor K2. Once the standing slug was introduced, the corrosion rate remains at more or less the same at a value of ~0.9 mm/year. This is consistent to what is observed in EQCM experiment. No negative effect of increased wall shear stress on corrosion inhibitor film removal was found. Actually, after introduction of the standing slug, the K2 corrosion inhibitor adsorption onto the metallic surface is significantly enhanced (similar happened to K1 but to a smaller extent). It is not entirely clear why this happened and because there was no observable effect on the corrosion rate, this effect was not investigated further.

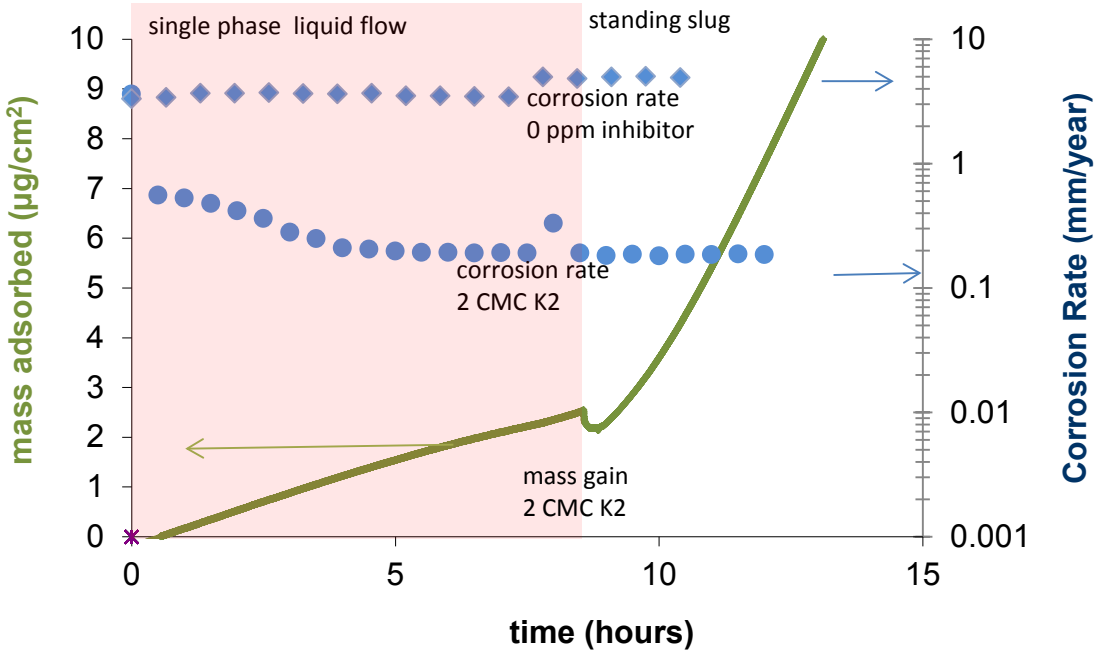

Figure 70. Effect of wall shear stress developed with a standing slug on alkylbenzyl dimethyl ammonium chloride (K2) corrosion inhibitor (pH 5.0, 25°C, liquid velocity 1 m/s and pCO_2=0.98 bar).

Figure 71 shows the effect of inhibitor K3, using a EQCM and an iron coated crystal. Corrosion inhibitor K3 was allowed to react with the iron crystal surface in single phase flow for six hours until a steady state with respect to adsorbed mass was achieved (4.5 $\mu g/cm^2$). The inhibitor film was then challenged by introducing the standing slug flow for six hours. Results showed that the inhibitor film was temporarily removed from the surface, reducing the mass adsorbed from 4.5 $\mu g/cm^2$ to 2.1 $\mu g/cm^2$. However, after the first 15 minutes following the application of the standing slug, the corrosion inhibitor film began to recover. The recovery process took 2 hours to reach the initial value of 4.5 $\mu g/cm^2$. The mass of corrosion inhibitor K3 continued to increase during the entire period of application of multiphase flow. Parallel measurements of corrosion rate are also reported in Figure 71. This experiment shows that corrosion inhibitor K3 reached an efficiency of 95% in quiescent condition. After the application of the standing slug, the corrosion rate remained at approximately the same value of ~0.02 mm/year, conferring an efficiency of 97%. The increase in corrosion inhibitor efficiency due to multiphase flow is in agreement with the EQCM results. In both experiments the inhibition by corrosion inhibitor K3 was not adversely affected by the standing slug.

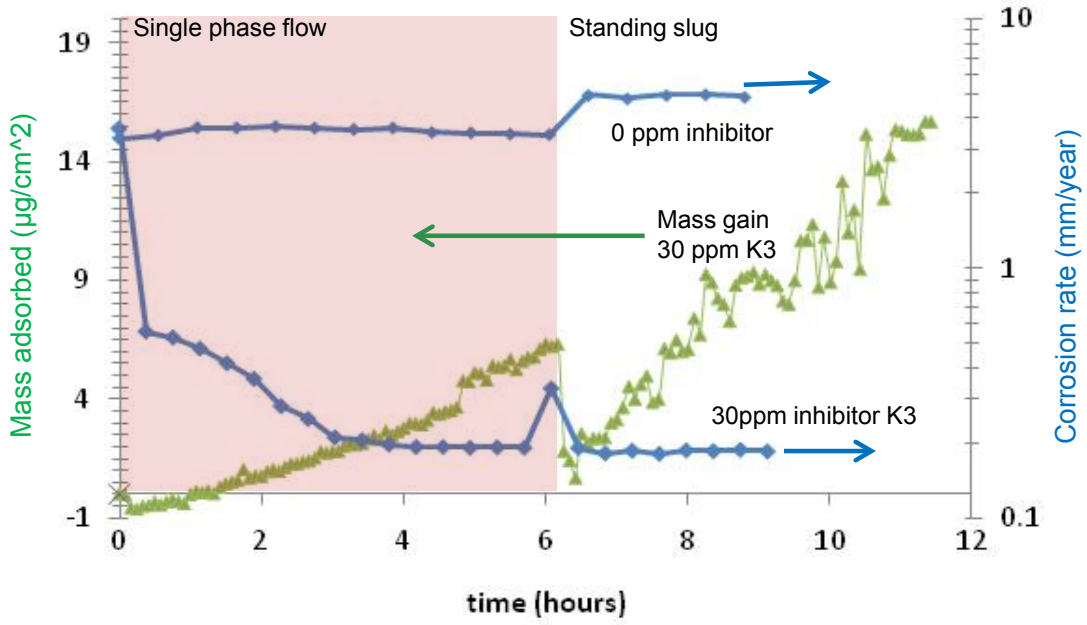

Figure 71. Effect of wall shear stress developed with a standing slug on mass adsorbed and corrosion rate using K3 - sodium thiosulfate corrosion inhibitor (pH 5.0, 25°C, liquid velocity 1 m/s and pCO_2=0.98 bar).

Inhibitor K4, which is a mixture of K1 and K3, was exposed to the standing slug after seven hours of adsorption in single phase flow. Figure 72 shows that there was no negative effect on inhibitor film when it was impacted by the standing slug. The adsorbed mass increased during the standing slug application. In single phase flow the inhibited corrosion rate reached a value of ~0.025 mm/year giving an efficiency of 99%. The change in hydrodynamic conditions introduced by the standing slug did not have any adverse effect on corrosion inhibitor film performance; rather, the corrosion inhibitor efficiency improved once the standing slug was introduced.

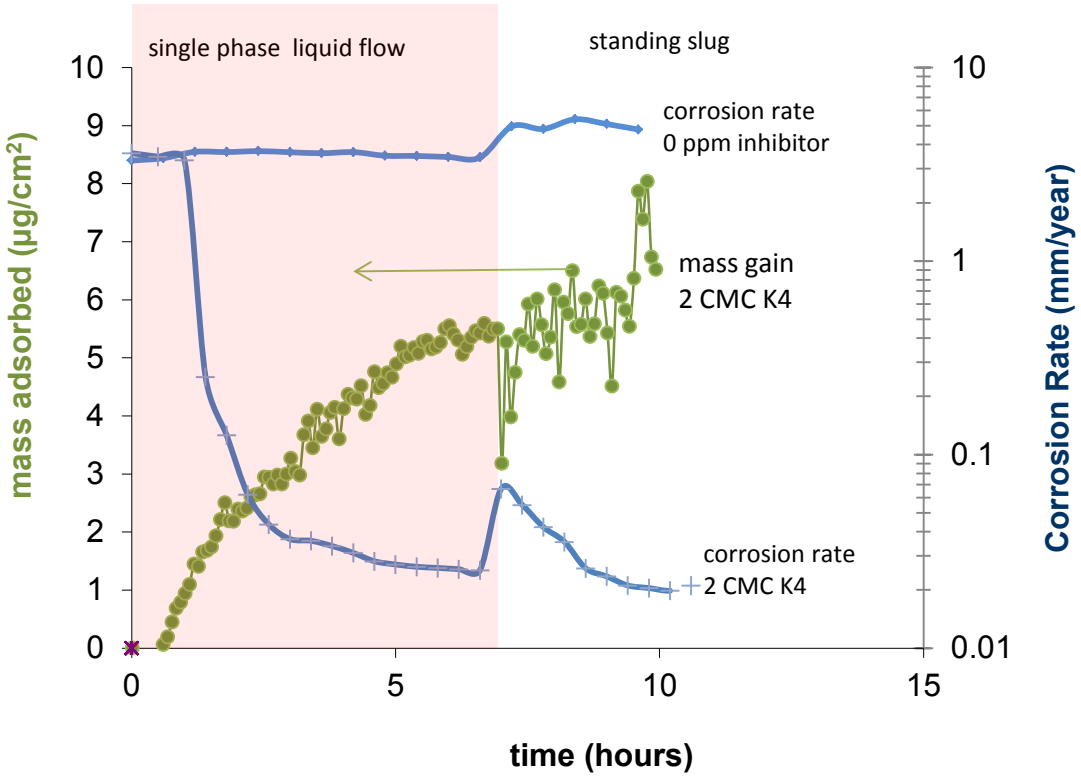

Figure 72. Effect of wall shear stress developed with a standing slug on mass adsorbed and corrosion rate using K4 corrosion inhibitor (pH 5.0, 25°C, liquid velocity 1 m/s and pCO_2=0.98 bar).

Finally, the standing slug effects on corrosion inhibitor film K5 are shown Figure 73. After six hours of adsorption of corrosion inhibitor K5 on an iron coated crystal in single phase flow, a standing slug was introduced. In single phase flow inhibitor K5 reached a maximum adsorption mass of ~5.2 µg/cm^2. When the standing slug was introduced, there was a temporary loss of adsorbed mass from the iron coated quartz crystal (from ~5 µg/cm^2 to 3 µg/cm^2). This is consistent to what was seen with inhibitor K3 which is a component of the K5 inhibitor presented here. After one hour the corrosion inhibitor film mass recovered and then kept on increasing to a value higher than that

reached in the single phase flow conditions. This confirms that there were no permanent adverse effects of wall shear stress on the inhibitor film.

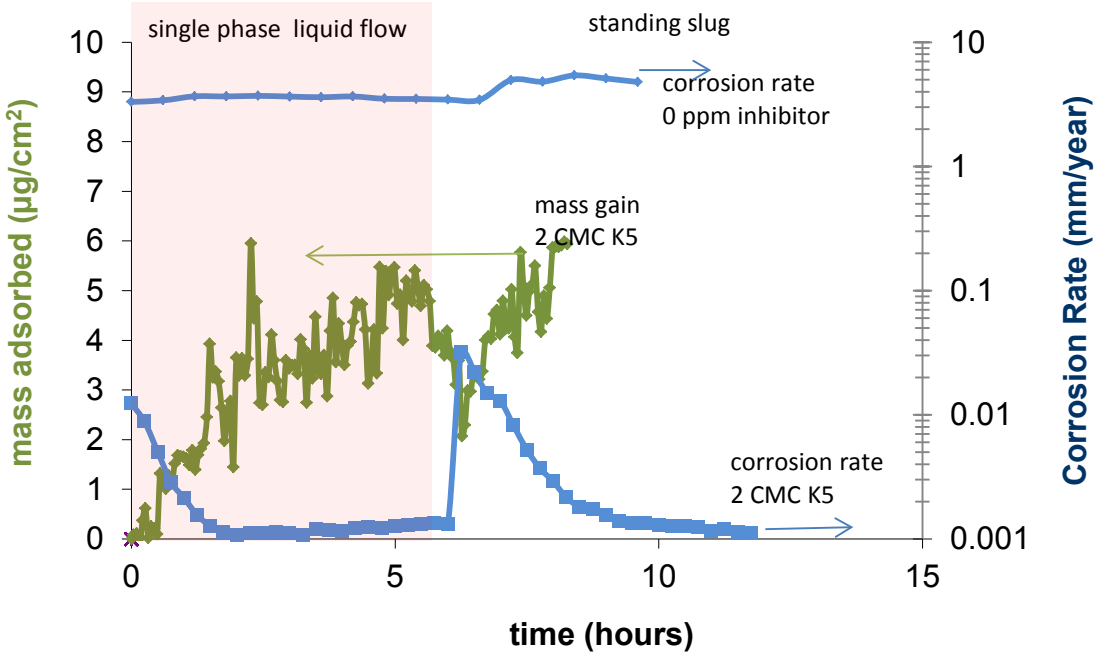

Figure 73. Effect of wall shear stress developed with a standing slug on mass adsorbed and corrosion rate using K5 corrosion inhibitor (pH 5.0, 25°C, liquid velocity 1 m/s and pCO_2=0.98 bar).

4.7.2 Moving Slug

Similar experiments to those described in the section above were conducted in a moving slug condition, more akin to the situation seen in real pipelines. The experiments were conducted in a Hilly-Terrain System which is a 300 gallon, large scale multiphase flow loop (Figure 74). A detailed description of each of the zones encountered in the hilly

terrain flow loop was reported by Laws[146] (2000). A brief summary of the flow zones is presented below and identified in Figure 74 A.

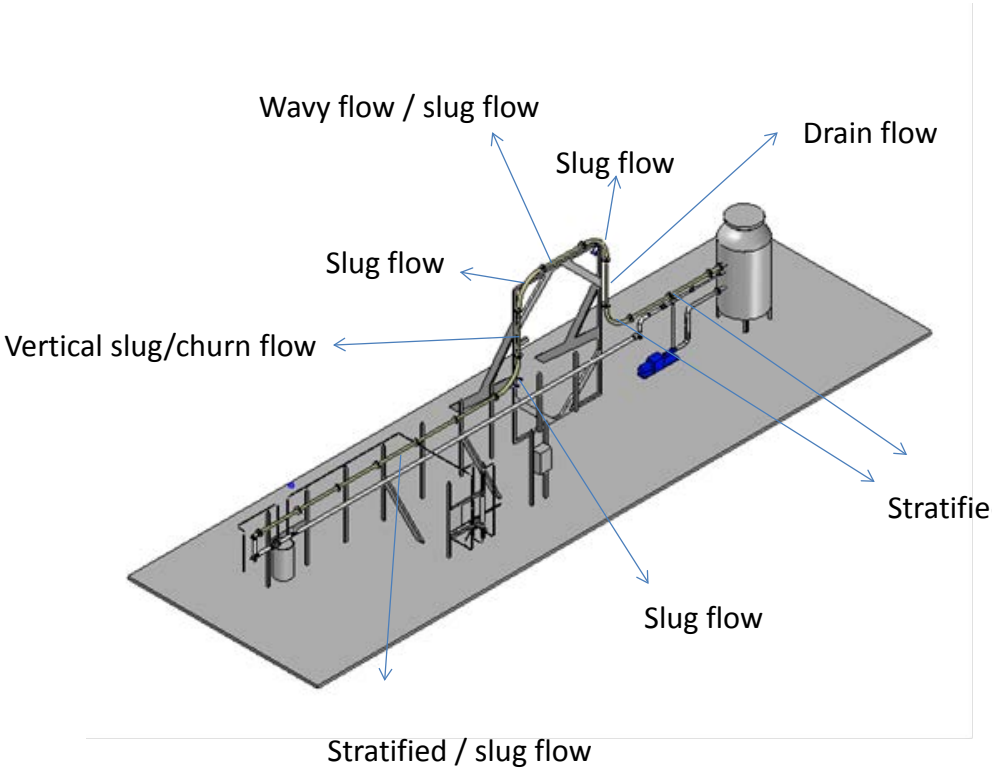

A)

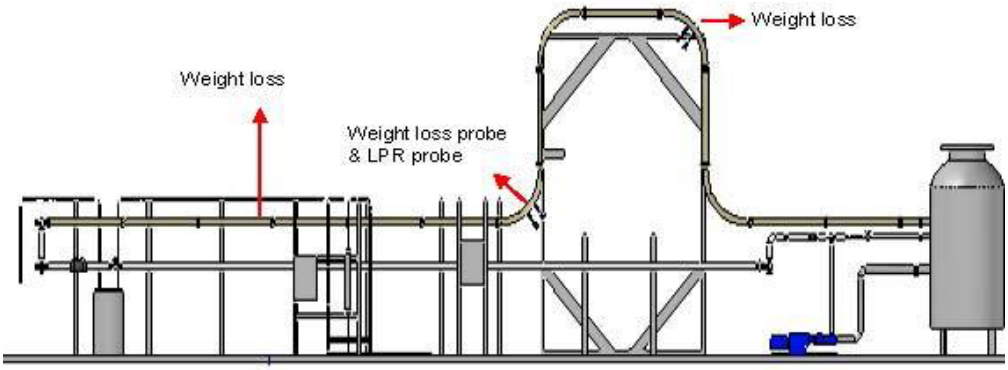

B)

Figure 74. Hilly-Terrain system used to measure the effect of multiphase flow in three different locations. A) flow regimes identified across the hilly terrain flow loop B) locations where the corrosion coupons were installed.

The flow regime in the first zone (horizontal section) is characterized as mostly stratified multiphase flow where slugs can be introduced intermittently at a frequency of 7 slugs/minute when the system operates at a superficial gas velocity (v_{sg}) of 1m/s. The slug frequency increases when the v_{sg} increases, giving a slug frequency of 10 slug/minute for v_{sg}=3m/s, and 15 slugs/minute for v_{sg}=6m/s. There are two test ports in the horizontal section which can be used for corrosion probe insertion.

The second zone in the hilly terrain system is the first elbow (bottom bend) that redirects the multiphase flow from horizontal to vertical direction, via a 32 inch radius bend. This section of the flow loop experiences more or less permanent slugging/churning. This is due to the liquid not being able to move upward against gravity nearly as fast as the gas can. Occasionally the liquid moves downward (against the gas flow) causing intense mixing of the phases. As the gas velocity is increased, the slugging intensity in this region becomes higher. In this section there are also two corrosion probe ports, both on the outer radius of the bend; one was used for electrochemical measurements (LPR) and the other for weight loss (WL).

The third zone is the first vertical riser; this zone is of high turbulence where vertical slug flow and churn hull are typical. The transition from vertical slug to churn flow is function of liquid and gas superficial velocity.

The fourth zone is the bend transition from vertical to horizontal pipe. In the apex of the first up bend there is a high turbulence region product of the hit of the vertical slug going uphill with the liquid film traveling downhill.

The fifth zone is the horizontal bridge in the hilly at this zone the slug–churn flow transit to a wavy flow with intermittent slugs in the horizontal crossing of the pipe.

The sixth zone, in which the hilly terrain system has test ports, is on the inner radius of the second top bend after the horizontal crossing. The second top bend redirects the flow from horizontal to downward vertical via a 32 inch radius bend and has the least turbulent flow in the system. The slugs formed prior to this bend dissipate and drain downwards as they pass through this bend.

The seventh zone is the down vertical pipe. At this zone the dissipated slug is transformed to a drain flow at the down bend of the hilly terrain.

The eighth zone is the last bend, which transit the drain flow from the down vertical pipe to the last horizontal zone, where stratified flow is the typical flow regime. Same stratified flow is encountered in the ninth zone of the flow, the last horizontal zone.

4.7.2.1 Experimental Procedure

All experiments were conducted at pH 5.0 and 25ºC and the inhibitor concentrations tested were 20 and 50ppm. The effect of the moving slug was evaluated using a superficial liquid velocity of 1 m/s and different superficial gas velocities of 1, 3, 6 and 10 m/s.

In addition to the flow loop testing, a glass cell with a standard RCE was connected to the flow loop using the same test liquid so that the inhibitor efficiency could be compared directly between the two experimental setups to ensure a connection with previously done experiments (Figure 10).

4.7.2.2 Test Matrix

Two concentrations of two different inhibitors were tested (Table 8). Both inhibitors were based on quaternary ammonium chloride, one of them with a known formulation labeled as K2 in the text above and the other being a similar commercial inhibitor formulation, labeled P1.

Table 8. Experimental conditions - Hilly - Terrain System

Material	X-65 Carbon steel
Test solution	1 wt.% NaCl
Temperature	25 °C
pH	5.0
Inhibitor	• Proprietary "quat" (labeled as P1) • Known formula: alkylbenzyl dimethyl ammonium chloride (labeled as K2)
Inhibitor concentration	0, 20, 50 ppm
Time exposure	24 hours
Superficial gas velocity	1, 3, 6, 10 m/s
Superficial liquid velocity	1 m/s
Measurement techniques	Linear polarization resistance Weight loss

4.7.2.3 Results and Discussion

The effect of multiphase flow has on protective inhibitor films was evaluated for different concentrations (0, 20ppm, 50ppm) for the two different inhibitors: K2 and P1. Figure 75 shows the effect that multiphase flow has on corrosion rate when the system has no inhibitor (baseline). Each time that the superficial gas velocity (v_{sg}) was increased, the corrosion rate increased; from 5mm/year when the v_{sg} was 1m/s to 6mm/year when the v_{sg} was 3m/s then 7.5mm/year when the v_{sg} was 6m/s.

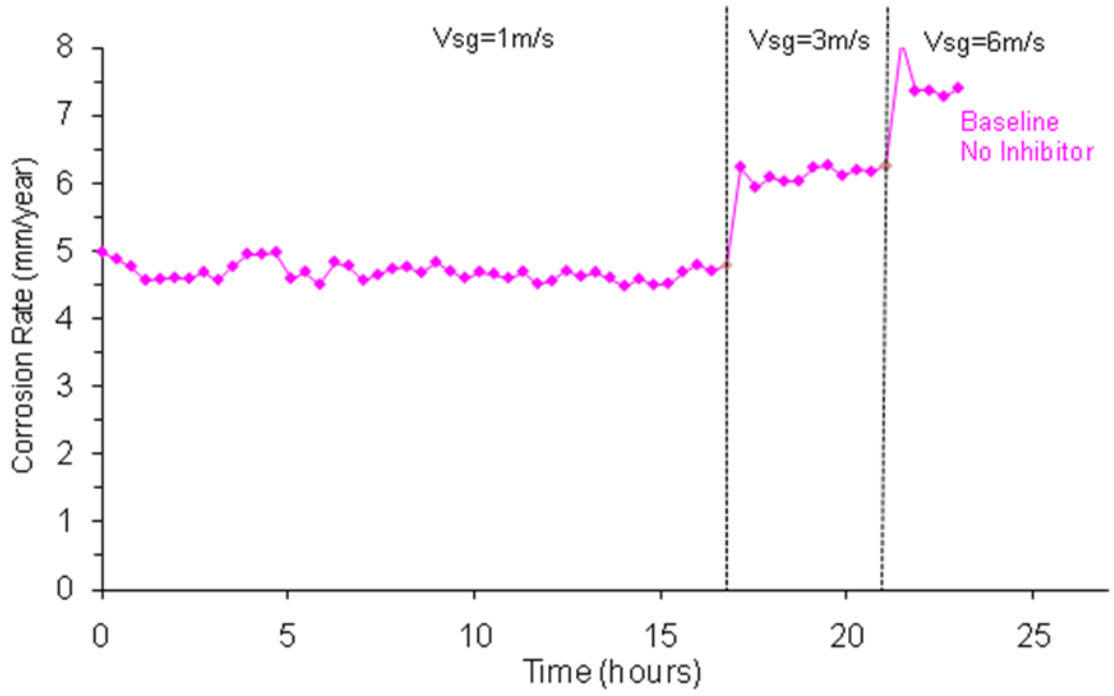

Figure 75. Baseline corrosion rate from LPR (no inhibitor present). Superficial gas velocity changed from 1 m/s to 3 m/s and from 3 m/s to 6 m/s. (pH 5.0, 25°C, superficial liquid velocity 1 m/s and pCO_2=0.98 bar).

Figure 76 shows corrosion rate from WL in three different locations in the hilly terrain System. Weight loss measurements were performed twice to ensure reproducibility of measurements in the location identified in Figure 74 B. Flow induced corrosion was higher on the bottom bend in which the turbulence is also higher. At the top bend, the flow induced corrosion was the lowest.

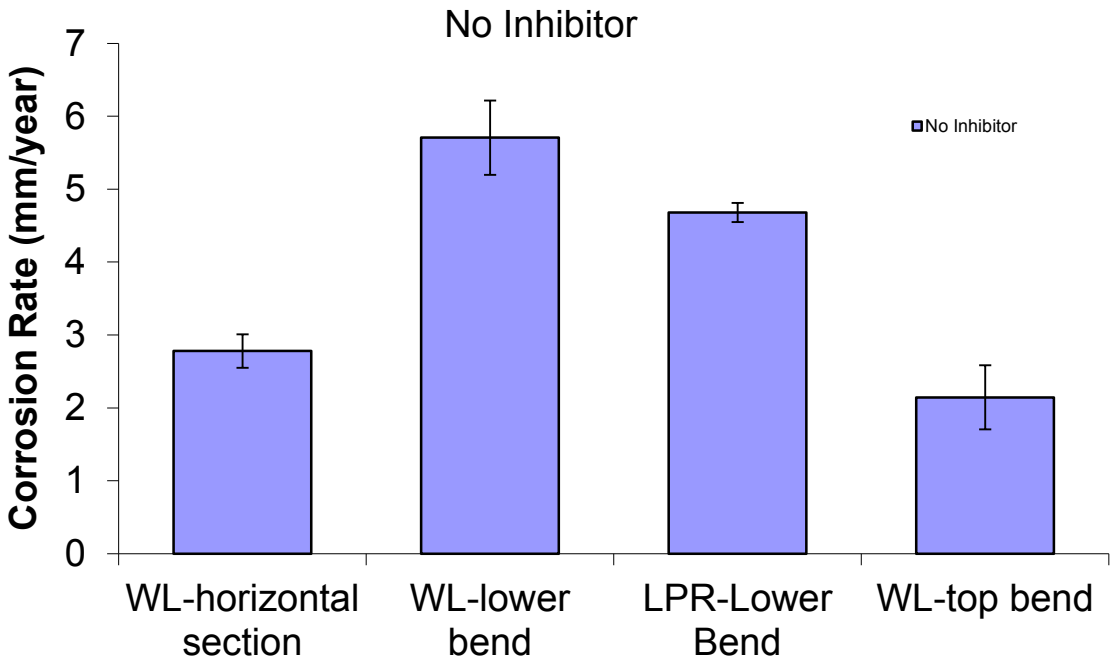

Figure 76. Baseline corrosion rates, no inhibitor present, from weight loss measurements for three different locations in the hilly terrain system (pH 5.0, 25°C, superficial gas velocity 1 m/s, superficial liquid velocity 1 m/s and pCO_2=0.98 bar).

Figure 77 shows the performance of thin protective films made with 20 ppm and 50 ppm of inhibitor P1. When the system had a concentration of 20 ppm, P1 did not show adequate protection, reducing the corrosion rate from 4.6 mm/year only to 2.8mm/year, with an efficiency of 40%. However, inhibitor P1 was not affected by the increase in v_{sg}. The same effect is seen with 50ppm of P1. The efficiency for the 50 ppm concentration of inhibitor P1 was 85%.

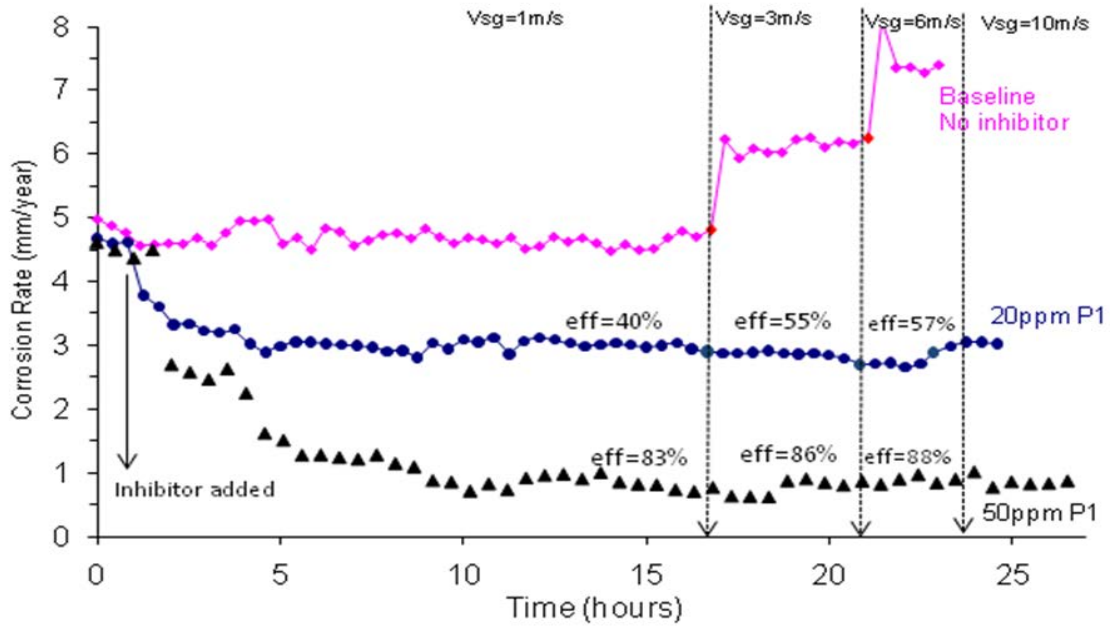

Figure 77. Corrosion rate from LPR when the system has 20 and 50 ppm of inhibitor P1. Superficial gas velocity was changed from 1 m/s to 3m/s, from 3m/s to 6m/s, and from 6 to 10 m/s (pH 5.0, 25°C, superficial liquid velocity 1 m/s and pCO_2=0.98 bar).

Figure 78 shows the performance K2. The protective film made with a concentration of 20ppm gives an efficiency of 63%, and this did not change when v_{sg} was increased to 3m/s or to 6m/s. When the system had 50ppm of K2, the inhibitor reduced the corrosion rate from 4.6mm/year to 1.4mm/year, giving an efficiency of 80% that was also unaffected by an increase in v_{sg}.

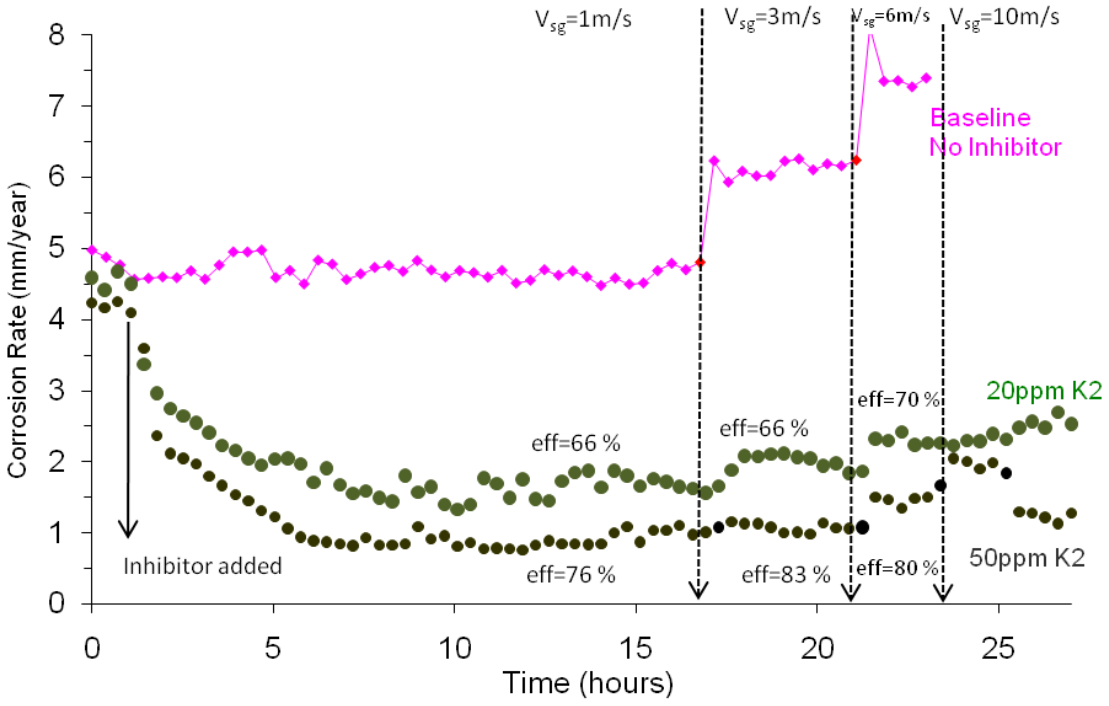

Figure 78. Corrosion rate from LPR when the system has 20 and 50 ppm of inhibitor K2. Superficial gas velocity was changed from 1 m/s to 3m/s, from 3m/s to 6m/s, and from 6 to 10 m/s (pH 5.0, 25°C, superficial liquid velocity 1 m/s and pCO_2=0.98 bar).

These results show that these two inhibitors did not give good protection against CO_2 corrosion under the tested multiphase conditions. One is tempted to jump to the "obvious" conclusion that this was due to high shear stresses seen in multiphase slug flow. It turns out that this would be wrong.

The corrosion rate was also measured in parallel glass cell using the same electrolyte as in the flow loop, and compared with independent glass cell measurements reported previously. Via simple comparisons of corrosion rates it was established that approximately two thirds of the inhibitor which was added to the flow loop was not present in the solution transferred from the flow loop into the glass cell. The inhibition

obtained at the nominal 20 ppm concentration in the flow loop was equivalent to the protection obtained at 5 ppm in the glass cell experiment (see Figure 79 a and b). This loss of inhibitor in the flow loop was traced back to formation of foam in the loop (see Figure 80), where much of the inhibitor was adsorbed, as explained in the following section.

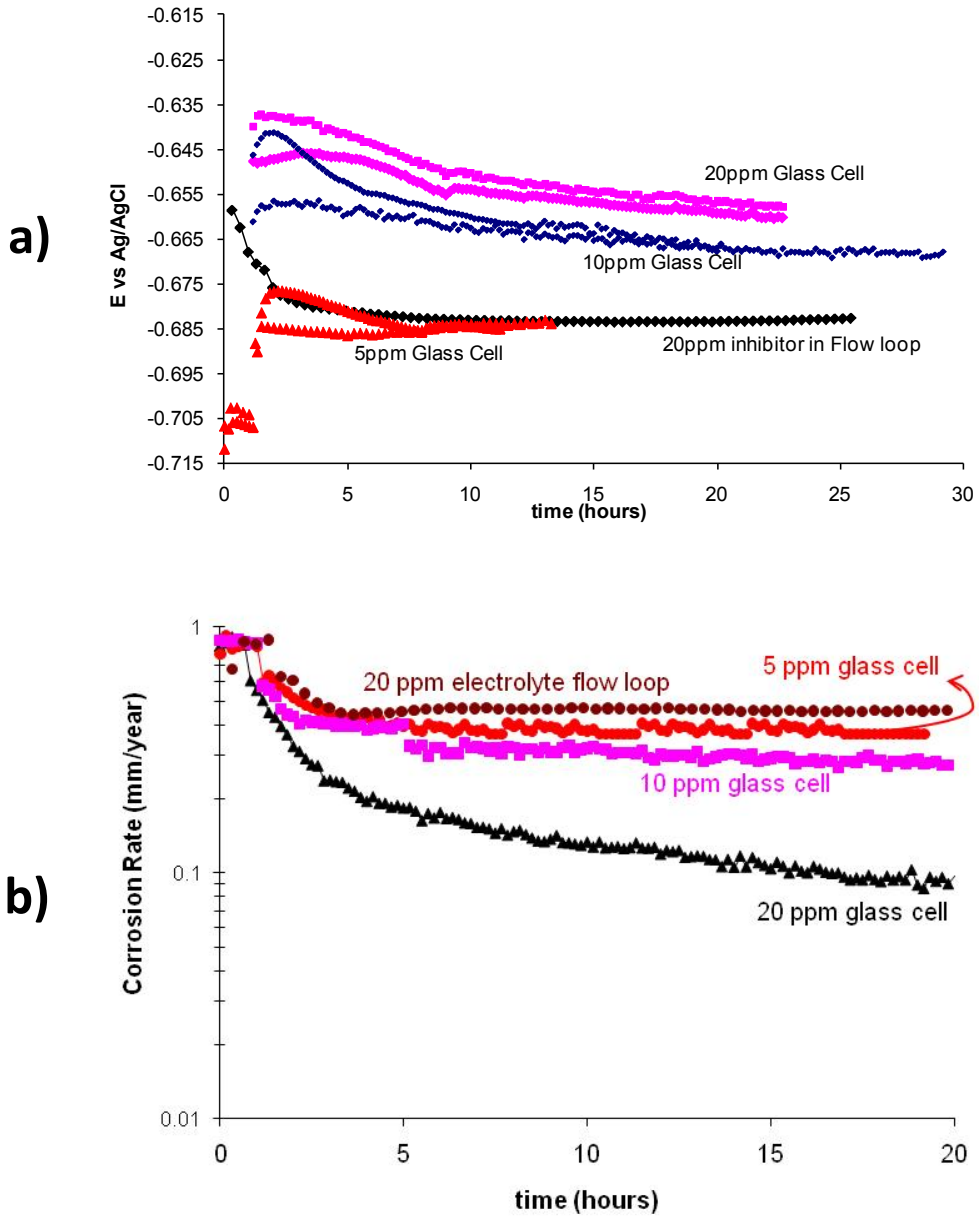

Figure 79. Comparison of a) corrosion potential and b) corrosion rate for three different concentrations of inhibitor P1 in a glass cell with 20ppm of inhibitor flowing in the flow loop.

Figure 80. Formation of foam in the Hilly-Terrain system when the flow loop has 20 ppm of inhibitor P1.

Chapter 5. Effect of Foaming on Corrosion Inhibitor Performance

5.1 Introduction

Foaming represents a severe problem for the performance of inhibitors due to the "consumption" of the inhibitor by adsorption onto the interface between the liquid and the gas phase. To counter this in field operations, operators sometimes resort to addition of de-foaming agents that can potentially affect adversely corrosion inhibitor performance. In wet gas systems where the amount of transported hydrocarbons is low the formation of foam is commonly experienced once the inhibitor is injected. The foam reduces the performance of inhibitor due to its absorption/consumption at the interface with the gas phase; this has the potential to result in damage to equipment used in gas production[147–149].

Foams are formed when the gas is dispersed in liquids. However, to maintain the foam stability often a "foaming agent" is needed. The organic corrosion inhibitors used in this study, K1 and K2, qualify as foaming agents. The inhibitors improve the foam stability by reducing: the thinning, the coalescence and the rupture of the gas bubbles. The tendency of the surfactant is to be adsorbed at the gas-liquid interface, with the hydrophilic head in the water phase and the tail into the gas phase (foam lamella) instead of being adsorb on the metallic surface[150]. The adsorption at the gas-liquid interface has been reported to be energetically stable[18].

5.2 Experimental Setup

5.2.1 Equipment

Loss of inhibitor performance due to foaming was determined in this series of experiments in which the corrosion rate was measured using the linear polarization technique. The first set of experiments was conducted in a glass cell with 1018 carbon steel as a rotating cylinder electrode (Figure 10). A concentric platinum wire was the counter electrode and a saturated Ag/AgCl acts as reference electrode connected externally *via* a Luggin capillary. The glass cell was filled with de-ionized water and 1 wt.% NaCl. The working electrode with 5.4 cm^2 of exposure area was polished using 320, 400, and 600 grit abrasive silicon carbide paper, wetted constantly with isopropanol. After one hour of pre-corrosion the required amount of inhibitor was added into the system, see Table 9.

5.2.2 Experimental Procedure

CO_2 gas was bubbled through a gas diffuser located in the center of the glass cell to generate the foam. The organic corrosion inhibitors add stability to the foam as was discussed above. For the experiment with foam the CO_2 gas was constantly bubbled in the glass cell during the entire experiment. Figure 81 shows the gas-liquid interface with the foam generated on the gas-liquid surface.

Figure 81. Gas/liquid interface with the foam.

To avoid foam formation in other experiments, before the addition of the corrosion inhibitor the gas diffuser was moved to the gas phase.

5.2.3 Test Matrix

Table 9. Experimental conditions – Small scale experiments set up to evaluate the loss of inhibitor due to adsorption at the gas/liquid interface

Test solutions	1 wt.% NaCl
Test material	1018 carbon steel
Temperature	25°C
Partial pressure of CO_2	0.98 bar at 25°C
pH	5.0
Characterization	Corrosion rate from polarization resistance from -5 mV to 5 mV vs E_{oc}
Consumption of corrosion inhibitor at gas/liquid interface	Measured in the glass cell (see Figure 81)

5.2.4 Results

Figure 82 shows the performance of corrosion inhibitor K1 (imidazoline based). An efficiency of 94% was reached when the inhibitor concentration was 20 ppm without foaming (blue bars in Figure 82). Concentrations of 10 ppm and 20 ppm were then used in experiments under foaming conditions in the glass cell. The results show that under foaming conditions the inhibitor efficiency was reduced (orange bars in Figure 82). When the solution contained 20 ppm of inhibitor its availability was reduced by a factor of two due to foam, i.e. the performance was equivalent to having 10 ppm corrosion inhibitor without foam. Even when the system contained only 10 ppm of inhibitor and foaming occurred, this produced a reduction in the inhibitor film performance. This reduction was not as pronounced as that observed for 20 ppm of corrosion inhibitor.

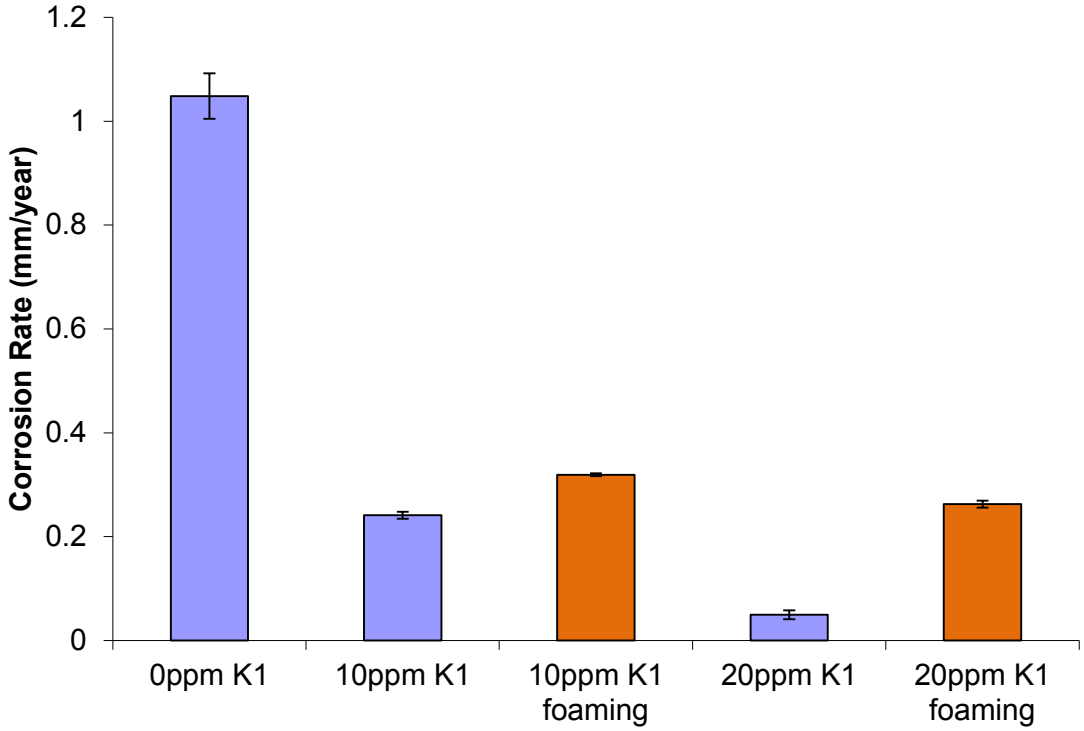

Figure 82. Corrosion Inhibitor K1 (imidazoline based) performance in glass cell, and effect of foam on its performance (pH 5.0, 25°C, 1000 rpm and pCO_2=0.98 bar). Blue bars denote no foaming conditions. Orange bars denote foaming conditions

Figure 83 shows the performance of inhibitor K2 (“quat”) in a glass cell with and without foaming. When the system has 160 ppm of corrosion inhibitor the efficiency reached 92% without foaming. However, the performance was significantly degraded when foam was formed (by approximately a factor of 2), i.e. the performance was equivalent to having 80 ppm without foam. The same happened when 80 ppm of inhibitor with added. The inhibitor availability was reduced by half, equivalent to the performance seen at 40 ppm of corrosion inhibitor without foam.

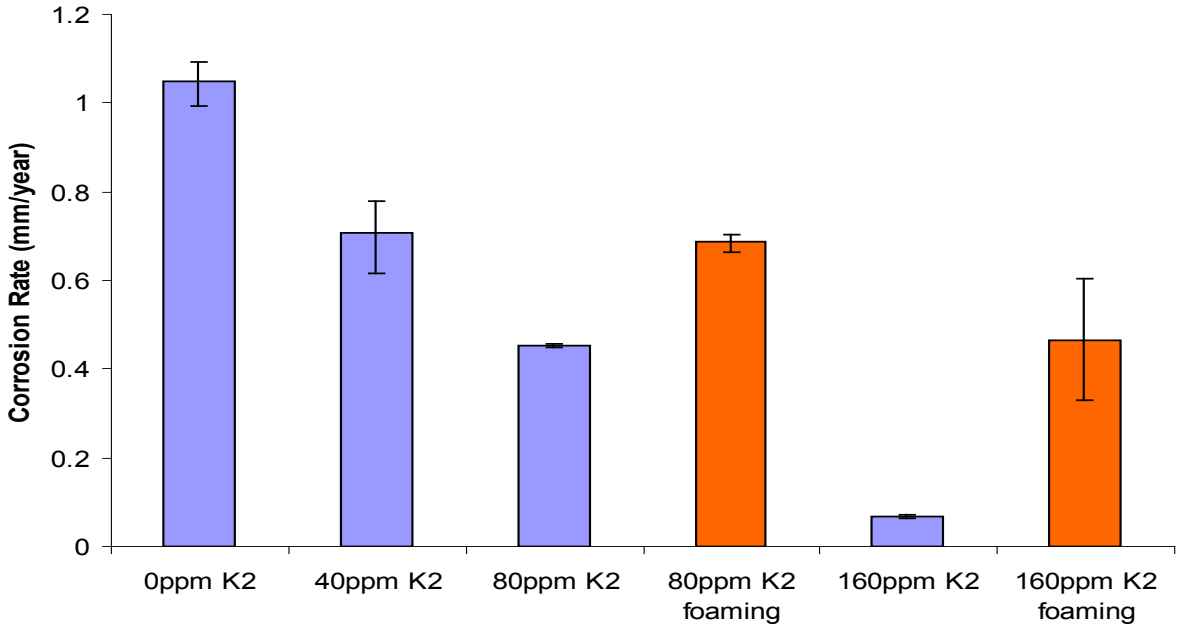

Figure 83. Corrosion inhibitor K2 (“quat”), performance in glass cell and effect of foam in its performance (pH 5.0, 25°C, 1000 rpm and pCO_2=0.98 bar).

In Figure 84 the performance of inhibitor K3 (sodium thiosulfate) was evaluated. The results showed that the maximum efficiency was reached when the system has 0.2 ppm of inhibitor, achieving 96% efficiency. Sodium thiosulfate is a non-surfactant polyatomic ion, therefore there can be no consumption of inhibitor due to foam formation, therefore its performance was not affected

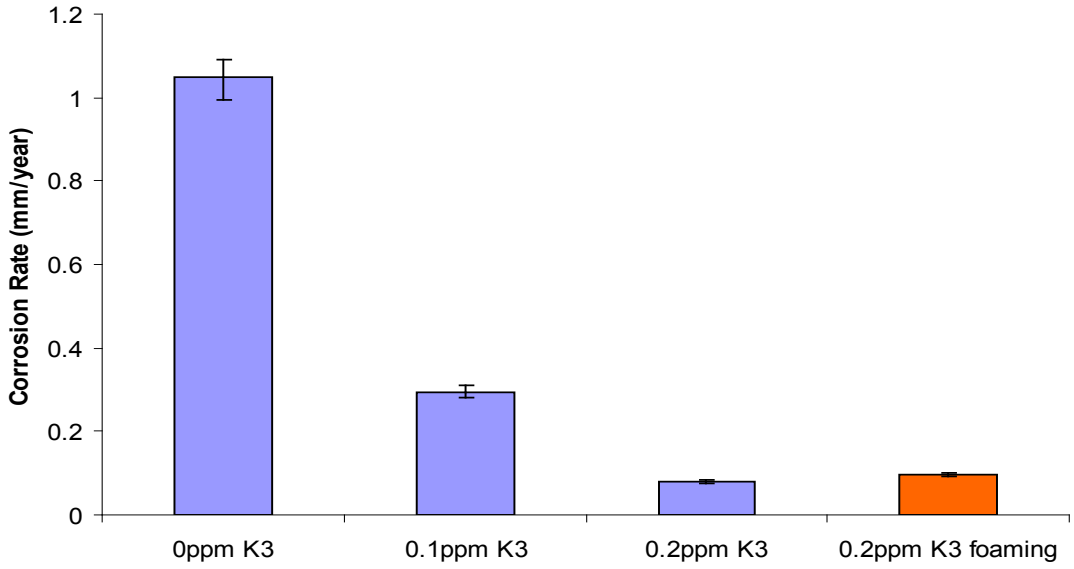

Figure 84. Corrosion inhibitor K3 (sodium thiosulfate) performance in glass cell, and effect of foam on its performance (pH 5.0, 25°C, 1000 rpm and pCO_2=0.98 bar).

The performance of inhibitor K4, a blend between inhibitor K1 + inhibitor K3 (imidazolinium + sodium thiosulfate) is plotted in Figure 85. The results show maximum protection was reached when the system has 1 ppm of inhibitor K4, reaching 93% efficiency. From Figure 85 it is easy to ascertain that the foam does not have a pronounced impact on inhibitor K4 as happen with the surfactant inhibitors K1 and K2. Blending inhibitor K3 with the surfactant K1 improved the performance, as was discussed in the sections above. This is due to the inhibitor K3 which is not a surfactant and therefore is not affected by the foam.

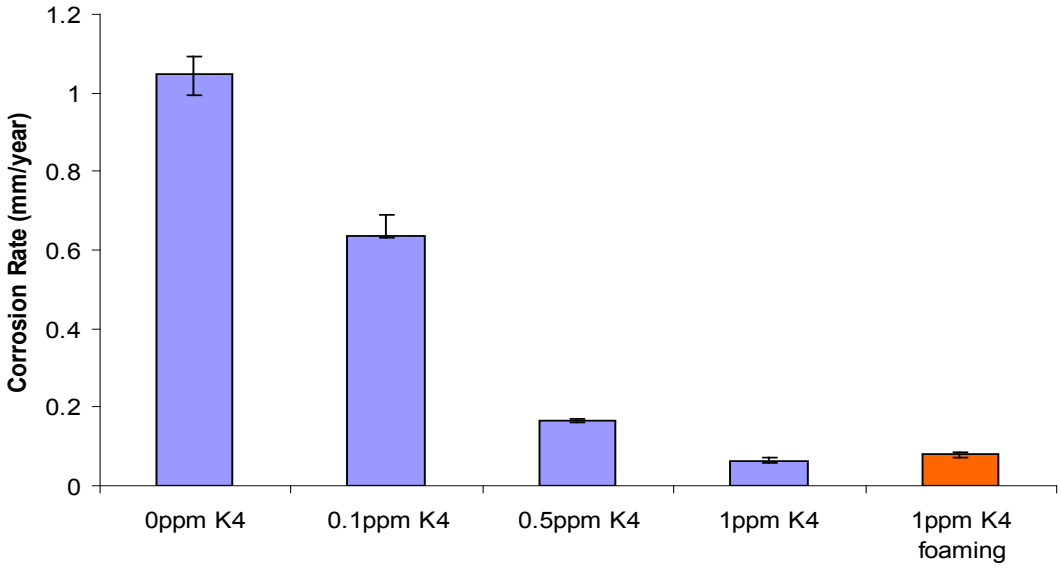

Figure 85. Corrosion inhibitor K4 (imidazolinium + sodium thiosulfate) performance in glass cell, and effect of foam on its performance (pH 5.0, 25°C, 1000 rpm and pCO_2=0.98 bar).

Figure 86 shows the performance of inhibitor K5 (blend of "quat' + thiosulfate) and the effect of foam on its performance. The plot illustrates that the maximum efficiency (92%) was reached when the system had 0.5 ppm of inhibitor. The plot also shows that the foam had a small effect on the availability of inhibitor in the system. When the system foamed the performance of the film was reduced, reaching the same corrosion rate than when the system has 0.3 ppm of inhibitor in the glass cell. This is a combined effect of the foam on the two components of K5: the component K1 which was affected by the foam and K3 which was not.

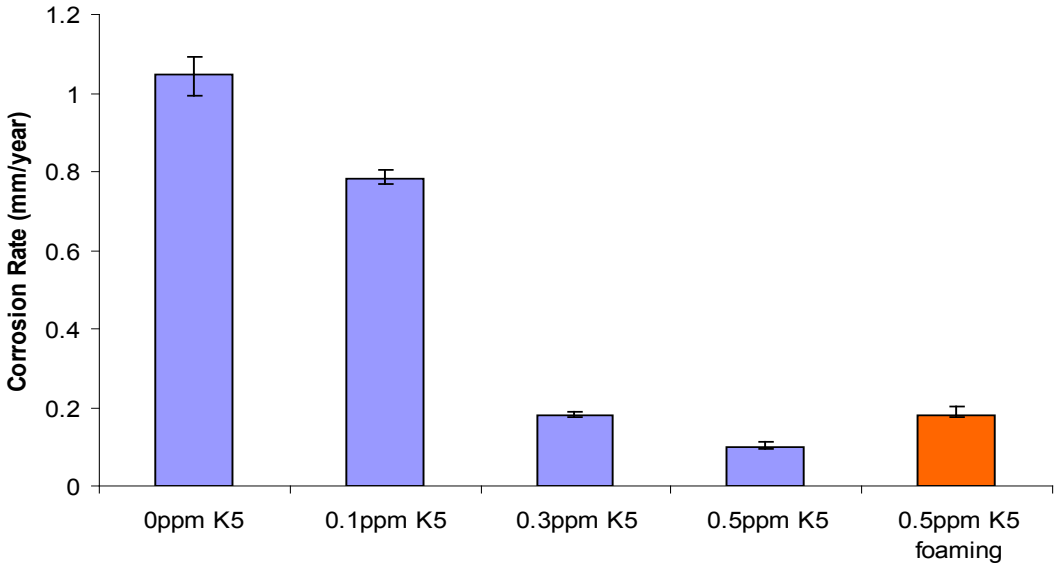

Figure 86 Corrosion Inhibitor K5 ("quat" + sodium thiosulfate) Performance in glass cell, and effect of foam on its performance (pH 5.0, 25°C, 1000 rpm and pCO_2=0.98 bar).

Chapter 6. Solid/Liquid Multiphase Flow

6.1 Introduction

In oil and gas production solids (sand and other small inorganic particles) can be present[85]. Other organic solids such as waxes or asphaltenes can also be present in the produced oil or gas[151]. In gas transportation under cold conditions the formation of solid hydrates is another common issue. It has been suggested that this type of multiphase flow including small amounts of solids can affect the internal corrosion rate of mild steel pipelines due to mechanical erosion of the protective corrosion inhibitor film [87,87,90].

The debate on how the presence of solids in multiphase pipeline flow affects the performance of a corrosion inhibitor film has been ongoing for a while. There are two main hypotheses. The first is related to the loss of inhibitor due to adsorption onto the surface of sand [85,150–152]. The other effect is mechanical erosion of the corrosion inhibitor film by impingement of sand particles [89,121,153–156]

Blumer and Babcock[151] (1996) studied the effect of different types of solid on loss of inhibitor due to adsorption onto sand. They found that the main factors are: the inhibitor concentration, the inhibitor composition and the type of solids.

In more recent works, McMahon *et al.*[85],(2005) and Ramachandran[152] (2005) also reported that the inhibitor loss also depends of the amount of solids in the system. McMahon, *et al.* [85], (2005) found that concentrations of sand below 35 pounds per thousand barrels (≈ 10 ppm) do not have a significant effect on the losses of inhibitor due to adsorption. By increasing the amount of sand, the inhibitor performance decreases significantly.

Obviously when inhibitor is adsorbed onto the sand surface then it is not available for inhibition of the steel surface corrosion [85,151]. This preferential adsorption of the corrosion inhibitor onto a particular substrate is related to the charge of the surface, in this scenario the competition is between sand and steel surface [127,150]. It was discussed in previous chapters that cationic corrosion inhibitors adsorb preferentially on negatively charged surfaces.

In a paper published by Atkin, *et al.* [157], (2000) ' the authors reported that the adsorption of surfactants onto silica is strongly dependent on the surfactant concentration. Thus, if the surfactant concentration reaches the CMC then the adsorption onto silica is accelerated. The main argument is related to the micelles acting as a bridge between the silica surface and the monomer to be adsorbed. In a different paper Atkin *et al.* [158], (2001) reported that the surfactant adsorption process onto silica is affected by the composition of the electrolyte. It was stated by Atkin *et al.* [158], (2001) and Bera *et al.* [159], (2013) that the pH is playing an important role on the adsorption of surfactants on silica surfaces. The pH affects the adsorption of cationic surfactants onto sand because of the ionization of hydroxyl group that changes the sand surface to become more negative. As a consequence cationic surfactants adsorption is enhanced.

Under the scenario of electrolytic solutions at lower pHs the adsorption of surfactants does not result in a distinguishable mass gain onto silica. In his work Atkin demonstrated that at pH 5.5 the adsorption of cationic surfactant was very low, and the adsorption mechanism was purely electrostatic. At the lower levels of pH in electrolytic solutions the cationic surfactant will compete with the cations in the electrolyte for

adsorption sites. Once the pH reaches more basic values the sand surface will increase surface charge allowing an easy adsorption of cationic surfactant[158].

Knag, *et al.*,(2004) [22] reported that adsorption of inhibitor onto silica is favored but that the adsorption onto iron and cementite is faster, leading to protection of the steel against corrosion just below the CMC.

The effect that solids have on the inhibitor performance is not only due to selective adsorption, but also to the mechanical erosion process that is suspected to play a key role in the inhibitor performance. The damage of steel caused by mechanical erosion forces and the interaction with electrochemical corrosion processes, is known as erosion-corrosion[88]. According to Shadley, *et al.*, (1996) [86] there are three scenarios related to the severity of the erosion condition:

1) Low erosion: a $FeCO_3$ protective scale/corrosion product layer is formed with low metal loss rate at low velocities.

2) Intermediate erosion: Impingement of solids on the wall pipe removes some or part of the layer, leading to localized corrosion.

3) High erosion: Sand erosion removes all the scale generating high metal loss rates.

There is far less information about the effect of sand erosion of corrosion inhibitor films. In this chapter, the effect of two-phase (solid/liquid) flow was investigated, in order to observe if sand erosion plays an important role in inhibitor performance. Furthermore, the erosion by sand was thought to be the most aggressive test of the

inhibitor film mechanical integrity and protectiveness, presenting a much more severe challenge than all the other multiphase scenarios described in the sections above.

6.2 Objectives

Both scenarios were investigated: selective adsorption of inhibitor onto sand as well as mechanical erosion. The former was investigated in small scale glass cell experiments, while the latter was done in a large scale flow loop.

6.3 Small Scale

6.3.1 Equipment

Small scale experiments were conducted in a glass cell as previously described for corrosion inhibitor characterization. Experiments relating to loss of corrosion inhibitor in the flow loop due to adsorption on sand were performed using a glass cell connected in parallel to the flow loop. Comparison of corrosion rate measured in small scale tests and in the glass cell connected in parallel to the flow loop was used to distinguish the effect of corrosion inhibitor selective adsorption from the erosive effect.

The sand used in this work was characterized previously by Addis (2008)[156] in his thesis research work. The average sand size reported by Addis (2008) was 275 microns, which represent coarse sand, according to McMahon *et al.,* (2005) [86]. Sand characteristics are reported in Table 10, experiments were conducted with 2 and 10 wt.% of sand. Before the beginning of any experiment the sand was washed with de-ionized water.

Table 10. Sand – physical characteristics

	Sand
Mean particle diameter (microns)	275
Specific gravity (H_2O = 1)	2.6
Specific Sand Surface area (cm^2/g)	83.91

6.3.2 Experimental Procedure

The 1wt.% NaCl electrolyte was deoxygenated by purging with CO_2 for one hour before the beginning of each experiment. The pH was adjusted with deoxygenated $NaHCO_3$, as required, to reach a value of 5.0. The working electrode was polished using 200, 400, 600 grit silicon carbide paper, rinsed with isopropyl alcohol, mounted in the holder, and placed into the glass cell. The baseline corrosion rate, conducted with only purged electrolyte in the glass cell, was measured over an hour. To determine the corrosion rate, linear polarization resistance measurements were conducted every 20 minutes. After the first hour, the working electrode was removed and the clean sand (2 or 10 wt. %) was added into the system and stirred continuously. The working electrode was polished again, and put back into the system. In this way the corrosion rate with sand was measured for one hour. After the first hour of specimen exposure with sand, 20 or 50 ppm of inhibitor K2 which is soluble in water was added into the system, and the linear polarization resistance was measured every 20 minutes until the end of the experiment.

6.3.3 Test Matrix

The first set of experiments was conducted in an electrochemical cell in order to evaluate the inhibitor loss due to its adsorption on sand, Table 11 Different concentrations of corrosion inhibitor K2 (Alkylbenzyl dimethyl ammonium) were tested with different concentrations of sand in the system. Measurements of the corrosion rate and open circuit potential were performed to determine if inhibitor was lost due to selective adsorption.

Table 11. Test matrix - Inhibitor adsorption onto sand

Test solution	1 wt.% NaCl
Test material	Carbon steel 1018
Temperature	Room temperature (25°C)
Partial pressure of CO_2	0.98 bar
pH	5.0
Flow velocity (rotation speed of RCE)	1000 rpm
Inhibitor kind	Alkylbenzyl dimethyl ammonium (K2)
Inhibitor concentration	5, 10, 20, 50 ppm
Sand concentration	0, 2, 10 wt.%
Electrochemical analysis	LPR and open circuit potential
Equipment	2 liter glass cell

6.3.4 Result and Discussion

Figure 87 shows the effect of different concentrations of inhibitor K2 (5, 10, 20, 50 ppm) on the corrosion potential. When the corrosion inhibitor concentration is increased, the corrosion potential also increased. After eight hours of exposure, the corrosion potential did not change significantly and remained stable for the rest of the experiment. Figure 88 shows the corrosion rate measured for the same corrosion inhibitor concentrations. In this plot, the effect that 20 and 50 ppm of inhibitor have on the final corrosion rate is very similar. When the system has 20 ppm, the corrosion rate was 0.06 mm/year, and when the system has 50 ppm of inhibitor, the final corrosion rate was 0.04 mm/year. This would indicate that the optimum concentration of inhibitor is between 20 and 50 ppm.

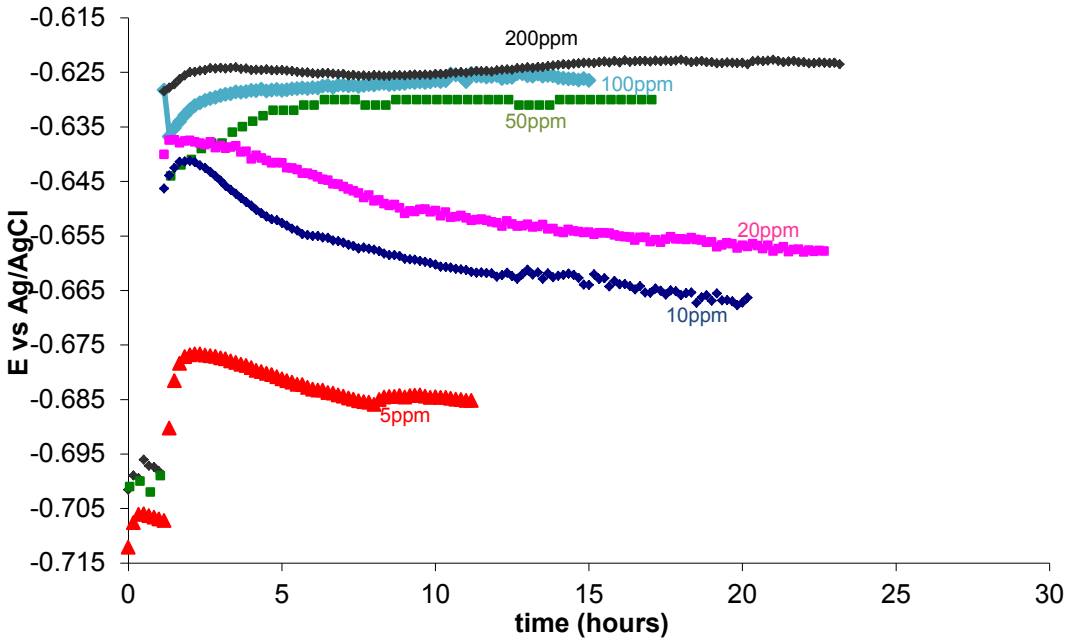

Figure 87. Effect of different concentrations of inhibitor K2 on the corrosion potential (pH 5.0, 25°C, 1000 rpm and pCO_2=0.98 bar).

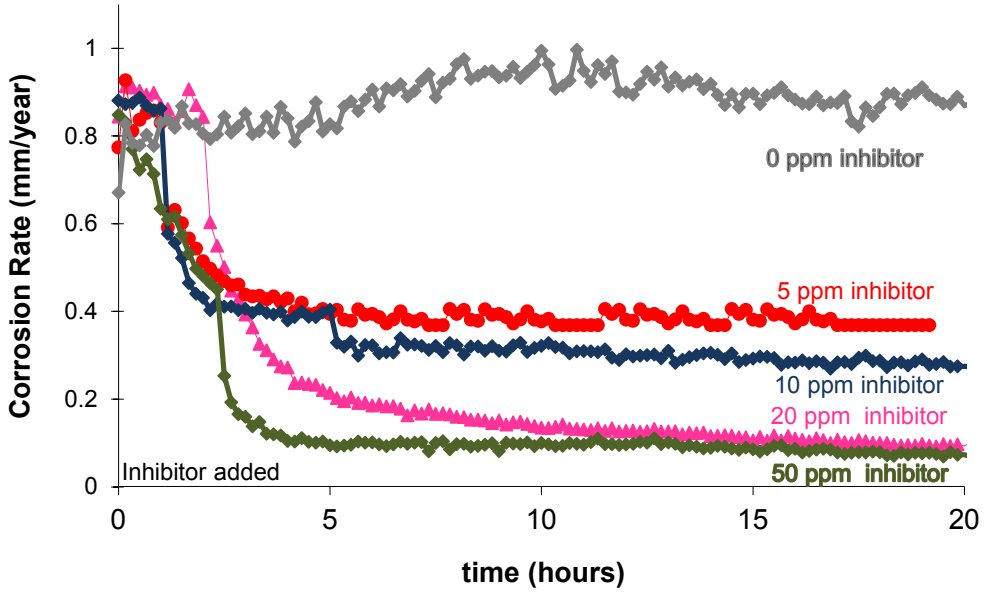

Figure 88. Effect of different concentration of inhibitor K2 on the corrosion rate (pH 5.0, 25°C, 1000 rpm and pCO_2=0.98 bar).

Knowing the relationship between the corrosion potential and corrosion rate in a system free of solids, the effect of sand in the system was evaluated. Figure 89 shows the effect that 2 wt.% sand has when the system has 20 ppm of inhibitor. Figure 90 shows that the corrosion rate increases from 0.06mm/year to 0.13mm/year, which is significant but still not in the range critical for field operations.

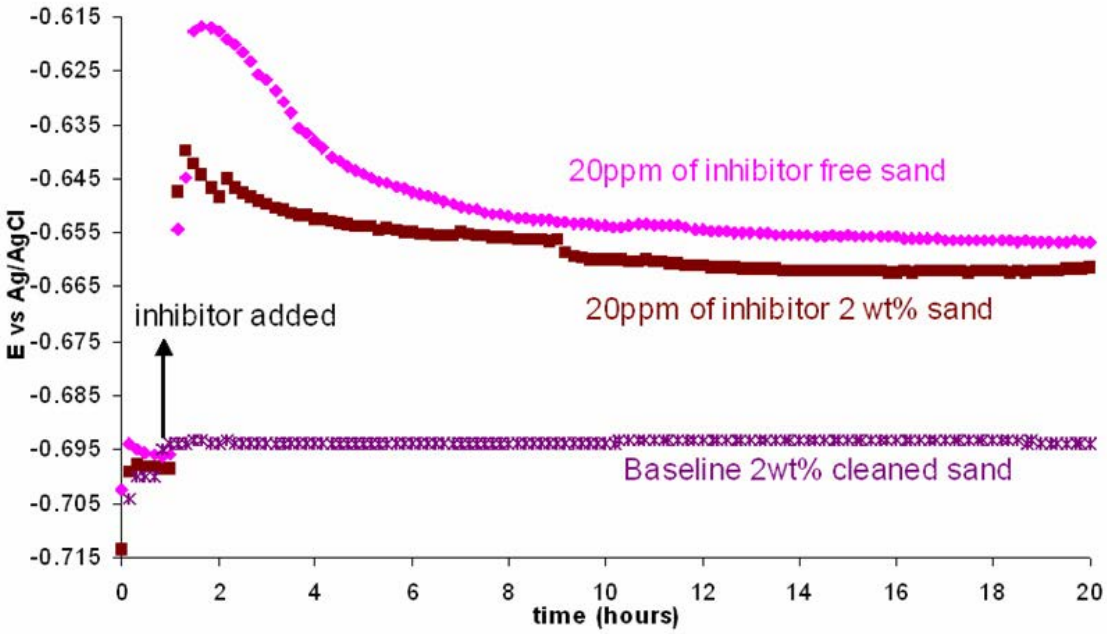

Figure 89. Corrosion potential for 20ppm of corrosion inhibitor K2 (“quat” type) with and without 2 wt.% sand (pH 5.0, 25°C, 1000 rpm and pCO_2=0.98 bar).

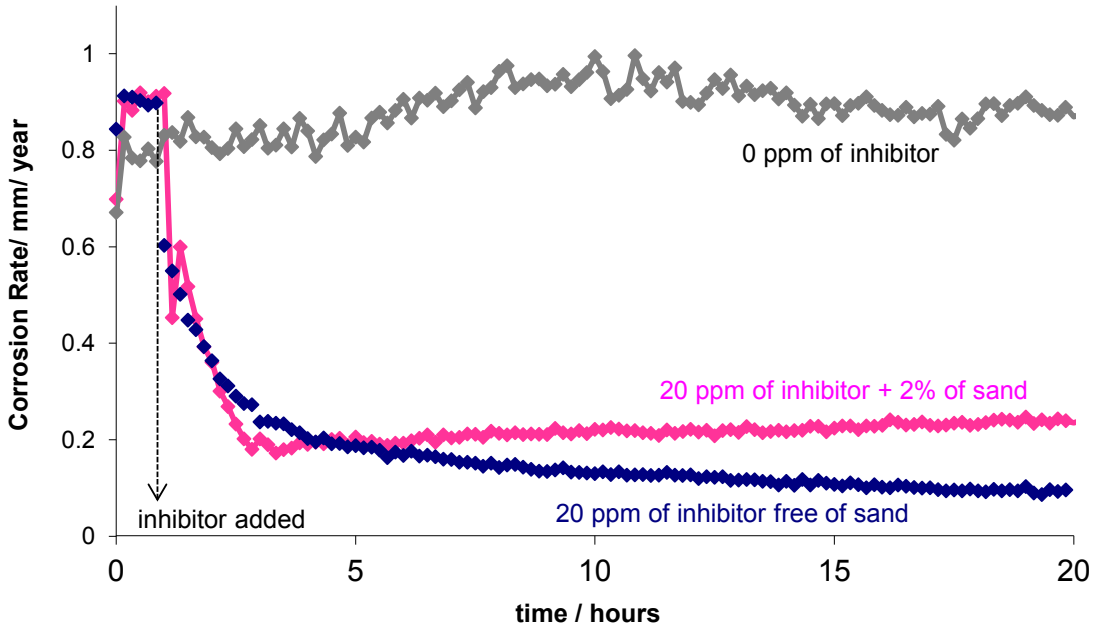

Figure 90. Corrosion rate for 20ppm of corrosion inhibitor with and without 2 wt.% sand, (pH 5.0, 25°C, 1000 rpm and pCO_2=0.98 bar).

It was therefore important to look at this effect at a higher sand concentration, where 50ppm of inhibitor was added in the system with 2 wt.% sand and then with 10 wt.% sand Figure 91 shows the corrosion potential for this experiment. In this plot, it is clear that when sand concentration is higher the corrosion potential decreased significantly (50mV). This drop in the corrosion potential is related to the loss of corrosion inhibitor by adsorption onto sand.

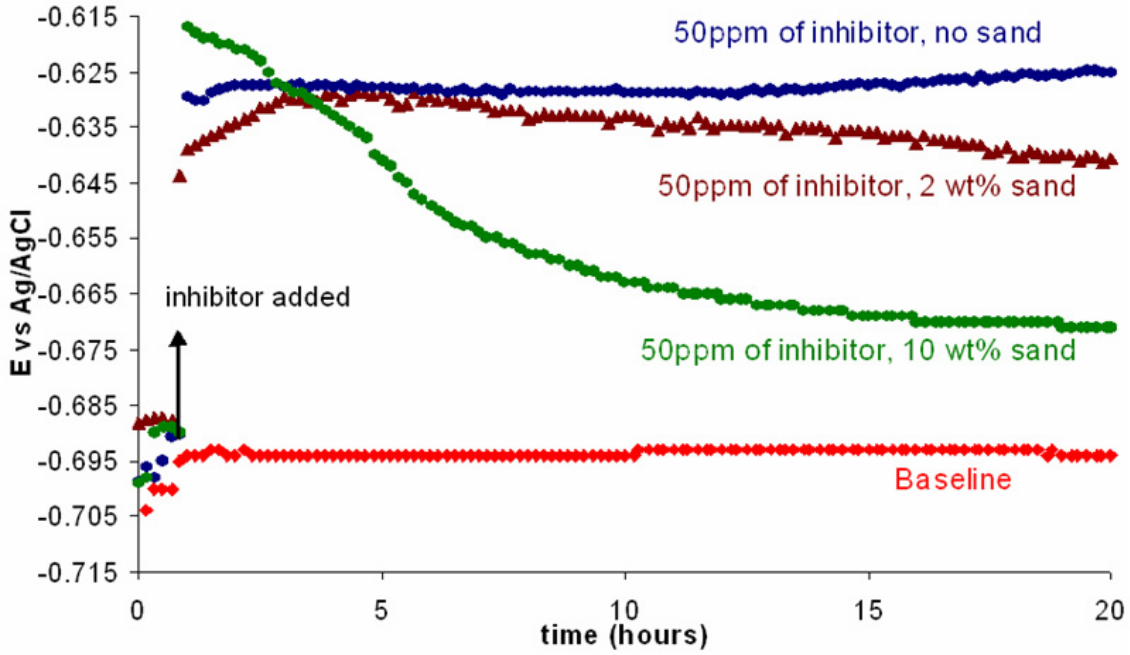

Figure 91. Corrosion potential for 50ppm of corrosion inhibitor with 2 and 10 wt.% sand (pH 5.0, 25°C, 1000 rpm and pCO_2=0.98 bar).

Figure 92 shows the corrosion rate for 50 ppm of corrosion inhibitor with 2 and 10 wt.% sand at pH 5.0, 25ºC, pCO_2 of 0.96 bar, and RCE at 1000rpm. With more sand added, the performance of the inhibitor was affected, but overall, even with the very large sand concentration (10%), the effect was not as dramatic as it was originally thought.

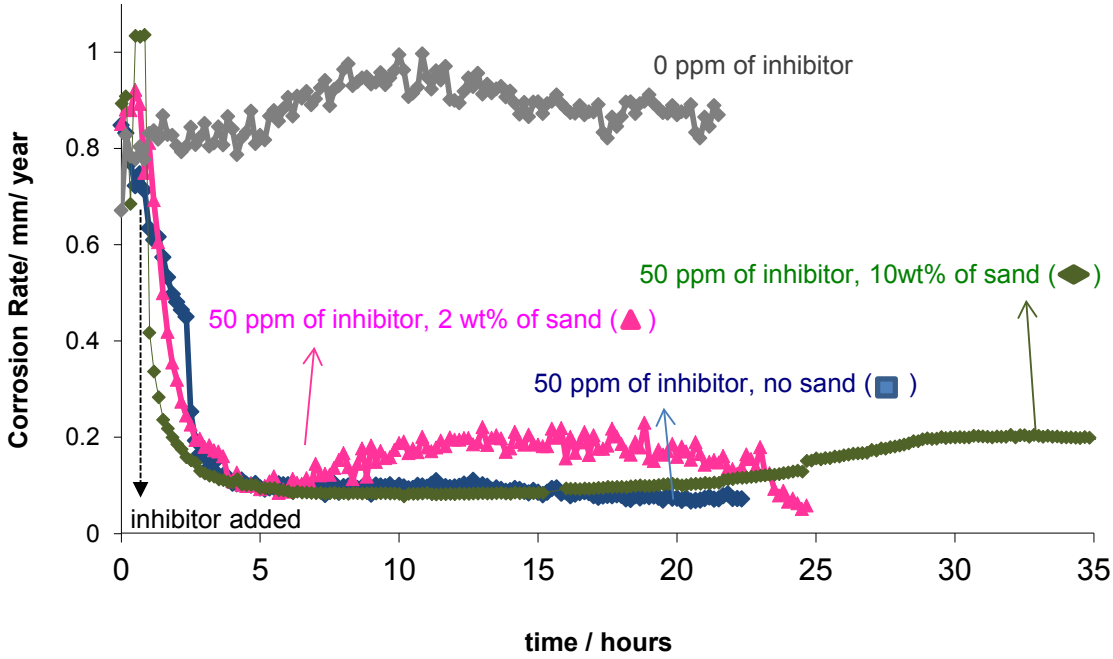

Figure 92. Corrosion rate for 50ppm of corrosion inhibitor with 2 and 10 wt.% sand, (pH 5.0, 25°C, 1000 rpm and pCO_2=0.98 bar).

6.3.5 Large Scale (Solid/Liquid Multiphase Flow) - Equipment

A 680 liter recirculating flow loop (Figure 93) with a five foot acrylic test section and fifty eight concentric coupons made of 1018 carbon steel was used to measure the effect of sand erosion on inhibitor film integrity using gravimetric and electrochemical techniques. The test section consists of four parts: an entrance section, a sudden pipe constriction, a protrusion, and a sudden pipe expansion. The entrance is a 15.24 cm long section of 10.2 cm ID, a constriction from 10.2 cm ID to 6.4 cm ID is a 60.96 cm long section. Halfway through the narrow 6.4 cm ID section is a 5 mm protrusion, followed by a sudden expansion from 6.4 cm ID to 10.2 cm ID. The final section is a 60.96 cm long section 10.2 cm ID, see Figure 91(b).

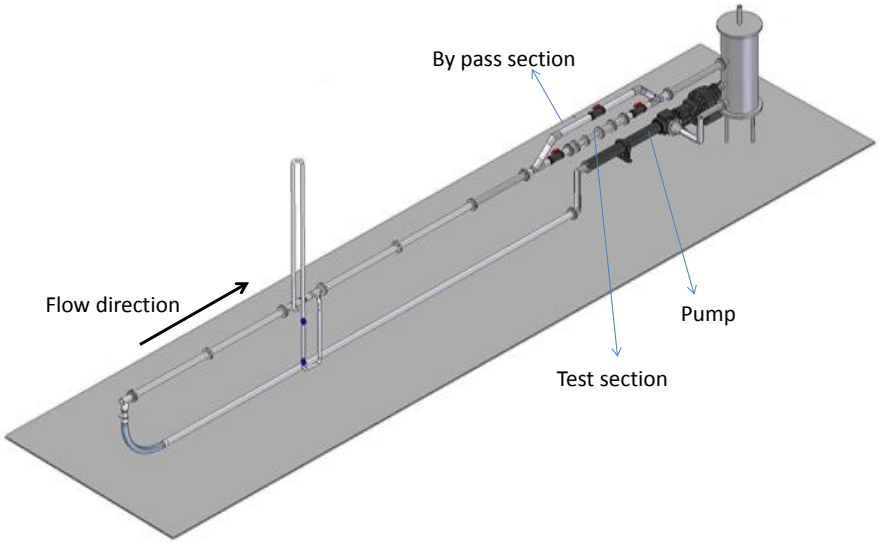

a)

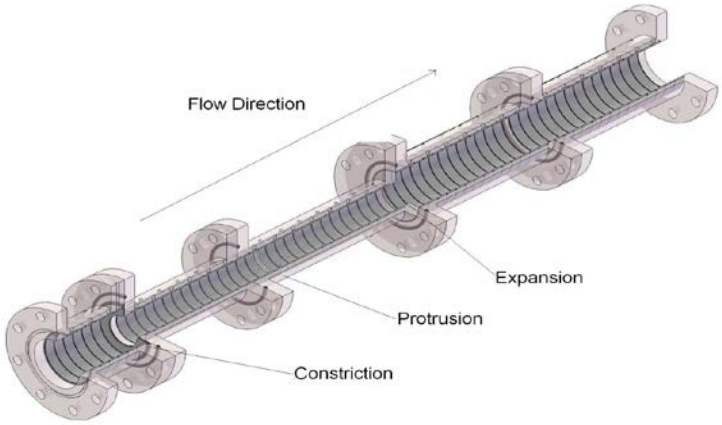

b)

Figure 93 (a) Erosion/corrosion test flow loop (b) test section.

6.3.6 Experimental Procedure

For every test, preparation of the flow loop and insertion of the test section was done by using a similar procedure. The flow loop was filled with 680 liter of water containing 1 wt.% NaCl. For pure corrosion and corrosion/erosion tests, with and without inhibitor, the system was purged with CO_2. For the pure steel erosion tests, the system was purged with pure N_2. For erosion and corrosion/erosion tests, the system was filled with 2 wt.% sand (see Table 13). The 2 wt.% sand was added and controlled during the experiments using the flow diversion tube (Figure 93). The concentration of dissolved oxygen was measured to be less than 10 ppb. The pH was measured and adjusted to the desired value before the test section was exposed to the multiphase flow. The 1018 carbon steel coupons were prepared first by cleaning with a bead blaster and then hand polished with 400 grit silicon carbide sandpaper prior to installation into the test section. The test section was installed in the flow loop and purged with a suitable gas (N_2 or CO_2) to eliminate the oxygen remaining in this area. Before the test section was opened to the test solution, the amount of desired inhibitor concentration was added to the system. After 15 minutes of deoxygenating the test section and equilibrating the inhibitor package with the electrolyte, the test section was opened to multiphase flow, the flow bypass closed, and the experiment started.

The inhibitor evaluated in this series of experiments was a commercial water soluble quaternary ammonium compound. The inhibitor was provided by the manufacturer at 60-80 % of active ingredients in a solvent - methanol. The inhibitor was

applied in concentrations of 20 and 50 ppm of supplied product to the total liquid in the test flow loop.

An electrochemical glass cell plugged in parallel with the flow loop was used to measure any loss of inhibitor due to its adsorption onto the sand surface. Measurement of corrosion potential and corrosion rate was performed in the glass cell using a side stream of the same solution that was flowing in the loop. It has been reported that corrosion potential is related to inhibitor concentration [160]. This relationship was used to identify any loss of inhibitor in the flow loop due to selective adsorption onto sand, or other surfaces.

6.3.7 Test Matrix

Table 12 shows the experimental test matrix used to study the effect of erosion/corrosion on corrosion inhibitor film performance, and is divided into three different sets of experiments. First, the evaluation of pure erosion rate was performed at pH 7.0 for different corrosion inhibitor concentrations. The second set of experiments was the study of pure corrosion evaluated at pH of 5.0 without any sand flowing through the loop. By combining these two sets of experiments it was possible to set up a baseline for comparison, and determine if the erosion/corrosion process has any synergistic effect on the corrosion inhibitor film performance. The third set were the erosion/corrosion experiments at pH 5.0 with 2 wt.% sand flowing through the loop.

Table 12. Experimental conditions - Determination of the erosion, corrosion and erosion/corrosion process on the corrosion inhibitor film performance.

Test solution	Water + 1 wt.% NaCl
Test material	1018
Temperature	25°C
Partial pressure of CO_2	1 bar
Velocity of the flow	2m/s 10 cm pipe & 5m/s 6.3cm pipe
Pure Erosion	
pH	7.0
Inhibitor type	Alkylbenzyl dimethyl ammonium chloride (K2)
Concentration	0, 20, 50ppm
Sand concentration flowing through the loop	2 wt.% NaCl
Pure Corrosion	
pH	5.0
Inhibitor type	Alkylbenzyl dimethyl ammonium chloride (K2)
Concentration	0, 20, 50ppm
Sand concentration flowing through the loop	0 wt.% NaCl
Erosion/Corrosion	
pH	5.0
Inhibitor type	Alkylbenzyl dimethyl ammonium chloride (K2)
Concentration	0, 20, 50ppm
Sand concentration flowing through the loop	2 wt.% NaCl

6.3.8 Results and Discussion

For the pure erosion experiments, the metal loss was determined by weight loss and was then adjusted by subtracting the small corrosion component determined by electrochemical measurement. In pure corrosion experiments the corrosion rate was

measured both by weight loss and electrochemically. The experimental conditions are listed in Table 12.

Results at 2 wt. % sand:

Figure 94 shows the combined analysis of the pure corrosion test and pure erosion test measured with the weight loss technique. When the system had 2 wt.% sand there was not a significant effect on surface erosion in the 10 cm ID pipe. However, after the protrusion the pure erosion metal loss increased slightly due to disturbed flow. The sum of the erosion rate and the corrosion rate agreed with the measured erosion/corrosion rate within the margin of error (Figure 95). This means that there was no synergistic effect in the erosion-corrosion process when the system had 2 wt.% sand. This conclusion is in accordance with previous work done in a similar setup[156] .

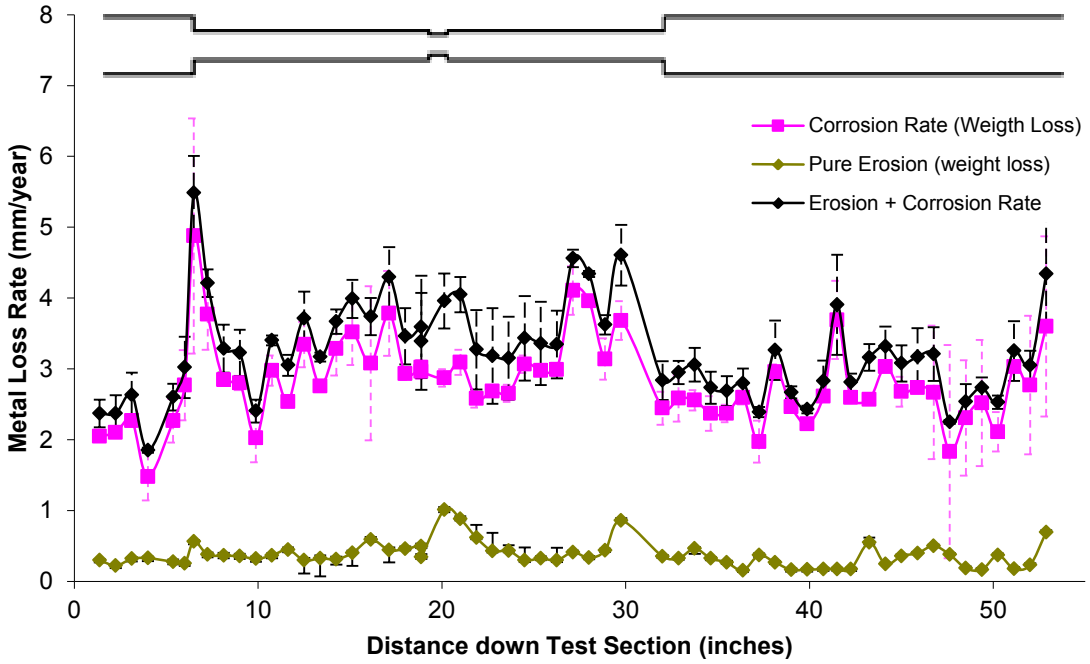

Figure 94. Combined analysis, corrosion rate (pH 5.0, 0 wt.% sand), erosion rate (pH 7.0, 2wt.% sand) and erosion + corrosion rate (25ºC, velocity 2 m/s and 0.98 bar CO_2)

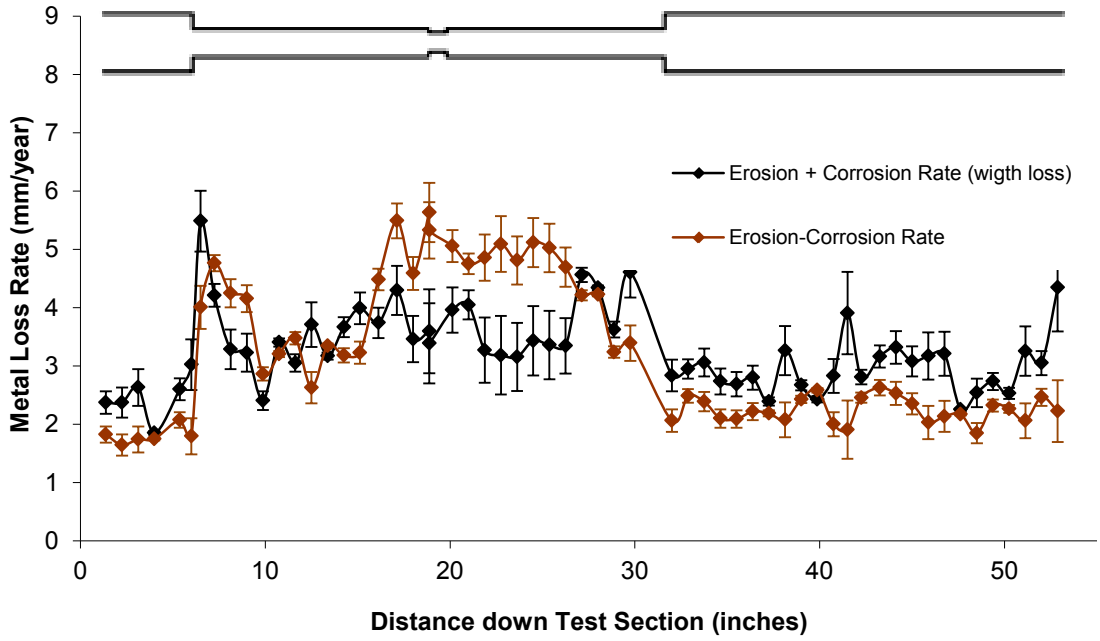

Figure 95. Comparison between the sum corrosion rate (pH 5.0, 0 wt.% sand) + erosion rate (pH 7.0, 2wt.% sand) and erosion/corrosion rate (25ºC, velocity 2 m/s and 0.98 bar CO_2)

Results at 2 wt.% sand and 20 ppm of inhibitor:

Figure 96 shows the influence of 20 ppm of corrosion inhibitor. The addition of inhibitor decreases the weight loss corrosion rate from 2 mm/year to 0.5 mm/year (75% efficiency) in the 4" ID pipe, and from 3.5 mm/year to 1 mm/year (71.4% efficiency) in a 2.5" ID pipe.

In Figure 97 the effect of the same concentration of corrosion inhibitor on the erosion process is observed. The erosion rate was reduced by the addition of 20 ppm of inhibitor from 0.3 mm/year to 0.1 mm/year (66% efficiency) in a 4" pipe diameter and from 1 mm/year to 0.2 mm/year (80% efficiency) after the protrusion. It is evident that the addition of inhibitor reduced the damage made by erosion process, since all the peaks

that appear in the erosion profile (20, 30, and 47 inches) were removed when the inhibitor was added.

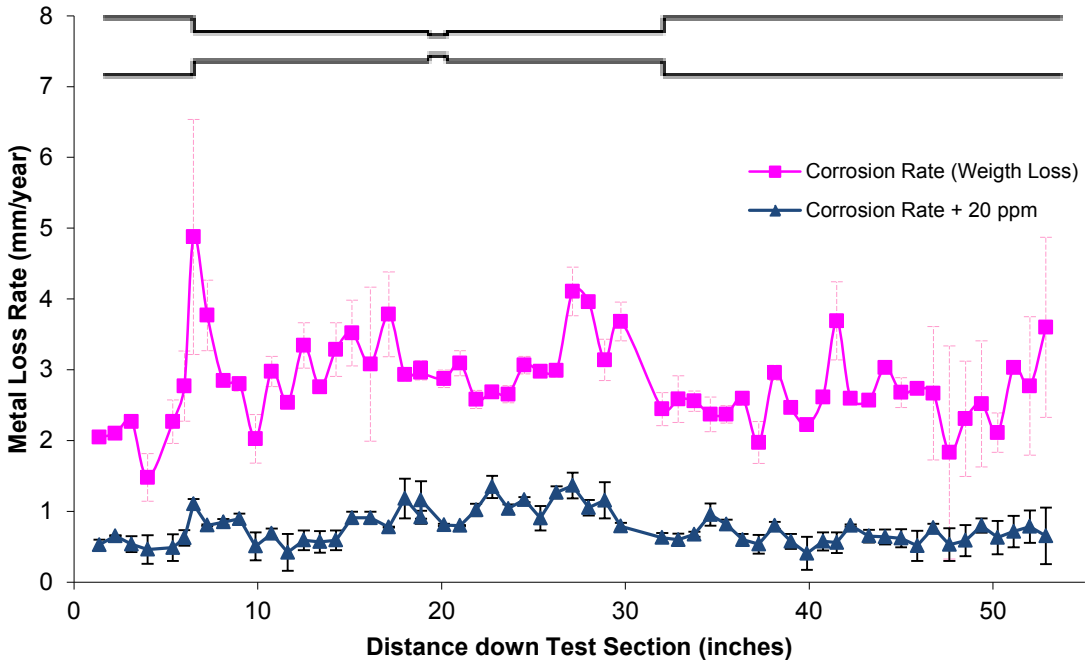

Figure 96. Corrosion rate and inhibited corrosion rate with 20ppm of inhibitor at pH 5.0, 0 wt.% sand, 25ºC, velocity 2 m/s and 0.98 bar CO_2.

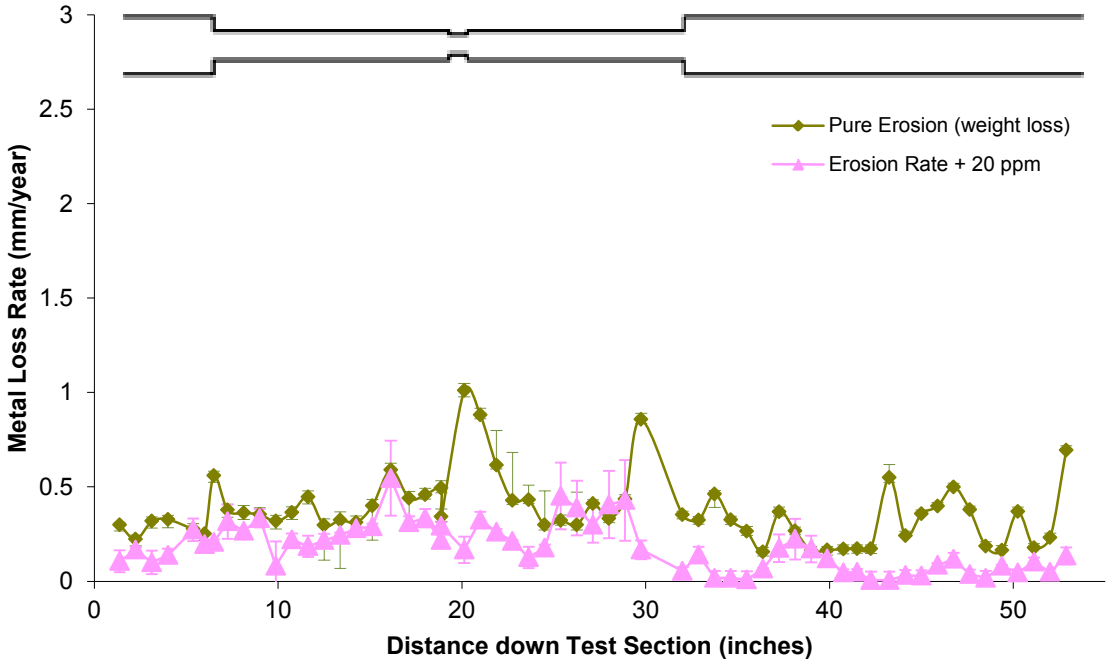

Figure 97. Erosion rate and inhibited erosion rate with 20ppm of inhibitor at pH 7.0, 2 wt.% sand, 25ºC, velocity 2 m/s and 0.98 bar CO_2.

Figure 98 shows a comparison between the combined metal loss from individual erosion and corrosion experiments and the metal loss due to the simultaneous erosion/corrosion process. In this graph it is possible to see that the sum of inhibited erosion and inhibited corrosion rate is very close to the inhibited erosion/corrosion rate.

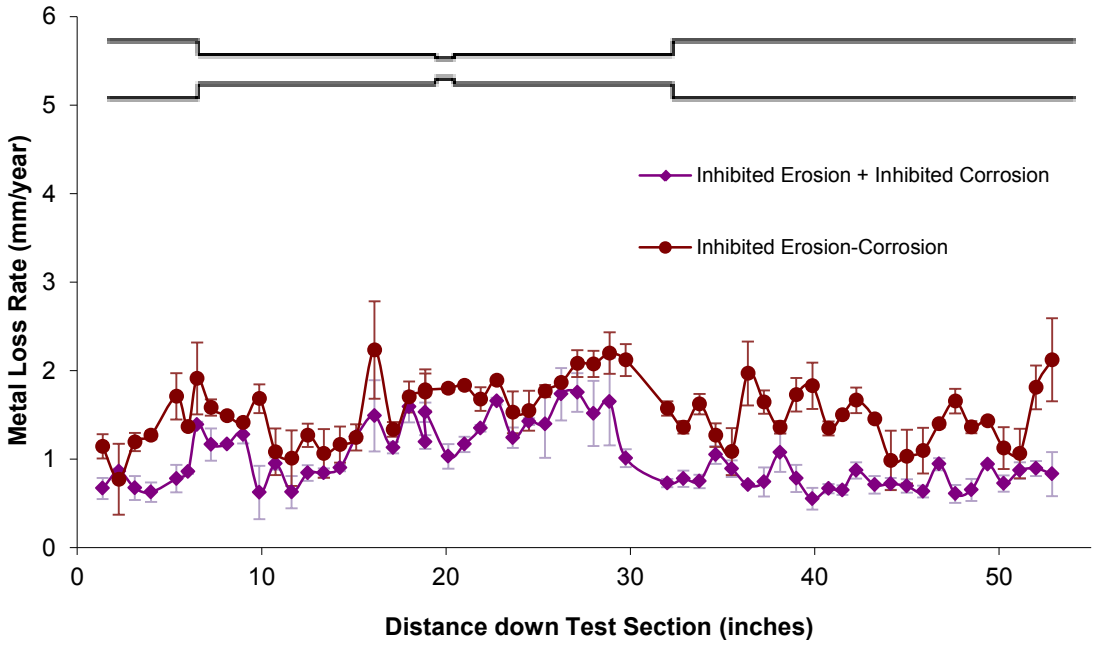

Figure 98 Comparison between the sum inhibited corrosion rate(pH 5.0, 0 wt.% sand) + inhibited erosion rate (pH 7.0, 2 wt.% sand) and inhibited erosion/corrosion rate (pH 5.0, 2 wt.% sand, 25ºC, velocity 2 m/s and 0.98 bar CO_2).

Figure 99 and Figure 100 show that the corrosion inhibitor was not lost due to selective adsorption onto sand. The corrosion rate (Figure 99) for inhibited corrosion and inhibited corrosion/erosion are 0.5 mm/year. Also, the corrosion potentials are in the same range: -0.675 to -0.665 V (see Figure 100).

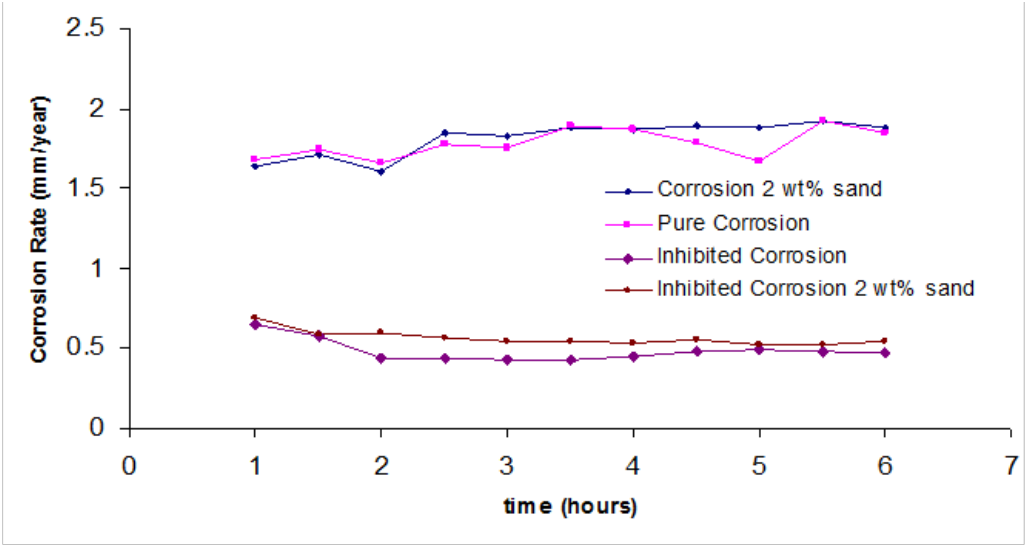

Figure 99. Corrosion rate measured with RCE for 20ppm of corrosion inhibitor with and without 2 wt.% sand (pH 5.0, 25ºC, 3200rpm and 0.98 bar CO_2).

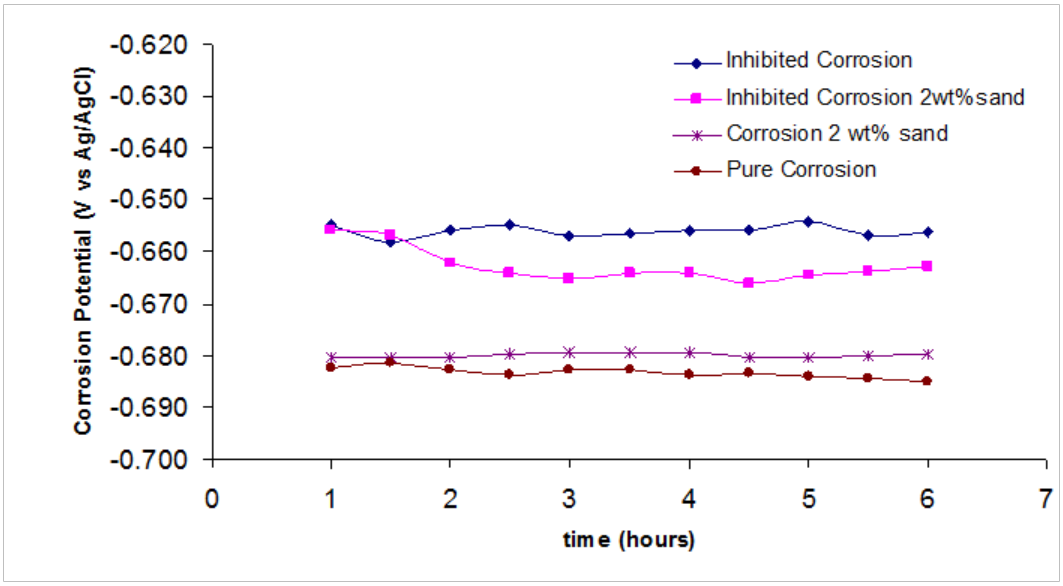

Figure 100. Corrosion potential measured with RCE for 20ppm of corrosion inhibitor with and without 2 wt% sand (pH 5.0, 25ºC, 3200rpm and 0.98 bar CO_2).

Results at 2 wt% sand and 50 ppm of inhibitor:

Figure 101 shows that 50 ppm of inhibitor offers good protection against pure corrosion, reducing the metal loss rate from ~2 mm/year to ~ 0.13 mm/year (93.5% efficiency) in a 4" ID pipe and from ~3 mm/year to ~0.25 mm/year (91.6% efficiency) in a 2.5" ID pipe. Comparing the erosion/corrosion experiment with 50 ppm of inhibitor to the pure erosion experiment (Figure 94), it is observable in Figure 102 that the inhibitor film also protected the steel against the sand erosion process, as happened with 20 ppm of inhibitor. All the peaks due to the sand impingement were reduced.

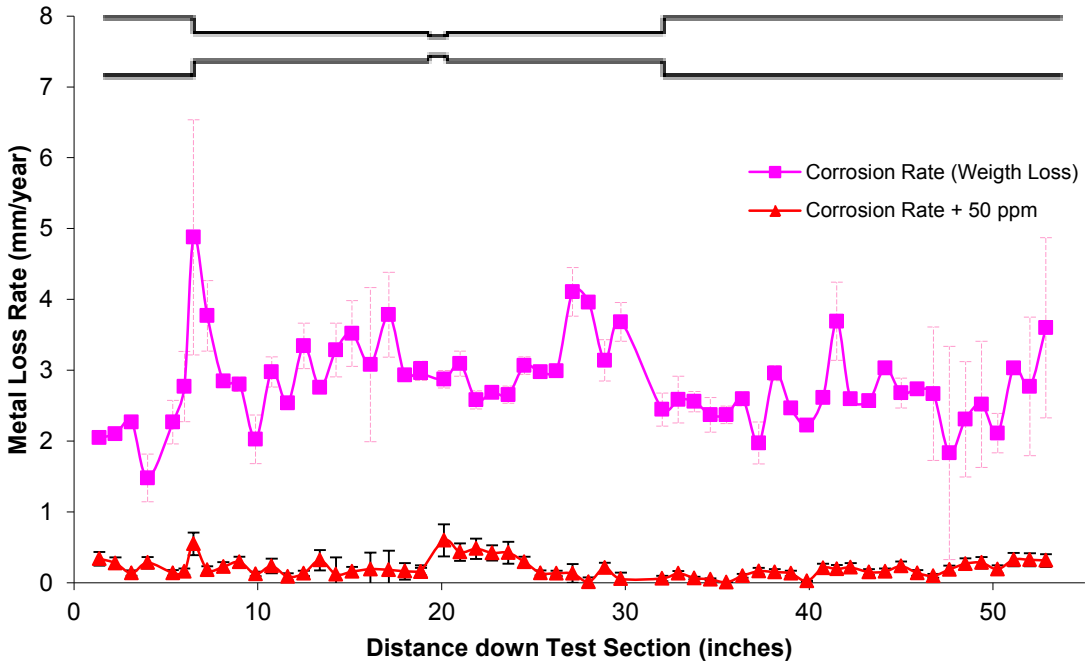

Figure 101. Corrosion rate and inhibited corrosion rate with 50 ppm of inhibitor at pH 5.0, 25ºC, 0 wt.% sand, velocity 2 m/s and 0.98 bar CO_2.

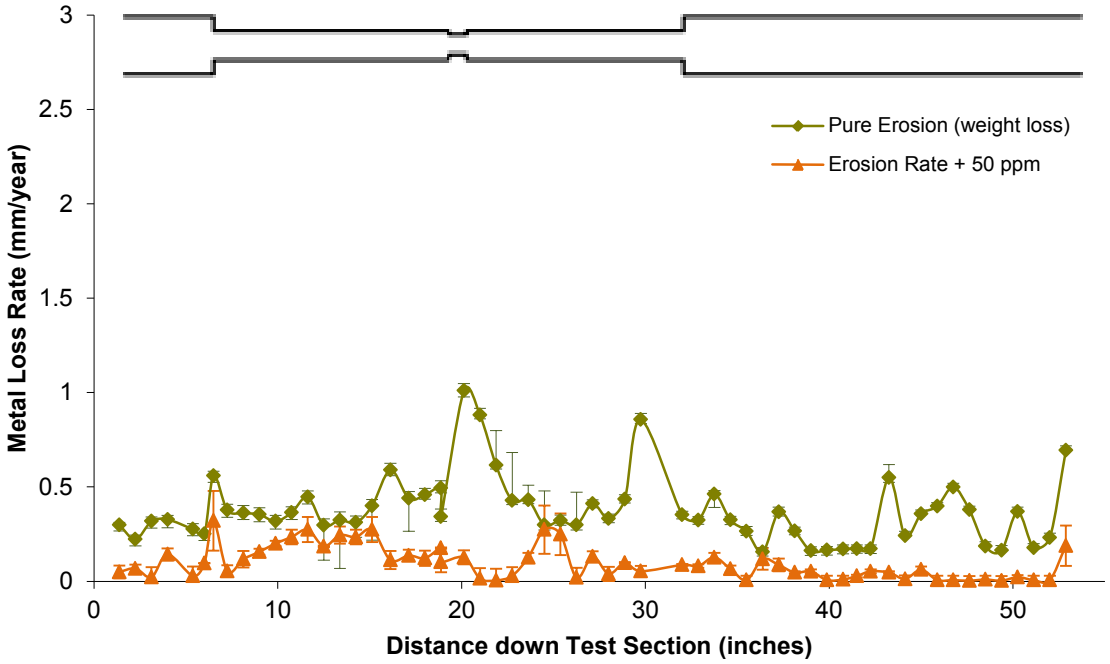

Figure 102. Erosion rate and inhibited erosion rate with 50ppm of inhibitor at pH 7.0, 25ºC, 2 wt.% sand, velocity 2 m/s and 0.98 bar CO_2.

Figure 103 shows the comparison between the combined inhibited erosion rate plus inhibited corrosion rate with the erosion/corrosion rate. Good agreement is obtained as with 2% sand indicating no synergistic effect.

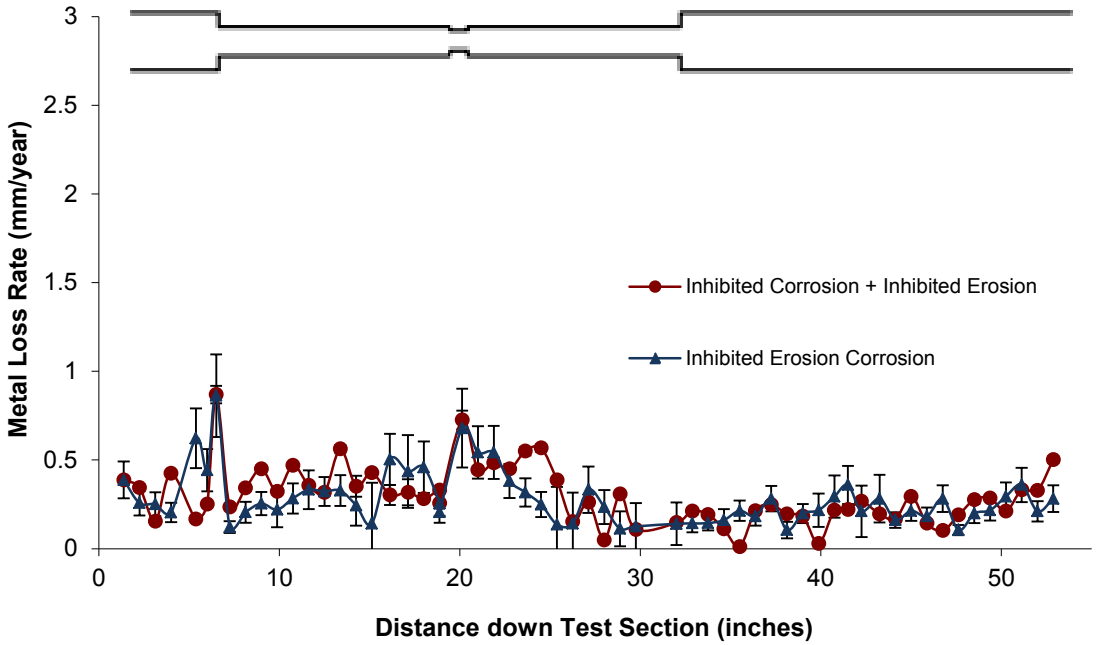

Figure 103. Comparison between the sum of inhibited corrosion rate(pH 5.0, 0 wt.% sand) plus inhibited erosion rate (pH 7.0, 2 wt.% sand) and inhibited erosion/corrosion rate (pH 5.0, 2 wt.% sand) at 25ºC, velocity 2 m/s and 0.98 bar CO_2.

Figure 104 and Figure 105 confirmed that the corrosion inhibitor was not lost due to selective adsorption onto sand.

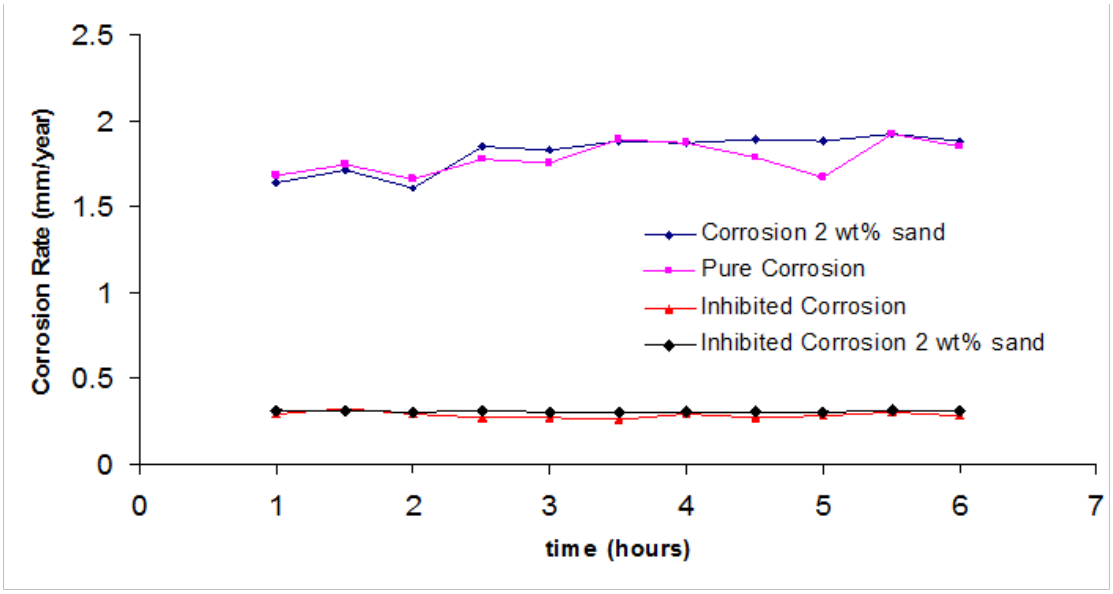

Figure 104. Corrosion rate measured with RCE for 50 ppm of corrosion inhibitor with and without 2 wt.% sand (pH 5.0, 25ºC, 3200rpm and 0.98 bar CO_2).

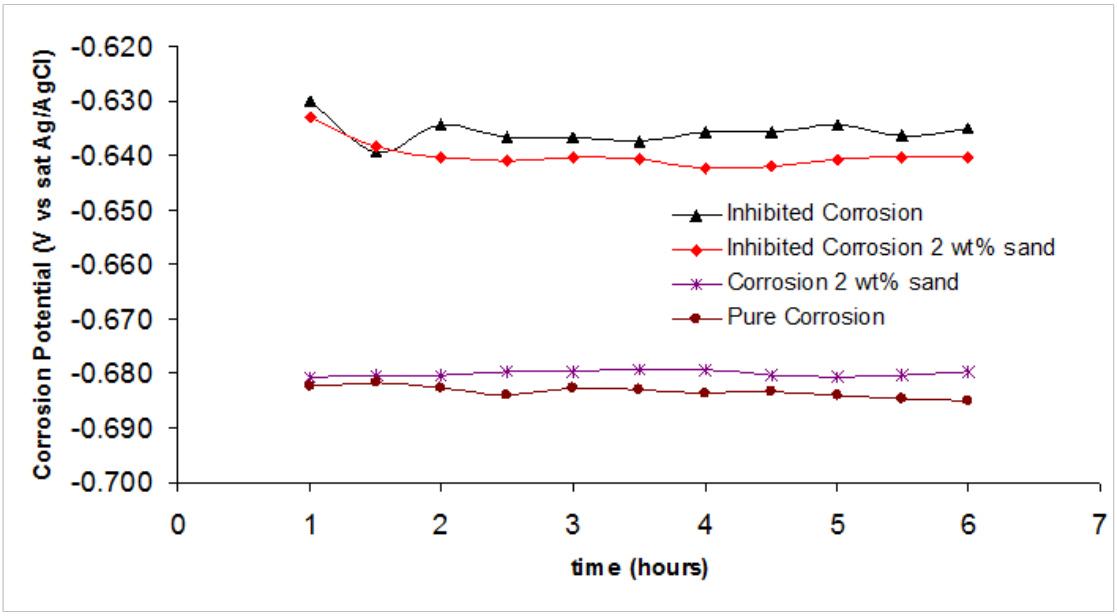

Figure 105. Corrosion potential measured with RCE for 20ppm of corrosion inhibitor with and without 2 wt% sand (pH 5.0, 25ºC, 3200rpm and 0.98 bar CO_2).

Chapter 7. Conclusions

- The adsorption of the organic corrosion inhibitors could be described by the Langmuir adsorption isotherms. The interaction energies between the organic molecules and the steel surface are in the range of physisorption for inhibitor alkyl benzyl dimethyl ammonium chloride K2 (-21 kJ/mol) and between a physisorption and chemisorption energies for inhibitor TOFA/DETA Imidazolinium (K1) (-30 kJ/mol). Corrosion inhibitor Sodium thiosulfate (K3), which is not a surfactant, appears to follow the same Langmuir isotherm with a binding energy in the chemisorption region -36 kJ/mol.
- Blending organic inhibitor (TOFA/DETA Imidazolinium and alkyl benzyl dimethyl ammonium chloride with sodium thiosulfate) showed a positive effect superior to that of single organic compounds. The electrochemical results showed that the organic corrosion inhibitors tested work by blocking the active sites on the steel surface. The improvement in performance of TOFA/DETA Imidazolinium and alkyl benzyl dimethyl ammonium chloride when blended with sodium thiosulfate suggest that inhibitor K3 forms a thin film of iron sulfide at the sites that are not covered by organic molecules.
- The effect of wall shear stress on the performance of the tested corrosion inhibitors was evaluated in small and large scale in single liquid phase flow and in multiphase flow. The different techniques (RCE, liquid jet impingement, CO_2 bubble jet impingement vapor cavitation, erosion-corrosion, moving slug and standing slug) used to develop high wall shear stress were not enough to disrupt

the corrosion inhibitor film. The opposite was observed: the corrosion inhibitors performance was improved. Even corrosion inhibitor with lower binding energy with steel (alkyl benzyl dimethyl ammonium chloride) was not affected by the wall shear stress at the concentrations tested.

- The major reduction of organic corrosion inhibitor performance in multiphase flow was encountered as a result of the consumption of corrosion inhibitor due to foaming at the gas/liquid interphase. The addition of sodium thiosulfate to inhibitors TOFA/DETA Imidazolinium and alkyl benzyl dimethyl ammonium chloride helped to improve their performance under foaming conditions.
- Even in very aggressive solid/liquid multiphase flow, erosion-corrosion had no effect on the corrosion inhibitor film performance. The corrosion inhibitor film was able to reduce the corrosion rate and even diminish somewhat the damage by erosion.

Chapter 8. Future Work

Based on the experimental results, significant gaps exist that can be addressed in order to further understanding of the effect of mechanical forces on corrosion inhibitor film performance.

Advancing theories of inhibitor adsorption and understanding the role of temperature will be important in modeling adsorption processes. Evaluation of the effect of wall shear stress on corrosion inhibitor film performance when the system is at higher temperatures will help to determine under which operational circumstances the wall shear stress affects adsorption, or if the wall shear stress does not play any role in the desorption process of corrosion inhibitors.

More different corrosion inhibitors should be further investigated, both for sweet (CO_2) and sour (H_2S) systems. The inhibitors evaluated in this work were generic and are used as a common component, in both sweet or sour systems. Exploration of the effect of wall shear stress on corrosion inhibitor film performance in sour systems will help to elucidate how wall shear stress affects the performance of corrosion inhibitor in the presence of a sulfide film. In addition, a future goal should be explore how sodium thiosulfate, added as an “activator” in inhibitor blends, impacts the protectiveness of the film under high wall shear stress.

This work aimed to advance the understanding of the effect of wall shear stress on corrosion inhibitor film performance. Surface analysis techniques such as TEM, AFM and XPS can help in the development of the understanding of the bonding interactions between corrosion inhibitor moleculaes and the metallic surface. In this way a better

understanding of the effect of mechanical forces on corrosion inhibitor film performance can be reached.

Bibliography

1. Nesic, S. & Lee, L. A Mechanistic Model for CO2 Corrosion with Protective Iron Carbonate Films-Part 3: Film Growth Model. *Corrosion* **59,** 616–628 (2003).

2. Fajardo, V., Canto, C., Brown, B. & Nesic, S. Effect of Organic Acids in CO2 Corrosion. in *CORROSION/07* paper No. 07319 (NACE International, 2007).

3. Bockris, J., Drazic, D. & Despic, A. The Electrode Kinetics of the Deposition and Dissolution of Iron. *Electrochem. Acta* **4,** 325–361 (1961).

4. Dugstad, A. Mechanism of Protective Film Formation During CO2 Corrosion of Carbon Steel. in *CORROSION/98* paper No. 31 (NACE International, 1998).

5. Nesic, S. & Lunde, L. Carbon Dioxide Corrosion of Carbon Steel in Two-Phase Flow. *Corrosion* **54,** 717–727 (1994).

6. Gulbrandsen, E., Nyborg, R., Loland, T. & Nisancioglu, K. Effect of Steel Microstructure and Composition on Inhibition of CO2 Corrosion. in *CORROSION/00* paper No. 23 (NACE International, 2000).

7. Binks, B., Fletcher, D. & Salama, I. Quantitative Prediction of the Reduction of Corrosion Inhibitor Effecteviness due to Parasitic Adsorption Onto a Competitor Surface. *Langmuir* **27,** 469–473 (2010).

8. Nesic, S., Postlethwaite, J. & Olsen, S. An Electrochemical Model for Prediction of Corrosion of Mild Steel in Aqueous Carbon Dioxide Solutions. *Corrosion* **52,** 280–294 (1996).

9. De Waard, C. & Lotz, U. Prediction of CO2 Corrosion of Carbon Steel. in *CORROSION/93* paper No. 69 (NACE International, 1993).

10. Nesic, S., Nordsveen, M. & Nyborg, R. A Mechanistic Model for Carbon Dioxide Corrosion of Mild Steel in the Presence of Protective Iron Carbonate Films-Part 2: A Numerical Experiment. *Corrosion* **59,** 489–497 (2003).

11. Nordsveen, M., Nesic, S. & Nyborg, R. A Mechanistic Model for Carbon Dioxide Corrosion of Mild Steel in the Presence of Protective Iron Carbonate Films - Part 1: Theory and Verification. *Corrosion* **59,** (2003).

12. De Waard, C., Lotz, U. & Milliams, D. Predictive Model for CO2 Corrosion Engineering in Wet Natural Gas Pipelines. *Corrosion* **47,** 976–985 (1991).

13. Nestle, A. Corrosion Inhibitors in Petroleum Production Primary Recovery. (1973).

14. Gray, L., Anderson, B., Danysh, M. & Tremaine, D. Effect of pH and Temperature on the Mechanism of Carbon Steel Corrosion by Aqueous Carbon Dioxide. in *CORROSION/90* paper No. 40 (NACE International, 1990).

15. Sastri, V. *Corrosion Inhibitors : Principles and Applications*. (Wiley, 1998).

16. Sastri, V. & Perumareddi, J. Molecular Orbital Theoretical Studies of some Organic Corrosion Inhibitors. *Corrosion* **53,** 617–622 (1997).

17. Xiong-Ci, Y., Hong, Z. & Ming-Dao, L. Quantum Chemical Study of Inhibition Properties of Pyridine and its Derivatives at an Aluminum Surface. *Corros. Sci.* **42,** 645–653 (2000).

18. Shawn, D. *Colloid and Surface Chemistry*. (Butterworth Heinemann, 1992).

19. Moon, T. & Horsup, D. Relating Corrosion Inhibitor Surface Active Properties to Field Performance Requirements. in *CORROSION/02* paper No. 02298 (NACE International, 2002).

20. Moulik, S. Micelles: Self Organized Surfactants Assemblies. *Curr. Sci.* **71,** 368–376 (1996).

21. Goyal, P. S. & Aswal, V. K. Micellar Structure and Inter-Micelle Interactions in Micellar Solutions: Results of Small Angle Neutron Scattering Studies. *Curr. Sci.* **80,** 972–929 (2001).

22. Knag, M., Sjoblom, J., Oye, G. & Gulbrandsen, E. A Quartz Crystal Microbalance Study of the Adsorption of Quaternary Ammonium Derivates on Iron and Cementite. *Colloid Surf. Physicochem. Eng. Asp.* **250,** 269–278 (2004).

23. Brown, G., Grieger, P. & Kraus, C. Effect of Addition Agents on the Conductance of Long Chain Salts. *Prop. Electrolytic Solut.* **36,** 95–101 (1949).

24. Benalla, H. & Zajac, J. Effect of Alcohol Addition to the Aqueous Phase on the Thermal Effects of Micellization of Cationic Benzyldimethyldodecylammonium Bromide and its Adsorption Onto Porous and Nonporous Silicas. *J. Colloid Interface Sci.* **272,** 253–261 (2004).

25. Ramachandran, S., Tsai, B. & Blanco, M. Self-Assembled Monolayer Mechanism for Corrosion Inhibition of Iron by Imidazolines. *Langmuir* **12,** 6419–6428 (1996).

26. Ramachandran, S. & Jovancicevic, V. Molecular Modeling of the Inhibition of Mild Steel Carbon Dioxide Corrosion by Imidazolines. *Corrosion* **55,** 259–267 (1999).

27. Ramachandran, S., Tsai, B. & Blanco, M. Atomistic Simulations of Oleic Imidazolines Bound to Ferric Clusters. *J. Phys. Chem. Acta* **101,** 83–89 (1997).

28. Nasser, A. & Sathiq, M. Adsorption and Corrosion Inhibition of Mild Steel in Hydrochloric Acid Medium by N-[Morpholin-4-YL(Phenyl)Methyl]Benzamide. *Int. J. Eng. Sci. Technol.* **2,** 6417–6426 (2010).

29. Liu, X., Okafor, P. & Zheng, Y. The Inhibition of CO2 Corrosion of N80 Mild Steel in Single Liquid Phase and Liquid/Particle Two-Phase Flow by Aminoethyl Imidazoline Derivatives. *Corros. Sci.* **51,** 74751 (2009).

30. Likhanova, N., Dominguez-Aguilar, M. & Olivares-Xometl, O. The Effect of Ionic Liquids with Imidazolium and Pyridinium Cations on the Corrosion Inhibition of Mild Steel in Acidic Environments. *Corros. Sci.* **52,** 2088–2097 (2010).

31. Palomar, M., Olivares-Xometl, O. & Likhanova, N. Imidazolium, Pyridinium and Dimethyl-Ethylbenzyl Ammonium Derived Compounds as Mixed Corrosion Inhibitors in Acidic Medium. *J. Surfactants Deterg.* **14,** 211–220 (2011).

32. Liu, J., Yu, W. & Zhang, J. Molecular Modeling Study on Inhibition Performnace of Imidazolines for Mild Steel in CO2 Corrosion. *Appl. Surf. Sci.* **256,** 4729–4733 (2010).

33. Bajpai, D. & Tyagi, V. Synthesis and Characterization of Imidazolinium Surfactants Derived from Tallow Fatty Acids and Diethylenetrimine. *Eur J Lipid Sci Technol.* **110,** 935–940 (2008).

34. Jovancicevic, V., Ramachandran, S. & Prince, P. Inhibition of Carbon Dioxide Corrosion of Mild Steel by Imidazolines and their Precursors. *Corrosion* **55,** 449–455 (1999).

35. Zhang, X., Wang, F. & He, y. Study of the Inhibition Mechanism of Imidazoline Amine on CO2 Corrosion of Armco Iron. *Corros. Sci.* **43,** 211–220 (2011).

36. Zhao, J. & Chen, G. The Synergistic Effect of Oleic Based Imidazoline and Sodium Benzoate on Mild Steel Corrosion in a CO2-Saturated Brine Solution. *Electrochem. Acta* **69,** 247–255.

37. Bereket, G. & Yurt, A. Inhibition of the Corrosion of Low Carbon Steel in Acidic Solution by Selected Quaternary Ammonium Compounds. *Anti-Corros. Methods Mater.* **49,** 210–220 (2002).

38. Fuchs-Godec, R. The Adsorption CMC Determination and Corrosion Inhibition of some N-Alkyl Quaternary Ammonium Salts on Carbon Steel Surface in 2 M H2SO4. *Colloid Surf.* **280,** 130–139 (2006).

39. Zvuaya, R. & Dawson, J. L. Inhibition Studies in Sweet Corrosion Systems by a Quaternary Ammonum Compound. *J. Appl. Electrochem.* **24,** 943–947 (1994).

40. Ezuber, H. Influence of Temperature and Thiosulfate on the Corrosion Behavior of Steel in Chloride Solutions Saturated in CO2. *Mater. Des.* **30,** 3420–3427 (2009).

41. Oblonsky, L., Chesnut, G. & Devine, T. Adsorption of Octadecyldimethylbenzylammonium Chloride to Two Carbon Steel Microstructures as Observed with Surface-Enhanced Raman Spectroscopy. *Corros. Sci.* **51,** 891–900 (1995).

42. Dendramis, A., Schwinn, E. & Sperline, R. A Surface-Enhance Raman Scattering Study of CATB Adsorption on Copper. *Surf. Sci.* **134,** 675–688 (1983).

43. Free, M. Understanding the Effect of Surfactant Agregation on Corrosion Inhibition of Mild Steel in Acidic Medium. *Corros. Sci.* **44,** 2865–2870 (2002).

44. Malik, H. Influence of C16 Quaternary Amine on Surface Films and Polarization Resistance of Mild Steel in Carbon Dioxide-Saturated 5% Sodium Chloride. *Corros. Eng. Ssection* **51,** 321–328 (1995).

45. Malik, H. Effect of pH on the Corrosion Inhibition of Mild Steel in CO2 Saturated Brine Solution. *Anti-Corros. Methods Mater.* **47,** 88–93 (2000).

46. Malik, H. Charge and pH Effects on Inhibitor Performance. *Anti-Corros. Methods Mater.* **48,** 364–370 (2001).

47. Hausler, R. *Performance of 'Quat' Type Inhibitor at Hig pH*.

48. Hausler, R. & Schmitt, G. Hydrodynamic and Flow Effects on Corrosion Inhibition. in *CORROSION/04* paper No. 04402 (NACE International, 2004).

49. Horsup, D., Clark, J., Binks, B., Fletcher, D. & Hicks, J. I Put it in, but where does it go? - The Fate of Corrosion Inhibitors in Multiphase Systems. in *CORROSION/07* paper No. 7617 (NACE International, 2007).

50. Gulbrandsen, E., Kvarekval, J. & Miland, H. Effect of Oxygen Contamination on Inhibition Studies in Carbon Dioxide Corrosion. *Corrosion* **61,** 1086–1097 (2011).

51. Jovancicevic, V., Dougherty, J. & Alink, B. CO2 Corrosion Inhibition by Sulfur-Containing Organic Compounds. in *CORROSION/00* paper No. 007 (NACE International, 2000).

52. Phillips, J., Renwick, J., Palmer, J. & Swift, A. The Synergistic Effect of Sodium Thiosulfate on Corrosion Inhibition - Oil Field Chemicals. in (1996).

53. Kappes, M. Evaluation of Thiosulfate as a Substitute for Hydrogen Sulfide in Sour Corrosion Fatigue Studies. (Ohio State University, 2011).

54. Kappes, M., Frankel, G. & Sridhar, N. Reaction Paths of Thiosulfate during Corrosion of Carbon Steel in Acidified Brines. *J. Electrochem. Soc.* **159,** C195–C204 (2012).

55. Kappes, M., Frankel, G. & Sridhar, N. Corrosion Behavior of Carbon Steel in Acidified, Thiosulfate-Containing Brines. *Corros. Sci.* **68,** 872–884 (2012).

56. Marcus, P. & Protopopof, E. Thermodynamics of Thiosulfate Reduction on Surfaces of Iron, Ninckel and Chromium in Water at 25 and 300°C. *Corros. Sci.* **39,** 1741–1752 (1997).

57. Pou, T. & Crolet, J. . Sensitivity of Oilfield Corrosion Inhibitors to Traces of Thiosulfate. in 1239–1249 (SEIC, 1995).

58. Chesnut, G. & Choi, H. Laboratory Testing and Selection of Corrosion Inhibitors for Continuos Application in Multiphase Pipelines. in *CORROSION/94* paper No. 35 (NACE International, 1994).

59. Nesic, S. Key Issues Related to Modeling of Internal Corrosion of Oil and Gas Pipelines - A Review. *Corros. Sci.* **49,** 4308–4338 (2007).

60. Gulbrandsen, E. & Grana, A. Testing of Carbon Dioxide Corrosion Inhibitor Performance at High Flow Velocities in Jet Impingement Geometry. Effect of Mass Transfer and Flow Forces. *Corrosion* **63,** 1009–1020 (2007).

61. Dougherty, J. & Stegmann, D. The Effects of Flow on Corrosion Inhibitor Performance. *Mater. Perform.* **35,** 47–53 (1996).

62. Woods, B., Fan, Z. & Hanratty, T. Frequency and Development of Slugs in a Horizontal Pipe at Large Liquid Flows. *Int J Multiph. Flow* **32,** 902–925 (2006).

63. Green, A. ., Johnson, B. . & Chol, H. . Flow-Related Corrosion in Large-Diameter Multiphase Flowlines. *SPE Prod. Facil.* **8,** 97–100 (1993).

64. Villarreal, J., Laverde, D. & Fuentes, C. Carbon-Steel Corrosion in Multiphase Slug Flow and CO2. *Corros. Sci.* **48,** 2363–2379 (2006).

65. Schmitt, G. Drag Reduction by Corrosion Inhibitors - A Neglected Option for Mitigation of Flow Induced Localized Corrosion. *Mater. Corros.* **52,** 329–343 (2001).

66. Seal, S., Sapre, K. & Kale, A. Effect of Multiphase Flow on Corrosion of C-Steel in Presence of Inhibitor: A Surface Morphological and Chemical Study. *Corros. Sci.* **42,** 1623–1634 (2000).

67. Nesic, S., Langsholt, M. & Lunde, L. *The Effect of Multiphase Flow on C O2 Corrosion and its Inhibition, Phase I - Measurments of Wall Shear Stress and Mass Transfer in Two-Phase Gas/Liquid Flow*. (IFE, 1995).

68. Heeg, B. & Klenerman, D. Persistency of Corrosion Inhibitor Films on C-Steel Under Multiphase Flow Conditions. Part II: Optical SHG and Electrochemical Studies. *Corros. Sci.* **40,** 1313–1329 (1998).

69. Heeg, B., Moros, T. & Klenerman, D. Persistency of Corrosion Inhibitor Films on C-Steel Under Multiphase Flow Conditions. Part I: The Jet-Cylinder Arragement. *Corros. Sci.* **40,** 1303–1311 (1998).

70. Petersen, A., Klenerman, D. & Hedges, W. Evaluation of the Effect of Carbon Dioxide Corrosion Inhibitors on Cavitation Damage Caused during the Ultrasound Test. *Corros. Sci.* **60,** 187–194 (2004).

71. Petersen, A., Klenerman, D. & Hedges, W. Effect of Cavitation on Carbon Dioxide Corrosion and the Development of a Test for Evaluating Inhibitors. *Corrosion* **58,** 216–224 (2002).

72. Efird, K. Jet Impingement Testing for Flow Accelerated Corrosion. in *CORROSION/00* paper No 00052 (NACE International, 2000).

73. Efird, K. Disturbed Flow and Flow-Accelerated Corrosion in Oil and Gas Production. *J. Energy Resour. Technol.* **120,** 72–77 (1998).

74. Silverman, D. The Rotating Cylinder Electrode for Examining Velocity-Sensitive Corrosion- A REview. *Corrosion* **60,** 1003–1023 (2004).

75. Nesic, S., Solvi, T. & Skjerve, S. Comparison of Rotating Cylinder and Loop Methods for Testing CO2 Corrosion Inhibitors. *Br. Corros. J.* **32,** 269–276 (1997).

76. Nesic, S., Solvi, T. & Skjerve, S. Rotating Cylinder vs. Loop Testing of Inhibitors for CO2 Corrosion. in *Proceedings of the 8th European Symposium on Corrosion Inhibitors* 1135–1162 (Ann. Univ. Ferrara, 1995).

77. Eisenberg, M., Tobias, C. . & Wilke, C. Ionic Mass Transfer and Concentration Polarization at Rotating Electrode. *J. Electrochem. Soc.* **101,** 306–320 (1954).

78. Patel, V. . & Head, M. Some Observations on Skin Friction and Velocity Profiles in Fully Developed Pipe and Channel Flow. *J. Fluid Mech.* **38,** 181–201 (1969).

79. Woollam, R. Is Shear Stress Important in CI Performance? Lenght Scales Important to Understanding Corrosion Processes. in *CORROSION/07* paper no.STG 61/EFC WP 13 Joint Session (NACE International, 2007).

80. Menendez, C., Weghorn, S., Ahn, Y., Jenkins, A. & Mok, W. Electrochemical Evaluations of High Shear Corrosion Inhibitors Using Jet Impingment. in *CORROSION/05* paper No 05331 (NACE International, 2005).

81. Zheng, L., Zhang, G., Guo, X. & Chai, C. Inhibitor Effect of Thioureidoimidazoline Inhibitor for the Flow Accelerated Corrosion of an Elbow. *Corros. Sci.* **90,** 202–215 (2015).

82. Schmitt, G., Bakalli, M. & Horstemeier, M. Contribution of Drag Reduction to the Performance of Corrosion Inhibitors in One-and two-Phase Flow. in *CORROSION/07* paper No 05344 (NACE International, 2007).

83. Tajallipour, N., Zhu, Z. & Teevens, P. The Effect of Slug Liquid Front on Inhibitor Effectiveness in Petroleum Pipelines. in *CORROSION/11* paper No 11275 (NACE International, 2011).

84. Tan, Y., Bailey, S. & Kinsella, B. An Investigation of the Formation and Destruction of Corrosion Inhibitor Films using Electrochemical Impedance Spectroscopy (EIS). *Corros. Sci.* **38,** 1545–1561 (1996).

85. McMahon, A., Martin, J. & Harris, L. Effects of Sand and Interfacial Adsorption Loss on Corrosion Inhibitor Efficiency. in *CORROSION/05* paper No 05274 (NACE International, 2005).

86. Shadley, J., Shirazi, S., Dayalan, E. & Rybicki, E. Using an Inhibitor to Combat Erosion-Corrosion in Carbon Steel Piping - How Much does it Help? in *Offshore Technology Conference* paper No. OTC 8195 (Offshore Technology Conference, 1996).

87. Tummala, K., Roberts, K., Shadley, J. & Rincon, H. Effect of Sand Production and Flow Velocity on Corrosion Inhibition Under Scale Forming Conditions. in *CORROsION/09* paper No 09474 (NACE International, 2009).

88. Wang, C. & Neville, A. Alleviation of Erosion-Corrosion Damage by Liquid-Sand Impact Trough use of Chemicals. *Wear* **258,** 649–658 (2005).

89. McLaury, B. & Shirazi, S. An Alternate Method to API RP 14E for Predicting Solids Erosion in Multiphase Flow. *J. Energy Resour. Technol.* **122,** 115–122 (2000).

90. McLaury, B., Wang, J., Shirazi, S., Shadley, J. & Rybicki, E. Solid Particle Erosion in Long Radius Elbows and Straight Pipes. in paper No 38842 (1997).

91. Wang, S. & Nesic, S. *On Coupling CO2 Corrosion and Multiphase Flow Models*. (Ohio University - ICMT, 2002).

92. Wang, H., Hong, T., Cai, J. & Jepson, W. Enhanced Mass Transfer and Wall Shear Stress in Multiphase Slug Flow. in *CORROSION/02* paper No 02501 (NACE International, 2002).

93. Schmitt, G. & Mueller, M. Critical Wall Shear Stresses in CO2 Corrosion of Carbon Steel. in *CORROSION/99* paper No 44 (NACE International, 1999).

94. Maley, L. & Jepson, W. Liquid Holdup in Large-Diameter Horizontal Multiphase Pipelines. *J. Energy Resour. Technol.* **120,** 185–192 (1998).

95. Bonizzi, M. & Issa, R. A Model for Simulating Gas Bubble Entrainment in Two Phase Horizontal Slug Flow. *Int. J. Multiph. Flow* **29,** 1685–1717 (2003).

96. Hewitt, G. & Hall-Taylor, N. *Annular Two-Phase Flow*. (Pergamon Press, 1970).

97. Maley, L. & Jepson, W. Wall Shear Stress and Differential Pressure in Large-Diameter Horizontal Multiphase Pipelines. *J. Energy Resour. Technol.* **122,** 193–197 (2000).

98. Li, W. *Effect of Multiphase Flow on Corrosion: Wall Shear Stress Measurements in Gas-Liquid*. (Ohio University, 2012).

99. Schmitt, G., Bosch, C. & Siegmund, G. A Probabilistic Model for Flow Induced Localized Corrosion. in *CORROSION/00* paper No 00049 (NACE International, 2000).

100. Chia, C., Giralt, F. & Trass, O. Mass Transfer in Axisymmetric Turbulent Impinging Jets. *Ind Eng Chem Fundam* **16,** 28–35 (1997).

101. Giralt, F., Chia, C. & Trass, O. Characterization of the Impingement Region in an Axisymmetric Turbulent Jet. *Ind Eng Chem Fundam* **16,** 21–28 (1997).

102. Papavinasam, S., Revie, R. W., Panneerselvam, T. & Milan, B. Standards for Laboratory Evaluation of Oilfield Corrosion Inhibitors. *Mater. Perform.* **46,** 46–51 (2007).

103. Tu, C., V. & Wood, D., H. Wall Pressure and Shear Stress Measurements Beneath an Impinging Jet. *Exp. Therm. Fluid Sci.* **13,** 364–373 (1996).

104. Gerretsen, J. & Visser, A. Inhibitor Performance Under Liquid Droplet Impingement Conditions in CO2 - Containing Environment. *Corros. Sci.* **34,** 1299–310 (1993).

105. Phares, D., Smedley, G. & Flagan, R. The Wall Shear Stress Produced by the Normal Impingement of a Jet on a Flat Surface. *J. Fluid Mech.* **418,** 351–375 (2000).

106. Papavinasam, S., Revie, R. W., Attard, M. & Demoz, A. Inhibitor Selection for Internal Corrosion Control of Pipelines: 1. Laboratory Methodologies. in *CORROSION/99* paper No. 1 (NACE International, 1999).

107. Papavinasam, S., Doiron, A. & Revie, R. W. Effect of Rotating Cage Geometry on Flow Pattern and Corrosion Rate. in *CORROSION/03* paper No 03333 (NACE International, 2003).

108. Deslouis, C., Belghazi, A., Al-Janabi, T., Plegemann, P. & Schmitt, G. Quantifying Local Wall Shear Stresses in the Rotated Cage. in *CORROSIOn/04* paper No 04727 (NACE International, 2004).

109. Mahulkar, A., Bapat, P. & Pandit, A. Steam Bubble Cavitation. *AIChE J.* **54,** 1711–1724 (2008).

110. Ashassi-Sorkhabi, H. & Ghalebsaz-Jeddi, N. Effect of Ultrasonically Induced Cavitation on Inhibition Behavior of Polyethylene Glycol on Carbon Steel Corrrosion. *Ultrason. Sonochem.* **13,** 180–188 (2006).

111. Dijkink, R. & Ohl, C. Measurement of Cavitation Induced Wall Shear Stress. *Appl. Phys. Lett.* **93,** 254107–1 to 254107–3 (2008).

112. Bremond, N., Arora, M. & Dammer, S. Interaction of Cavitation Bubbles on a Wall. *Phys. Fluids* **18,** 121505–1 to 121505–10 (2006).

113. Maisonhaute, E., Prado, C. & White, P. Vurface Acoustic Cavitation Understood Via Nanosecond Electrochemistry. Part III: Shear Stress in Ultrasonic Cleaning. **9,** 297–303 (2002).

114. Joseph, D. Cavitation and the State of Stress in a Flowing Liquid - CAV2001 Fourth International Symposium on Cavitation. in *Fourth International Symposium on Cavitation-CAV 2001* 1–13 (2001).

115. Kato, H., Konno, A. & Maeda, M. Possibility of Quantitative Prediction of Cavitation Erosion without Model Test. *Trans. ASME* **118,** 582–588 (1996).

116. Chivate, M. & Pandit, A. Quantification of Cavitation Intensity in Fluid Bulk. *Ultrason. Sonochem.* **2,** S19–S25.

117. Langton, N. & Vaughan, P. Cavitation and the Ultrasonic Degradation of High Polymers. *Brit J Appl Phys* **13,** 478–482 (1962).

118. Sanada, T., Watanabe, M. & Shirote, M. Impact of High-Speed Steam-Droplet Spray on Solid Surface. *Fluid Dyn. Res.* **40,** 627–636 (2008).

119. Ashassi-Sorkhabi, H. & Asghari, E. Effect of Hydrodynamics Conditions on the Inhibition Performance of L-Methionine as a 'Green' Inhibitor. *Electrochem. Acta* **54,** 162–167 (2008).

120. Wang, C., Neville, A., Ramachandran, S. & Jovancicevic, V. Understanding the Action of Inhibitors in Mitigating Erosion-Corrosion in Impinging Flows. in *CORROSION/04* paper No 4658 (NACE International, 2004).

121. Eaton, P. & Sutton, G. The Effect of Flow on Inhibitor Film Life. in *CORROSION/94* paper No 30 (NACE International, 1994).

122. Park, N., Morello, L., Wong, J. & Maksoud, S. The Effect of Oxygenated Methanol on Corrosion in Sour Wet Gas Environments. in *CORROSION/07* paper No 07663 (NACE International, 2007).

123. Miller, R. Adsorption Kinetics of Surfactants from Micellar Solutions. *Colloid Polym. Sci* **259,** 1124–1128 (1981).

124. Qiao, W., Zheng, Z. & Shi, Q. Synthesis and Properties of a Series of CO2 Switchable Surfactants with Imidazoline Group. *J Surfact Deterg* **15,** 533–539 (2012).

125. Bosenberg, S., John, D., Becker, T., Bailey, S. & De Marco, R. Resolving the Structure of Carbon Dioxide Corrosion Inhibitors on Surfaces. in *Corrosion Control* paper 113 (Australian Corrosion Association Inc., 2007).

126. Ying, G. Fate, Behavior and Effects of Surfactants and their Degradation Products in the Environment. *Environ. Int.* **32,** 417–431 (2006).

127. Alaei, P., Binks, B., Fletcher, D., Salama, I. & Horsup, D. Surfactant Properties of Alkylbenzyldimethylammonium Chloride Oilfield Inhibitors. in *CORROSIO/13* paper No 02158 (NACE International, 2013).

128. Sun, W. & Nesic, S. A Mechanistic Model of H2S Corrosion of Mild Steel. in *CORROSION/07* paper No 57 (NACE International, 2007).

129. Xiong, Y. AFM studies of the Metallicity of Single-walled Carbon Nanotubes and Corrosion Inhibitor Adsorption. (Ohio University, 2011).

130. Xiong, Y., Brown, B., Kinsella, B., Nesic, S. & Pailleret, A. Atomic Force Microscopy Study of the Adsorption of Surfctant Corrosion Inhibitor. *Corrosion* **73,** 247–260 (2014).

131. Small, D. Lateral Chain Packing in Lipids and Membranes. *J. Lipid Res.* **25,** 1490–1500 (1984).

132. McMahon, A. The Mechanism of Action of an Oleic Imidazoline Based Corrosion Inhibitor for Oilfield Use. *Colloid Surf.* **59,** 187–205 (1991).

133. Ashassi-Sorkhabi, H. & Es'haghi, M. Corrosion Inhibition of Mild Steel in Acidic Media by [BMIm]Br Ionic Liquid. *Mater. Chem. Phys.* **114,** 267–271.

134. Ai, J. Z., Guo, X. P., Qu, J. E., Chen, Z. Y. & Zheng, J. Adsorption behavior and Synergistic Mechanism of Cationic Inhibitor and KI on the Galvanic Electrode. *Colloids Surf. A* **281,** 147–155 (2006).

135. Papavinasam, S. *Uhlig's Corrosion Handbook*. (John Wiley & Sons, 2000).

136. Trasatti, S. Work Function, Electronegativity, and Electrochemical Behaviour of Metals II Potential of Zero Charge and Electrochemical Work Functions. *J Electroanal Chem* **33,** 351–378 (1971).

137. Drazic, D., Vracar, L. & Drazic, V. The Kinetics of Inhibitor Adsorption on Iron. *Electrochem. Acta* **38,** 1165–1170 (1994).

138. Kern, P. & Landlot, D. Adsoption of a Bromide Labeled Carboxylic Acid Corrosion Inhibitor on Iron Measured with EQCM, EIS and XPS. *Corros. Sci.* **44,** 1809–1824.

139. Kern, P. & Landlot, D. Adsorption of Organic Corrosion Inhibitors on Iron in the Active and Passive State. A Replacement Reaction between Inhibitor and Water Studied with the Rotating Quartz Crystal Microbalance. *Electrochem. Acta* **47,** 589–598 (2001).

140. Akrout, B., Bousselmi, L. & Triki, E. Adsorption Mechanism of Non-Toxic Organic Inhibitors on Steel in Solutions at pH 8 Determined by Electrochemical Quartz Crystal Microbalance Measurments. *Mater. Corros.* **56,** 185–191.

141. Ochoa, N., Moran, F., Pebere, N. & Tribollet, B. Influence of low on the Corrosion Inhibition of Carbon Steel by Fatty Amines in Association with Phophonocarboxylic Acid Salt. *Corros. Sci.* **47,** 593–604 (2005).

142. Musa, A. *et al.* Stability of Layer Forming for Corrosion Inhibitor on Mild Steel Surface under Hydrodynamic Conditions. *Int J Electrochem.* **4,** 707–716 (2009).

143. Fagundes Netto, J. ., Fabre, J. & Peresson, L. Shape of Long Bubbles in Horizontal Slug Flow. *Int. J. Multiph. Flow* **25,** 1129–1160 (1999).

144. Fan, Z. & Jepson, W. A Model for Stationary Slugs. *Int J Multiph. Flow* **18,** 477–494 (1992).

145. Wang, X., Wang, T. & He, L. Measurement of Gas Entrainment from Stationary Liquid Slug in Horizontal Tube with Double-Sensor Conductivity Probe. *Flow Meas. Instrum.* **27,** 81–91 (2012).

146. Laws, J. Localized, Flow Dependent, Sweet Corrosion at Regions of Drastic Changes in Elevations: Hilly Terrain and River Crossing. (Ohio University, 2000).

147. Gregg, M., R. & Lerbscher, J. Non Foaming Corrosion Inhibitor Developments Providing Mitigating Benefits Against CO2 Corrosion for Application in High

Volume Gas Wells. in *CORROSION/04* paper No 04371 (NACE International, 2004).

148. Joosten, M., Kolts, J., Humble, P. G., Gough, M. A. & Hannah, I. Partitioning of Corrosion Inhibitor in Relationship to Oil Field Appications and Laboratory Testing. in *CORROSION/00* paper No 00018 (NACE International, 2000).

149. Thitakamol, B. & Veawab, A. Foaming Behavior in CO2 Absorption Process using Aqueous Solutions of Single and Blended Alkanolamines. *Ind Eng Chem Res* **47,** 216–225 (2008).

150. Horsup, D., Clark, J., Binks, B., Fletcher, D. & Hicks, J. The Fate of Oilfield Corrosion Inhibitors in Multiphase Systems. *Corrosion* **66,** (2010).

151. Blumer, D. & Babcock, M. Adsorption of Corrosion Inhibitor on Formation Sand and Proppant. in (NACE Canadian/Western Region, 1996).

152. Ramachandran, S., Ahn, Y., Bartrip, K., Jovancicevic, V. & Bassett, W. Further Advances in the Development of Erosion Corrosion Inhibitors. in *CORROSION/05* paper No 05292 (NACE international, 2005).

153. Smart, J. Flow Velocity Requiered for Solid Particle Movement in Oil and Gas Pipeline. in *CORROSION/09* paper No 09469 (NACE International, 2009).

154. Smart, J. The Role of Corrosion Inhibitors in Preventing Erosion Corrosion in High Rate Oil and Gas Production System. in *CORROSION/91* paper No 0469 (NACE International, 1991).

155. Ramachandran, S., Ward, M., Batrip, K. & Jovancicevic, V. Inhibition of the Effects of Particle Impingement. in *CORROSION/02* paper No 02498 (NACE International, 2002).

156. Addis, J. Erosion-Corrosion in Disturbed Liquid/Particle Flow. (Ohio University, 2008).

157. Atkin, R., Craig, V. & Biggs, S. Adsorption Kinetics and Structural Arrangements of Cationic Surfactants on Silica Surfaces. *Langmuir* **16,** 9374–9381 (2000).

158. Atkin, R., Craig, V. & Biggs, S. Adsorption Kinetics and Structural Arrangements of Cetylpyridinium Bromide at the Silica-Aqueous Interface. *Langmuir* **17,** 6155–6163 (2001).

159. Bera, A., Kumar, T., Ojha, K. & Mandal, A. Adsorption of Surfactants on Sand Surface in Enhanced Oil Recovery: Isotherms, Kinetics and Thermodynamic Studies. *Appl. Surf. Sci.* **284,** 87–99 (2013).

160. Damaskin, B., Petrii, O. & Batrakov, V. *Adsorption of Organic Compounds on Electrodes*. (Plenum Press, 1971).

Thesis and Dissertation Services